

**Modeling and Simulation of
Multiphase/Multicomponent Flows**

by

Randy S. Lagumbay

B.S., MSU-IIT, Philippines, 1997

M.S., The University of New South Wales, Australia, 2001

A thesis submitted to the

Faculty of the Graduate School of the
University of Colorado in partial fulfillment

of the requirements for the degree of

Doctor of Philosophy

Department of Mechanical Engineering

2006

This thesis entitled:
Modeling and Simulation of Multiphase/Multicomponent Flows
written by Randy S. Lagumbay
has been approved for the Department of Mechanical Engineering

Prof. Oleg V. Vasilyev

Prof. David Kassoy

Prof. John Daily

Prof. Sedat Biringen

Dr. Jin Wang

Date _____

The final copy of this thesis has been examined by the signatories, and we find that both the content and the form meet acceptable presentation standards of scholarly work in the above mentioned discipline.

Randy S. Lagumbay, (Ph.D., Mechanical Engineering)

Modeling and Simulation of Multiphase/Multicomponent Flows

Thesis directed by Prof. Oleg V. Vasilyev

Most of the existing approaches in dealing with multiphase/multicomponent flows are limited to either single-phase multicomponent or multiphase single-component mixtures. To remove this limitation, a new model for multiphase/multicomponent flows with an arbitrary number of components in each phase is developed. The proposed model is based on a homogenized fluid mixture approach. The model is hyperbolic and gives an accurate value for the mixture speed of sound when compared to experimental data. A numerical method based on the homogenized mixture formulation and extension of Roe and HLLC scheme is developed. The new approach for modeling and numerical simulation of multiphase/multicomponent flows is applicable to a variety of flow configurations including shock waves, cavitation, single and multiphase turbulent flow, free surface flow, high-pressure and high-speed flows. In order to validate the proposed approach for a variety of flow regimes, a novel “idealized” fluid-mixture model is proposed and an exact solution for the multiphase/multicomponent Riemann problem in one dimension is derived. A number of existing benchmark problems for single-phase multicomponent flows becomes a subset of this new model problem. To verify the accuracy of the proposed numerical method and to demonstrate the physical capability of the proposed model, three classical benchmark problems (single-phase two-component shock tube, shock wave propagation in a single-phase two-component fluid, and single-phase shock-bubble interaction) and two novel benchmark problems for an “idealized” fluid-mixture model (two-phase shock-tube and two-phase rarefaction problems) are presented. Furthermore, the flexibility of the new approach is demonstrated by extending the methodology to cavitating and turbulent flows. Representative cavitation and multiphase/multicomponent subgrid scale models

in the context of direct numerical simulations and large eddy simulations are considered and numerical simulations demonstrating these capabilities are performed.

Dedication

To my father, mother, brother and sister.

Acknowledgements

This thesis would not have been possible without the support of many people. I would like to express many thanks with deepest sincerity to my advisor, Professor Oleg V. Vasilyev, for his tremendous support and guidance, expertise and excellent advice, patience and understanding throughout this work. I would like to acknowledge the support and help of Professor Andreas Haselbacher for providing the Rocflu code and giving valuable comments and suggestions. Thanks to my committee members, Professor David Kassoy, Professor John Daily, Professor Sedat Biringen and Dr. Jin Wang who offered guidance and support. I would like to acknowledge the support of Argonne National Laboratory for sponsoring this work under grants number 2-RP50-P-00005-00, 3B-00061, 4B-00821, 5F-00462. Also, the support from MSU-IIT are gratefully acknowledge. I would like to extend my appreciation to my friends and colleagues in MU-Columbia and CU-Boulder, Dr. Dan Goldstein, Tanarit Sakulyanontvittaya, Dr. Alexei Vesolainen, Jonathan Regele, Qianlong Liu, Dr. Chetan Malhotra, Dr. Hrishikish Panchawagh and Myongjai Lee for their encouragements and discussions. I am very grateful and thankful to my father, mother, brother, sister, relatives and numerous friends who endured this long process with me, always offering support and love. Above all, I offer this success to the Almighty God for giving me knowledge, strength, courage and determination.

Contents

Chapter

1	Introduction	1
1.1	Motivation	1
1.2	Experimental Study	3
1.3	Numerical Study	6
1.4	Objectives of the Research	10
1.5	Research Methodology	10
1.6	Organization of the Thesis	12
2	Mathematical Formulation	15
2.1	Homogenized-Mixture Model	16
2.2	Governing Equations	16
2.2.1	Transport Variables Model	19
2.3	Mixture Equation of State	20
2.3.1	Mixture Pressure using Dalton's Law	21
2.3.2	Mixture Pressure using Amagat-Leduc Law	22
2.4	Mixture Speed of Sound	23
3	Idealized Fluid-Mixture Model	30
3.1	Density and Equation of State for Idealized Fluid-Mixture	30
3.2	Entropy for Idealized Fluid-Mixture	32

3.3	Speed of Sound for Idealized Fluid-Mixture	34
3.4	Riemann Invariants for Idealized Fluid-Mixture	34
3.5	Riemann Problem for Idealized Fluid-Mixture	35
3.5.1	Left Shock Wave Analysis	37
3.5.2	Right Shock Wave Analysis	38
3.5.3	Left Rarefaction Wave Analysis	39
3.5.4	Right Rarefaction Wave Analysis	40
3.5.5	Complete Solution	40
4	Numerical Method for Simulation of Multiphase/Multicomponent Flows	42
4.1	Extended Roe's Approximate Riemann Solver	42
4.2	Extended HLLC Approximate Riemann Solver	49
5	Code Verification and Model Validation	54
5.1	Single-Phase Two-Component Shock-Tube Problem	55
5.2	Shock-Wave Propagation in a Single-Phase Two-Component Fluid	55
5.3	Two-Phase Shock-Tube Problem for Idealized Fluid Mixture	58
5.4	Two-Phase Rarefaction Problem for Idealized Fluid Mixture	60
5.5	Single-Phase Two-Component Shock-Bubble Interaction	61
6	Multiphase and Multicomponent Free Surface Nozzle Jet Flow	67
6.1	Shock Tube Analysis in an Expanded Duct	68
6.2	Multiphase/Multicomponent Free Surface Jet Flow	70
6.2.1	Jet Formation and Jet Radial Profile	74
6.3	Multiphase/Multicomponent Cavitating Nozzle Jet Flow	77
6.3.1	Cavitation Overview	77
6.3.2	Cavitation Modeling and Simulation	80
6.3.3	Cavitation in Nozzle Injector	84

6.4	The Effect of Fluctuating Inflow Condition to the External Jet Formation	90
7	Multiphase and Multicomponent Turbulent Flows	92
7.1	Turbulent Modeling	93
7.2	Multiphase/Multicomponent Large Eddy Simulation	94
7.2.1	Governing Equations	95
7.2.2	Subgrid Scale (SGS) Model	97
7.3	Large Eddy Simulation of a Plane Jet	100
7.3.1	Single Phase LES of a Plane Jet	102
7.3.2	Multiphase/Multicomponent LES of a Plane Jet	109
8	Conclusions and Future Research	119
8.1	Concluding Remarks	119
8.2	Future Research	123
Bibliography		125

Tables**Table**

5.1	Properties of air and helium used in the simulations of shock-bubble interaction.	61
5.2	Comparison of computed velocities with those measured by Haas and Sturtevant [53] and computed by Quirk and Karni [105].	65

Figures

Figure

1.1 Complex physics of the jet inside and near the nozzle region.	3
1.2 Cavitation in the vena contracta region. Reference: [114]	5
1.3 Shock wave generation in a gaseous medium due to a high pressure and supersonic jet flow. The image of shock wave is captured using synchrotron x-radiography. Reference: [89]	7
2.1 Speed of sound of a water-air mixture at $P = 1 \cdot 10^5$ Pa and $T = 298.15K$ as a function of the volume fraction of air. Speed of sound predicted by Eq. (2.50).	26
2.2 Speed of sound of a water-air mixture at $P = 1 \cdot 10^5$ Pa and $T = 298.15K$ as a function of the volume fraction of air. Comparison of predicted speed of sound with experimental data of Karplus [72] for frequencies of 1 kHz (diamonds), 0.5 kHz (squares) and extrapolated to zero frequency (circles).	26
2.3 Speed of sound of a water-air mixture at $P = 1 \cdot 10^5$ Pa and $T = 298.15K$ as a function of the mass fraction of air. Speed of sound predicted by Eq. (2.50) and using Eq. (2.4).	27
2.4 Speed of sound of a water-air mixture at $P = 1 \cdot 10^5$ Pa and $T = 298.15K$ as a function of the mass fraction of air. Comparison of predicted speed of sound with experimental data of Karplus [72] for frequencies of 1 kHz (diamonds), 0.5 kHz (squares) and extrapolated to zero frequency (circles).	27

2.5	Speed of sound of a liquid-gas mixture predicted by Eq. (2.50) at $P = 1 \cdot 10^5$ Pa and $T = 298.15K$, for a liquid-gas density ratio, $\rho_{\text{liquid}}/\rho_{\text{gas}} \approx 100$	28
2.6	Speed of sound of a liquid-gas mixture predicted by Eq. (2.50) at $P = 1 \cdot 10^5$ Pa and $T = 298.15K$, for a liquid-gas density ratio, $\rho_{\text{liquid}}/\rho_{\text{gas}} \approx 1000$	28
2.7	Speed of sound of a liquid-gas-vapor mixture predicted by Eq. (2.50) at $P = 1 \cdot 10^5$ Pa and $T = 298.15K$	29
3.1	Structure of the solution of the Riemann problem for the idealized-mixture formulation.	36
3.2	Four possible wave patterns of the solution of the Riemann problem [141]: (a) left rarefaction, contact, and right shock; (b) left shock, contact, and right rarefaction; (c) left rarefaction, contact, and right rarefaction; (d) left shock, contact, and right shock.	37
4.1	The Riemann wave diagram used in the Roe scheme.	45
4.2	The simplified Riemann wave diagram with two intermediate states used in the HLLC scheme.	50
5.1	Comparison of numerical (o) and exact (solid line) solutions for single-phase two-component shock-tube problem at $t \approx 517 \mu\text{s}$	56
5.2	Comparison of numerical (o) and exact (solid line) solution for shock-wave propagation in a single-phase two-component fluid at $t \approx 864 \mu\text{s}$	57
5.3	Comparison of numerical (o) and exact (solid line) solution for two-phase shock-tube problem for an idealized fluid mixture at $240 \mu\text{s}$	59
5.4	Comparison of numerical (o) and exact (solid line) solution for two-phase rarefaction problem for an idealized fluid mixture at $540 \mu\text{s}$	60
5.5	Schematic diagram of the computational domain for the shock-bubble interaction problem.	62

5.6	Numerically generated Schlieren images of the shock-bubble interaction computations on the fine grid at various times.	63
5.7	Numerically generated Schlieren images of the shock-bubble interaction computations at approximately $674 \mu\text{s}$ for different grid spacings.	64
5.8	Definition of locations at which velocities are measured. V_S - incident shock, V_T - transmitted shock, V_{ui} - upstream edge of bubble, and V_{di} - downstream edge of bubble.	65
6.1	Plot of (a) mass fraction of liquid, (b) x-velocity component, (c) mixture pressure, and (d) mixture temperature, after 5.7689×10^{-07} seconds through an expanded duct, showing the normal traveling shock.	69
6.2	Plot of: (top left) mixture density showing an oblique shock wave in a gaseous medium, (top right) contact discontinuities of the mixture density across the interface in the centerline of the jet axis, (bottom left) mass fraction of the liquid, and (bottom right) contact discontinuities of the mass fraction of the liquid across the interface in the centerline of the jet axis.	72
6.3	Plot of: (top left) mixture pressure showing an oblique shock wave in a gaseous medium, (top right) mixture pressure along the centerline of the jet axis, (bottom left) mixture temperature showing an oblique shock wave in a gaseous medium, and (bottom right) mixture temperature along the centerline of the jet axis.	73
6.4	Plot of: (top left) contact discontinuities of the x-velocity component of the mixture across the interface in the centerline of the jet axis, (top right) velocity profile of the jet at 1.8 mm from the exit of the nozzle, and (bottom) mixture x-velocity component showing an oblique shock wave in a gaseous medium.	74

6.5 Plot of the mass fraction of the liquid. The leading edge of the jet is about 3.0 mm from the nozzle exit.	75
6.6 Jet radial profile across the body of the jet at a distant of about 3.0 mm from the nozzle exit.	75
6.7 Comparison of the results between numerical simulation (bottom) and experimental observation of MacPhee <i>et al.</i> [89](top).	76
6.8 Plot of the mass fraction of the vapor after 2.000e-04 sec. Inflow condition: $P = 1,161,000 \text{ Pa}$; $u = 10 \frac{\text{m}}{\text{s}^2}$; domain length = 6 mm; orifice over nozzle entrance ratio: $\frac{a_t}{a_i} = 0.3$	82
6.9 Plot of the mass fraction of the vapor after 2.202e-04 sec. Inflow condition: $P = 1,161,000 \text{ Pa}$; $u = 10 \frac{\text{m}}{\text{s}^2}$; domain length = 6 mm; orifice over nozzle entrance ratio: $\frac{a_t}{a_i} = 0.3$	82
6.10 Plot of the mass fraction of vapor after 2.502e-04 sec. Inflow condition: $P = 1,161,000 \text{ Pa}$; $u = 10 \frac{\text{m}}{\text{s}^2}$; domain length = 6 mm; orifice over nozzle entrance ratio: $\frac{a_t}{a_i} = 0.3$	83
6.11 Plot of the mass fraction of vapor after 3.000e-04 sec. Inflow condition: $P = 1,161,000 \text{ Pa}$; $u = 10 \frac{\text{m}}{\text{s}^2}$; domain length = 6 mm; orifice over nozzle entrance ratio: $\frac{a_t}{a_i} = 0.3$	83
6.12 Plot of the pressure after 3.000e-04 sec. Inflow condition: $p = 1,161,000 \text{ Pa}$; $u = 10 \frac{\text{m}}{\text{s}^2}$; domain length = 6 mm; orifice over nozzle entrance ratio: $\frac{a_t}{a_i} = 0.3$	84
6.13 Plot of the initial condition of the system. The nozzle region is filled with liquid and the chamber downstream from the exit of the nozzle is filled with gas.	85
6.14 Plot of the computational mesh and boundary conditions of the two-dimensional plane model nozzle injector.	85

6.15 Cavitation inside the nozzle injector. Experimental results taken from Roosen <i>et al.</i> [114]. Injection pressure, $P_{inlet} = 80$ bar; exit pressure, $P_{exit} = 11$ bar.	86
6.16 Cavitation inside the nozzle injector. Numerical simulation by Yuan <i>et al.</i> [155]. Injection pressure, $P_{inlet} = 80$ bar; exit pressure, $P_{exit} = 11$ bar.	87
6.17 Results of the numerical simulation for a cavitating nozzle injector using the multiphase mixture formulation with a cavitation model. Injection pressure, $P_{inlet} = 80$ bar; exit pressure, $P_{exit} = 11$ bar.	87
6.18 Contour plot of the vapor (left) and gas (right) volume fraction inside and close to the exit of the nozzle injector. Constant steady injection pressure, $P_{inlet} = 80$ bar; exit pressure, $P_{exit} = 11$ bar.	88
6.19 Contour plot of the liquid volume fraction (left) and velocity profile (right) inside and close to the exit of the nozzle injector. Constant steady injection pressure, $P_{inlet} = 80$ bar; exit pressure, $P_{exit} = 11$ bar.	89
6.20 Plot of the unsteady external jet formation (left) and distribution of vapor volume fraction (right) inside and close to the exit of the nozzle injector. Periodic unsteady injection pressure, $P_{inlet} = 80 \pm 10$ bar; frequency, $f = 3.725$ mhz; exit pressure, $P_{exit} = 11$ bar.	91
 7.1 Computational grid on a $x - y$ section.	101
7.2 Zoom view near the inlet region.	101
7.3 Inflow boundary condition.	102
7.4 Profiles of the longitudinal velocity at different streamwise locations. . .	104
7.5 Profiles of the streamwise turbulence intensity at different locations. . .	104
7.6 Contours of the magnitude of vorticity on an xy -plane at different time. (a) $t=5.0E-05$ sec., (b) $1.04E-04$ sec., (c) $1.4E-04$ sec., (d) $1.88E-04$ sec. . .	105

7.7	Snapshots of contours of the (a)magnitude of vorticity on an xy-plane, (b) velocity, (c) density and (d) pressure at time, t=2.05E-04sec.	106
7.8	Snapshots of contours of the (a)magnitude of vorticity on an xy-plane, (b) velocity, (c) density and (d) pressure at time, t=2.60E-04sec.	107
7.9	Snapshots of contours of the (a)magnitude of vorticity on an xy-plane, (b) velocity, (c) density and (d) pressure at time, t=2.80E-04sec.	108
7.10	Comparison of a snapshot of turbulent jet. (a) extended LES approach for multiphase/multicomponent flows, (b) LES approach from [6].	109
7.11	Snapshots of multiphase jet at time, t=5.0E-04 sec.(a) mass fraction of liquid, (b) mass fraction of gas, (c) mass fraction of vapor.	111
7.12	Snapshots of multiphase jet at time, t=5.0E-04 sec.(a) mass fraction of liquid, (b) vorticity, (c) density, (d) energy, (e), pressure and (f) velocity vectors.	112
7.13	Snapshots of multiphase jet at time, t=7.7E-04 sec.(a) mass fraction of liquid, (b) vorticity, (c) density, (d) energy, (e), pressure and (f) velocity vectors.	113
7.14	Snapshots of multiphase jet at time, t=1.0E-03 sec.(a) mass fraction of liquid, (b) vorticity, (c) density, (d) energy, (e), pressure and (f) velocity vectors.	115
7.15	Snapshots of multiphase jet at time, t=1.2E-03 sec.(a) mass fraction of liquid, (b) vorticity, (c) density, (d) energy, (e), pressure and (f) velocity vectors.	116
7.16	Snapshots of multiphase jet at time, t=1.4E-03 sec.(a) mass fraction of liquid, (b) vorticity, (c) density, (d) energy, (e), pressure and (f) velocity vectors.	117

Chapter 1

Introduction

This thesis focuses on the development of analytical and computational approach for modeling and numerical simulation of multiphase (liquid or gas) and multicomponent (several species of the same phase) flows, which is applicable to a variety of flow configurations including shock waves, cavitation, single and multiphase turbulent flows, free surface flow, high-pressure and high-speed flows. The approach is demonstrated by solving many problems with different flow configurations.

1.1 Motivation

Multiphase and multicomponent flows are common in many engineering applications. Relevant examples are fuel sprays in combustion process, liquid-jet machining of materials, and steam generation and condensation in nuclear reactors. The physical mechanisms underlying multiphase and multicomponent flows as well as the interplay of these mechanisms is very complex. In multiphase and multicomponent flows the phases and/or components can assume a large number of complicated configurations; small-scale interactions between the phases can have a profound impact on macroscopic flow properties [54]. The modeling and numerical simulation of multiphase and multicomponent flows poses far greater challenges than that of single-phase and single-component flows. These challenges are due to interfaces between phases and large or discontinuous property variations across interfaces between phases and/or components.

High-pressure and supersonic multiphase and multicomponent jet flow is one of the most challenging problems in multiphase flow due to the complexity of the dynamics of the jet. For example, the presence of cavitation and gas entrapment inside the nozzle orifice can greatly affect the development and formation of the external jet. Experimental evidence demonstrates that cavitation within the nozzle influences the characteristics of the nozzle exit spray [60, 128]. The jet exits the nozzle orifice as a bubbly fluid, which carries some of the trapped gas and cavitation bubbles. The jet properties behave as a multiphase mixture of liquid, gas and vapor. Due to a high injection pressure and a small nozzle orifice, the multiphase and multicomponent jet flow often exits the nozzle orifice at supersonic condition with respect to the surrounding gas; hence, generates an oblique shock wave in the gaseous medium [89]. Figure 1.1 shows a sketch of the complex physics of a supersonic multiphase and multicomponent jet flow inside and near the nozzle region.

Most of the current research on high-pressure supersonic multiphase and multicomponent jet flows through a gaseous medium is experimental, and the evolution of the jet hydrodynamics is not completely and clearly revealed. The understanding of the flow pattern of the jet is still rather limited. The characteristic properties of the jet depend on many factors such as whether flow is laminar or turbulent, subsonic or supersonic, and single phase or multiphase/multicomponent. The jet could be a single phase or multiphase/multicomponent fluid. A typical multiphase/multicomponent jet consists of bubbles that are carried in the flow stream. These bubbles could be the vapor generated in the nozzle orifice due to cavitation and/or could be the gas entrapped inside the nozzle. In addition, jet velocity could be larger than the speed of sound in the gaseous medium resulting in generation of shock waves to the surrounding gas environment, and producing compression waves inside the jet in an opposite direction of the jet velocity. Another phenomenon is the jet entrained near the surrounding media towards the direction of the flow, which creates a secondary flow of the surrounding

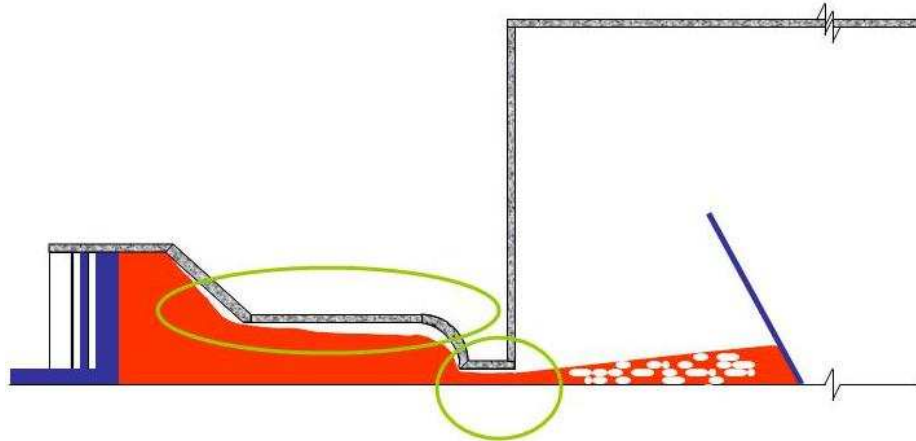


Figure 1.1: Complex physics of the jet inside and near the nozzle region.

medium. Further downstream, the surrounding medium near the main jet flow diffuses due to the viscous diffusion of the momentum.

1.2 Experimental Study

Experimental investigation in this area has been rare and detailed quantitative data is very limited due to the difficulties involved resulting from the small size of the injector nozzle that ranges from $100 \mu\text{m}$ - 1 mm , high injection pressure that may reach upwards to 2000 bar in a very short time period, the high speed flow, which may reach supersonic velocity [155], and the cost and difficulty of manufacturing experimental devices. The aforementioned time frame, on the order of $1 - 10 \mu\text{s}$ [155], presents the greatest challenge to modeling the internal flow of a nozzle and to capturing the process of cavitation formation for investigation.

Most experimental studies have been performed on large scale transparent models in order to visualize the cavitation structure. The first cavitation water tunnel was built by Sir Charles Parsons in 1895 after identifying the reason why the ship propellers failed to produce the design thrust. However, Parsons experienced with unsuccessful results of the trials as reported by Burrill [21]. In 1910, Parsons constructed a large water tunnel,

which could test 12 in. diameter propellers under cavitating conditions. During the period of World War II, a few other tunnels for propeller research with the refinements and improvements over Parson's tunnel were built in Europe and the USA. By the same period, the general interest in cavitation phenomena was extended (1) to tests in venturi meters and other conduits with restrictions, (2) to circuits for tests of single-hydrofoil sections and (3) to variable-pressure circuits for hydraulic pump and turbine investigations. Knapps *et al.* [75] have presented and discussed some special equipment developed to produce cavitation under controlled conditions in a specified locations, where observations can be made.

After the end of World War II, the interest in cavitation phenomena increased and many of the research has focused on the effect of cavitation development in injection nozzles to the jet formation and spray atomization. In 1959, Bergwerk [16] performed an experimental study of the flow pattern in diesel nozzle spray holes. It was observed during the experiment that at high injection rates, the fluid pressure in the vena contracta region inside the nozzle decreased below the saturation vapor pressure of the fluid, which causes a vapor formation in that region [114]. Similar observations have been reported in the experiments described in Refs. [7, 84, 99, 114]. Figure 1.2 shows cavitation in the vena contracta region. Although this cavitation can improve jet break-up [7, 109] and can enhance jet atomization [134], it increases the hydraulic resistance of the nozzle and produces noise and vibrations that can cause damage to the working surfaces [75]. The experimental research in nozzle cavitation continues to progress. Hiroyasu *et al.* [63] have studied the internal flow in a nozzle injector and the effect of cavitation in the break up length of a liquid spray. Arcoumanis *et al.* [9] have investigated the development of cavitation in a vertical multi-hole diesel injector. Soteriou *et al.* [128] have studied the effect of cavitation and hydraulic flip on atomization in direct injection diesel sprays, while He *et al.* [60] and Ruiz *et al.* [115] have looked into the effect of cavitation and turbulence on high-speed atomization. The spectral

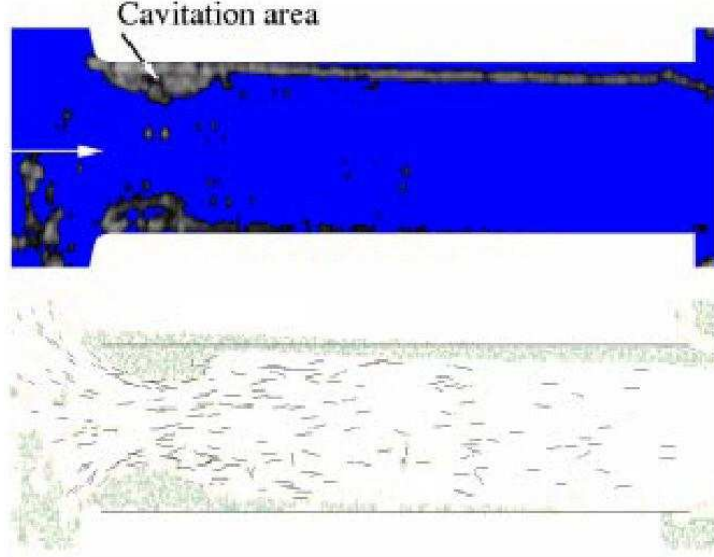


Figure 1.2: Cavitation in the vena contracta region. Reference: [114]

characteristics of turbulent flow in a diesel fuel nozzle injector were studied by Knox *et al.* [77]. The application of refractive index matching to study the internal flow in a diesel nozzle injector were conducted by Arcoumanis *et al.* [10]. The use of laser light illumination to visualize the development of cavitation in the orifice of a diesel injector were performed by Soteriou *et al.* [129]. Ganippa *et al.* [48] have used a transparent scaled-up single-hole diesel nozzle to study the cavitation phenomenon.

Further experimental studies of cavitation have shown that the characteristics of the flow from a large scale transparent models differs from an actual scale [8]. The difference is caused by the flow scaling effects associated with imperfections in micro- and macro- geometry of the flow and the nature of the flow. Because of this flow scaling effects, many researchers [8, 12, 23, 25, 69, 83, 117, 134] have used an actual scale in conducting an experiments in order to determine the correct characteristics of the flow. Recent experimental studies have focused on the spray cone angles for a cavitating nozzle flow [25, 152], cavitation oscillation frequencies [23], and the length of the cavity [117]. Payri *et al.* [100] examined the influence of cavitation on the internal flow and the

macroscopic behavior of spray in diesel injection nozzles, and concluded that cavitation leads to incremental changes of the spray cone angle and increases the outlet velocity.

So far, most of the experimental research mentioned in the previous paragraph has focused on the development of cavitation inside the nozzle injector and the effect of cavitation to the jet formation and spray atomization. However, none of them have paid attention close to the exit of the nozzle region. Over the past few years, despite of the substantial advances in laser diagnostics [26, 62, 156], the region close to the nozzle still has not yielded desired quantitative information. A high-pressure fuel spray has never been recognized as supersonic under typical fuel injection conditions [97, 124]. Recently, MacPhee *et al.* [89] have used a synchrotron x-radiography and a fast x-ray detector to record the time evolution of the transient fuel sprays from a high-pressure injector. In their experiment, the propagation of the spray-induced shock waves in a gaseous medium were captured and the complex nature of the spray hydrodynamics were revealed. They have found out that under injection conditions similar to those in operating engines, the fuel jets can exceed supersonic speeds and result an oblique shock wave in the gaseous medium, see Figure 1.3. However, the effect of this shock wave to the atomization of the fuel and the combustion processes is currently not known.

1.3 Numerical Study

In the experimental studies, the understanding of the complex nature of the high-pressure supersonic multiphase jet flow is limited. However, numerical and theoretical investigations complement each other and provide detailed quantitative explanations of the complex structure of the jet from single phase flow to a more complex multiphase flows. Numerical modeling and simulation has become the best of the alternative tools to supplement experimental study, and provide very promising results in improving the understanding of the complex nature of the jet flow. With the advancement of computer technology and improvement of numerical technique, the majority of current research

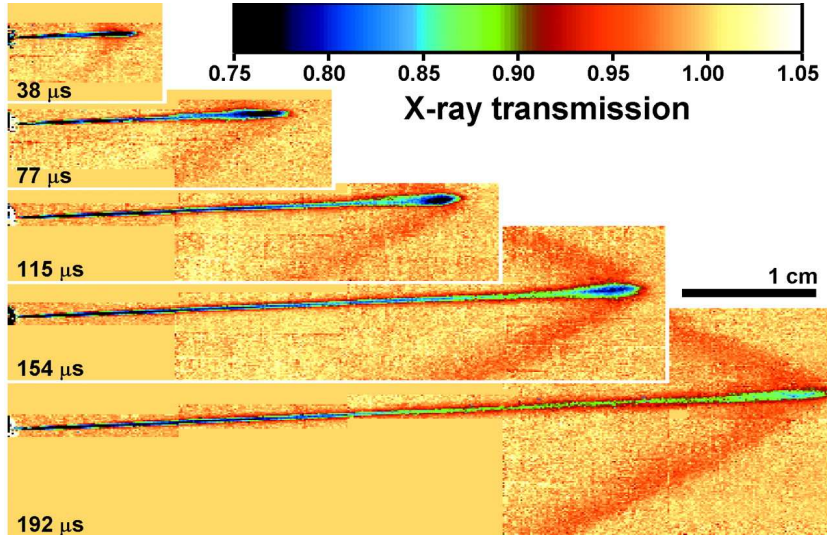


Figure 1.3: Shock wave generation in a gaseous medium due to a high pressure and supersonic jet flow. The image of shock wave is captured using synchrotron x-radiography. Reference: [89]

have focused on numerical modeling and simulation.

Bunnell *et al.* [20] have performed a three-dimensional simulation of unstable cavitating flows in injector passages and have demonstrated the effect of cavitation on both the mean and unsteady components of the orifice discharge coefficient. Similarly, Dirke *et al.* [33] have carried out three-dimensional simulations of cavitating flows in diesel injectors and have shown the distribution of cavitation zones. Yuan *et al.* have demonstrated the strong interaction of a cavitating nozzle flow with the external jet formation [155] and the effect of injection pressure fluctuations on the cavitation processes in injection nozzles [154]. A numerical study of cavitating flow through various nozzle geometries was performed by Schmidt *et al.* [122] and the results show that the upstream geometry has a small influence on the nozzle flow. A numerical simulation of three-phase (air, fuel liquid, and fuel vapor) flow in a high pressure swirl injectors was presented by Alajbegovic *et al.* [5]. A formation of a thin conical fuel sheet with an air core and cavitation in the pressure depression initiated in the air core was predicted in

the simulation.

The flow inside the nozzle is composed of a mixture of liquid, vapor, and gas, and exits the nozzle through a gaseous medium. The numerical modeling and simulation of a multiphase and multicomponent flow is a very daunting task as compared to a single phase flow. In a multiphase and multicomponent flow the phases and/or components will assume a large number of complicated configurations, in which small-scale interactions between the phases and/or components can have profound effects on the macroscopic properties of the flow [54]. The most common problem encountered in multiphase and multicomponent flow modeling is the fluid interface, where a large density variation exists. This causes flow phenomena to become more complex because of additional non-linearity introduced by the indeterminacy of such surfaces. In addition, the fluid interface may be unstable, changing the flow configuration of the problem [103].

Several numerical simulations of multiphase and multicomponent flow have been conducted over the past few years with different modeling approach and numerical techniques. It has been shown that each model and numerical method has limits to their respective capabilities. To this date, there has been a great need of improving the technique of modeling multiphase and multicomponent flow and of a numerical method to perfectly capture the complex nature of the flow.

Dumont *et al.* [37] and Shin [125] have used the homogeneous equilibrium model to solve two-phase (liquid and vapor) cavitating flows. Their models differ on the equation of state of the mixture and the numerical scheme. Taking a different approach, Alajbegovic *et al.* [5] and Tatschl *et al.* [136] have used the two-fluid formulation for multiphase flows [35] to simulate three phase cavitating flows. The conservative form of the Favre-averaged Navier-Stokes equations have been utilized by Senocak *et al.* [123] to study cavitating flows through convergent-divergent nozzles. A direct calculation of cavitating flows by the Space-Time Conservation Element and Solution Element (CE/SE) method is reported by Qin *et al.* [104]. The CE/SE method is applicable

for flows at wide range of Mach numbers and suitable for time accurate simulations. Vortman *et al.* [149] have proposed a new approach based on postulating Gibbs free energy for the phase mixture. The two-phase flow is treated numerically by combining the rate equation with a volume of fluid approach.

Singhal *et al.* [126] have developed a full cavitation model that accounts for the formation and transport of vapor bubble, turbulent fluctuations of pressure and velocity, and the magnitude of non-condensable gases that are dissolved in the operating liquid. A reduced form of Rayleigh-Plesset equation for bubble dynamics has been used to derive the phase change rate equations. The model has assumed an isothermal flow process, and decoupling the cavitation module from heat transfer and radiation modules. The model has been implemented in an advanced, commercial, general-purpose CFD code called CFD-ACE+ by CFD Research Corporation (CFDRC). Taking a similar approach, Delale *et al.* [32] have used a continuum bubbly liquid flow model with bubble nucleation, and nonlinear bubble dynamics described by the classical Rayleigh-Plesset equation in quasi one dimensional steady state cavitating nozzle flows. Another approach using multi-dimensional modeling of multiphase flow to examine the multi-physics of high-speed nozzle and jet flows were presented by Murphy *et al.* [96].

In addition, Ahuja *et al.* [4] have formulated a multiphase model for low speed gas/liquid mixtures by reducing the compressible system of equations to an acoustically accurate form for multi-fluid mixtures. Also, Hosangadi *et al.* [65] have developed a generalized numerical framework for transient and multiphase problems that involve a combination of gas, bulk liquid, and a dense dispersed phase. The model has been improved by allowing flexibility of specifying variables for thermodynamic properties and specifying physical equations of state for mixture constituents [3].

1.4 Objectives of the Research

The main objective of this thesis is to develop a general approach for modeling and numerical simulation of multiphase and multicomponent, compressible and incompressible flows, which is applicable to a variety of flow configurations including shock waves, cavitation, single and multi-phase turbulent flows. The approach is flexible and can have an arbitrary number of components in each phase using either Euler or Navier-Stokes formulation. It must be emphasized that the modeling and computational approach developed in this thesis is flexible enough to incorporate a variety of different cavitation and/or turbulence models. To illustrate these capabilities numerical simulation using representative models are performed.

1.5 Research Methodology

Two approaches are commonly used for the simulation of multiphase and multicomponent flows. In the first approach, each phase and/or component is considered to occupy a distinct volume and the interfaces between the phases and/or components are tracked explicitly, see, e.g., [17, 36, 42, 50, 87, 118, 135]. In the second approach, the phases and/or components are spatially averaged to lead to a homogeneous mixture and are considered to occupy the same volume. The phases and/or components need not be in equilibrium, i.e. their mechanical and thermodynamical properties may differ. The advantage of the homogenized-mixture approach compared to the interface-tracking approach is that it solves only one set of equations for the mass, momentum, and energy of the mixture, supplemented by equations for the mass or volume fraction of the mixture constituents [94]. In this research, the homogenized-mixture approach is used and mechanical and thermodynamical equilibrium is assumed, i.e. pressure, temperature, and velocity are identical for all the phases and components.

Multiple approaches of dealing with multiphase or multicomponent mixtures ex-

ist. However, most of them are limited to either single phase multicomponent fluids [1, 70, 79, 80] or multiphase single component mixtures [13, 22, 133]. To remove this limitation, a new model for multiphase and multicomponent flows with an arbitrary number of components in each phase is developed. The model is hyperbolic, allowing the construction of upwind methods for the computation of convective fluxes. Furthermore, the model is acoustically and thermodynamically consistent, which means that the model gives an accurate value for the mixture speed of sound.

To perform simulations which demonstrate the capabilities of the new multiphase and multicomponent model, a numerical method is developed, based on a finite-volume framework [57, 58, 59]. The Roe's approximate Riemann solver [112] and the modified Harten, Lax and van Leer scheme (HLLC) [15] are extended to multiphase and multicomponent flows and used to capture shock waves and contact discontinuities. The numerical method is verified by applying it to a number of test problems. The problems were chosen to highlight the flexibility and robustness of the new approach and cover the following flow regimes:

1. single-phase single-component fluid;
2. single-phase multicomponent fluid;
3. multiphase single component fluid;
4. multiphase multicomponent fluid.

It should be noted that a number of benchmark problems for cases 1-3 are available [1, 2, 13, 22, 71, 120, 150]. However, no test problem for case 4 that has an exact closed-form solution for arbitrary initial conditions and arbitrary numbers of phases and components has been reported until now. To address this deficiency, a novel “idealized” fluid mixture model is developed, which allows the derivation of an exact solution for the multiphase and multicomponent Riemann problem in one dimension. A number of

existing benchmark problems for single-phase multicomponent flows become a subset of this new problem.

1.6 Organization of the Thesis

In the thesis body, additional short reviews of the research areas related to the particular applications are given in an appropriate places. The rest of this thesis is organized as follows. Chapter 2 introduces the mathematical formulation for multiphase and multicomponent flow. The governing multiphase and multicomponent equations in conservative form and the mathematical model for the mixture variables are presented. The mathematical model for multiphase and multicomponent flow is based on the homogenized-mixture approach. The governing equations of the homogenized-mixture model for the simulation of multiphase and multicomponent flows are described. The determination of the speed of sound of the mixture as well as the validation of the mixture speed of sound is presented. Also, the calculation of the mixture equation of state using two different approaches such as Dalton’s Law and Amagat’s Law is presented.

The governing equations for the multiphase and multicomponent flows cannot be solved exactly for arbitrary mixtures. In Chapter 3, a novel idealized fluid-mixture model is developed. This new model allows derivation of exact solution for one dimensional multiphase/multicomponent Riemann problem. A number of existing benchmark problems for single-phase multicomponent flows becomes a subset of this new model problem. In addition, the expressions of the equation of state and entropy for an idealized fluid-mixture are derived. Also, the Riemann invariants and eigenvectors of the idealized fluid mixture are presented for one-dimensional flows.

The development of the numerical method is presented in Chapter 4. Two advanced numerical schemes based on Roe’s approximate Riemann solver [112] and the modified Harten, Lax and van Leer scheme (HLLC) [15] are extended to multiphase

and multicomponent flows and used to capture shock waves and contact discontinuities. The spatial and temporal discretization as described in [57, 58, 59] is adopted, except that the equations being solved represent the mixture of liquid, gas, and vapor with two additional conservation equations for the mass fractions of the gas and vapor. The spatial discretization is based on the unstructured finite-volume framework and the classical four-stage Runge-Kutta method in low-storage formulation is used for the temporal discretization.

In Chapter 5, the new developed solver for simulation of multiphase and multicomponent flows is verified and validated by solving some benchmark problems including the novel benchmark problems for the idealized fluid-mixture model. The problems considered are:

1. Single-phase two-component shock-tube problem;
2. Shock-wave propagation in a single-phase two-component fluid;
3. Two-phase single-component shock-tube problem for idealized-fluid mixture;
4. Two-phase single-component rarefaction problem for idealized fluid mixture;
5. Single-phase two-component shock-bubble interaction.

Chapter 6 demonstrates the flexibility of the new developed general approach to incorporate a variety of cavitation model for modeling and numerical simulation of multiphase and multicomponent flows. A representative cavitation model proposed by Hosangadi *et al.* [64] is integrated into the framework. The approach with the incorporated cavitation model is tested to perform simulation of multiphase and multicomponent cavitating nozzle jet flow through a gaseous medium. The results of the numerical simulation, which captures the cavitation process in the nozzle orifice are presented.

Chapter 7 extends the new developed general approach to modeling and simulation of turbulent multiphase and multicomponent flows. The extended large eddy simulation (LES) methodology for multiphase and multicomponent flows is incorporated into the general framework. The capability of the extended LES for multiphase and multicomponent flows is examined by conducting a numerical simulation of turbulent plane jet in both single phase and multiphase/multicomponent flow regime.

Finally, conclusions and possible future extensions of the work are outlined in Chapter 8.

Chapter 2

Mathematical Formulation

The mathematical model for multiphase and multicomponent flow is based on the homogenized-mixture approach. The phases and/or components are spatially averaged and are considered to occupy the same volume. The advantage of the homogenized-mixture approach compared to the other approach, i.e. interface-tracking approach, is that it solves only one set of equations for mass, momentum and energy of the mixture, supplemented by equations for the mass or volume fraction of the mixture constituents [94]. However, there are challenges associated with the use of this approach like the mathematical closure of the system that is acoustically and thermodynamically consistent.

The governing equations of the homogenized-mixture model for the simulation of multiphase and multicomponent flows are described in the following. The mixture is assumed to be in thermodynamic and mechanical equilibrium so that the temperature T , pressure P , and velocity components u , v and w of the phases and components are identical. In the description to follow, the mixture is assumed to consist of two phases, namely liquid and gas, and the gas phase is assumed to consist of two components, namely a generic gas and a vapor. These are denoted by the subscripts l , g , and v for liquid, gas, and vapor, respectively. It should be noted, however, that the homogenized-mixture model can be extended in a straightforward fashion to an arbitrary number of phases and components. Variables without subscripts are applicable to the mixture

only. The subscript i is used to denote a specific component.

2.1 Homogenized-Mixture Model

The homogenized-mixture model is based on the notion that quantities associated with a given phase and/or component are averaged to give the corresponding mixture quantity. Accordingly, quantities per unit volume are averaged by their respective volume fraction ϕ_i . For example, the mixture density is given by

$$\rho_m = \sum_{i=l,g,v} \rho_i \phi_i, \quad (2.1)$$

where the volume fractions satisfy the constraint

$$\sum_{i=l,g,v} \phi_i = 1. \quad (2.2)$$

Conversely, quantities per unit mass are averaged by their respective mass fractions Y_i .

For example, the specific heat at constant volume of the mixture is given by

$$c_{vm} = \sum_{i=l,g,v} c_{vi} Y_i. \quad (2.3)$$

The volume and mass fractions are related through

$$\rho_i \phi_i = \rho_m Y_i. \quad (2.4)$$

2.2 Governing Equations

The Navier-Stokes equations governing the evolution of mass, momentum, energy, and composition of the mixture can be written in vector form as

$$\frac{\partial \mathbf{Q}}{\partial t} + \frac{\partial \mathbf{E}}{\partial x} + \frac{\partial \mathbf{F}}{\partial y} + \frac{\partial \mathbf{G}}{\partial z} = \frac{\partial \mathbf{E}_v}{\partial x} + \frac{\partial \mathbf{F}_v}{\partial y} + \frac{\partial \mathbf{G}_v}{\partial z} + \mathbf{S}, \quad (2.5)$$

where \mathbf{Q} is the vector of the conserved variables and \mathbf{E} , \mathbf{F} and \mathbf{G} are the convective flux vectors given by

$$\mathbf{Q} = \begin{bmatrix} \rho_m \\ \rho_m u \\ \rho_m v \\ \rho_m w \\ \rho_m e_{mT} \\ \rho_g \phi_g \\ \rho_v \phi_v \end{bmatrix}, \quad \mathbf{E} = \begin{bmatrix} \rho_m u \\ \rho_m u^2 + P \\ \rho_m uv \\ \rho_m uw \\ (\rho_m e_{mT} + P)u \\ \rho_g \phi_g u \\ \rho_v \phi_v u \end{bmatrix}, \quad \mathbf{F} = \begin{bmatrix} \rho_m v \\ \rho_m vu \\ \rho_m v^2 + P \\ \rho_m vw \\ (\rho_m e_{mT} + P)v \\ \rho_g \phi_g v \\ \rho_v \phi_v v \end{bmatrix}, \quad \mathbf{G} = \begin{bmatrix} \rho_m w \\ \rho_m wu \\ \rho_m wv \\ \rho_m w^2 + P \\ (\rho_m e_{mT} + P)w \\ \rho_g \phi_g w \\ \rho_v \phi_v w \end{bmatrix}. \quad (2.6)$$

where u , v and w are the x -, y - and z -components of the velocity vector of the mixture, respectively, and the total energy, e_{mT} , is defined as

$$e_{mT} = c_{vm} T + \frac{1}{2} (u^2 + v^2 + w^2). \quad (2.7)$$

The constitutive equations of the liquid, gas, and vapor are assumed to take the form

$$\rho_i = \rho_i(P, T). \quad (2.8)$$

The mathematical model derived in this thesis is general and can be used for arbitrary forms of the equation of state for each phase. However, in the present study the gas and vapor are assumed to obey the ideal-gas laws

$$\rho_g = \frac{P}{R_g T}, \quad (2.9)$$

$$\rho_v = \frac{P}{R_v T}, \quad (2.10)$$

while the liquid is assumed to be a linear dependent of pressure and temperature

$$\rho_l = \rho_o + \frac{1}{C_l^2} (P - P_o) - \left(\frac{\beta_l}{C_l} \right)^2 (T - T_o), \quad (2.11)$$

where ρ_o , P_o and T_o are the reference density, pressure and temperature of the liquid, respectively. C_l and β_l are the isothermal speed of sound and compressibility of the liquid, respectively.

The vectors \mathbf{E}_v , \mathbf{F}_v and \mathbf{G}_v on the right hand side of Eq. (2.5) are the viscous flux vectors written as

$$\mathbf{E}_v = [0, \tau_{xx}, \tau_{yx}, \tau_{zx}, \Theta_x, \Psi_{gx}, \Psi_{vx}]^T, \quad (2.12)$$

$$\mathbf{F}_v = [0, \tau_{xy}, \tau_{yy}, \tau_{zy}, \Theta_y, \Psi_{gy}, \Psi_{vy}]^T, \quad (2.13)$$

$$\mathbf{G}_v = [0, \tau_{xz}, \tau_{yz}, \tau_{zz}, \Theta_z, \Psi_{gz}, \Psi_{vz}]^T. \quad (2.14)$$

The total stress, τ_{ij} , are defined as

$$\tau_{ij} = 2\mu_m S_{ij} - \frac{2}{3}\mu_m \frac{\partial v_k}{\partial x_k} \delta_{ij}, \quad (2.15)$$

where μ_m is the viscosity of the mixture and $S_{ij} = \frac{1}{2}(\partial \tilde{u}_i / \partial x_j + \partial \tilde{u}_j / \partial x_i)$ is the strain rate tensor. The work of the total stress and heat conduction in the fluid mixture are defined as

$$\Theta_x = \tilde{u}\tau_{xx} + \tilde{v}\tau_{xy} + \tilde{w}\tau_{xz} + \tilde{k}_m \frac{\partial \tilde{T}}{\partial x}, \quad (2.16)$$

$$\Theta_y = \tilde{u}\tau_{yx} + \tilde{v}\tau_{yy} + \tilde{w}\tau_{yz} + \tilde{k}_m \frac{\partial \tilde{T}}{\partial y}, \quad (2.17)$$

$$\Theta_z = \tilde{u}\tau_{zx} + \tilde{v}\tau_{zy} + \tilde{w}\tau_{zz} + \tilde{k}_m \frac{\partial \tilde{T}}{\partial z}, \quad (2.18)$$

where, k_m is the thermal conductivity of the mixture. Furthermore, the scalar fluxes of the gas and vapor are given by

$$\Psi_{gi} = \tilde{\varphi} \frac{\partial \bar{\rho}_m Y_g}{\partial x_i}, \quad (2.19)$$

$$\Psi_{vi} = \tilde{\varphi} \frac{\partial \bar{\rho}_m Y_v}{\partial x_i}, \quad (2.20)$$

where φ is the diffusion coefficient, which is considered to be zero, unless otherwise specified.

In addition, the vector \mathbf{S} on the the right hand side of Eq. (2.5) represents the source terms written as

$$\mathbf{S} = [0, 0, 0, 0, 0, 0, S_v]^T, \quad (2.21)$$

where S_v is the cavitation source term. S_v is zero until Section 6.3.2, where cavitation model is introduced. In general, source terms are non-zero in the case when there is phase transformation, chemical reactions, and/or body force. In this thesis, the source terms are limited only to mass transfer between liquid and vapor phases, which is a characteristic of cavitation process.

On the other hand, Eq. (2.5) can be simplified into Euler equations in the case of inviscid flow, with the assumptions of no viscosity effect, no heat transfer, and no body force. Thus, Eq. (2.5) can be reduced to

$$\frac{\partial \mathbf{Q}}{\partial t} + \frac{\partial \mathbf{E}}{\partial x} + \frac{\partial \mathbf{F}}{\partial y} + \frac{\partial \mathbf{G}}{\partial z} = \mathbf{S}. \quad (2.22)$$

The governing Euler equations for the mixture given in Eq. (2.22) are used in Chapters 5 and 6 for the numerical simulation of multiphase and multicomponent flows, while the governing Navier-Stokes equations given in Eq. (2.5) are considered in Chapter 7 for the numerical simulation of turbulent multiphase and multicomponent flows.

2.2.1 Transport Variables Model

The viscosity μ_m and thermal conductivity k_m of the mixtures are modeled by averaging the viscosity and thermal conductivity of the mixture constituents. These are given by

$$\mu_m = \sum_{i=l,g,v} \mu_i Y_i, \quad (2.23)$$

$$k_m = \sum_{i=l,g,v} k_i Y_i. \quad (2.24)$$

The viscosity for each constituents are modeled in the following. For the gas and vapor, the viscosity can be approximated using the Power law and Sutherland law [151], respectively given by

$$\mu_{i=g,v} \approx \mu_o \left(\frac{T}{T_o} \right)^n, \quad (2.25)$$

$$\mu_{i=g,v} \approx \mu_o \left(\frac{T}{T_o} \right)^{3/2} \left(\frac{T_o + S_{th}}{T + S_{th}} \right), \quad (2.26)$$

where μ_o is a reference viscosity at a reference absolute temperature T_o . The constants n and S_{th} are fit to the data. For example, for air, $n = 0.7$, $S_{th} \approx 110.4$ K, with $T_o = 273$ K and $\mu_o = 1.71 \times 10^{-5}$ kg/(m · s). For the liquid, the viscosity is approximated using the empirical function [151],

$$\ln \frac{\mu_l}{\mu_o} \approx a + b \left(\frac{T_o}{T} \right) + c \left(\frac{T_o}{T} \right)^2. \quad (2.27)$$

where, for water with $T_o = 273.16$ K, $\mu_o = 0.001792$ kg/(m · s), the suggested values for the constants are $a = -1.94$, $b = 4.80$, and $c = 6.74$.

The thermal conductivity for each constituents are calculated using the equation of Prandtl number,

$$k_{i=l,g,v} \approx \frac{c_{pi}\mu_i}{Pr}. \quad (2.28)$$

Some complex models of the properties of liquids and gases can be found in [108].

2.3 Mixture Equation of State

The equation of state of the mixture is very important in describing the physical and thermodynamical properties of the mixture of fluids. However, the evaluation of the properties of mixture is difficult, because any one property depends not only on two independent properties like pressure and temperature, but also on a specification of the composition of the mixture such as the mass or volume fraction of each component. On the other hand, the equation of state of the mixture provides a mathematical relationship between numerous state functions associated with matter, such as pressure, temperature, mass or volume fraction, speed of sound, specific heat, and many others.

The mathematical expressions of the equation of state for multiphase (liquid or gas) and multicomponent (several instances of the same phase) mixture can be obtained using the principle of either Dalton's Law or Amagat-Leduc Law. In the evaluation, each phase and/or component behaves as a compressible fluid. The derivation of the

equation of state is difficult and depends on the constitutive equation for each phase and/or component.

2.3.1 Mixture Pressure using Dalton's Law

In Dalton's law, the total pressure exerted by a mixture of gases is the sum of the component pressures P_i , each measured exclusively at the temperature T and volume V of the mixture. Hence, Dalton's law when applied to multicomponent mixture of gas and vapor can be written in the form

$$P_{gv} = \sum_{i=g,v} P_i = P_g + P_v, \quad (2.29)$$

$$V_{gv} = V_g = V_v, \quad (2.30)$$

where P_{gv} is the total pressure and V_{gv} is the volume of the multicomponent mixture of gas and vapor. Applying Eqs. (2.9) and (2.10) to Eqs. (2.29) and (2.30), supplemented with the mass balance of the gas and vapor mixture, yields

$$P_{gv} = \rho_{gv} R_{gv} T, \quad (2.31)$$

where

$$\begin{aligned} \rho_{gv} &= \frac{\rho_g \phi_g + \rho_v \phi_v}{\phi_{gv}}, \\ \phi_{gv} &= \phi_g = \phi_v, \\ R_{gv} &= \frac{\rho_g \phi_g R_g + \rho_v \phi_v R_v}{\rho_g \phi_g + \rho_v \phi_v}. \end{aligned}$$

Now, let us consider the case for a mixture of liquid, gas and vapor. The pressure exerted by the multicomponent mixture of gas and vapor, P_{gv} , and the pressure exerted by the liquid, P_l , in the overall mixture are assumed in equilibrium. Thus,

$$P = P_l = P_{gv}. \quad (2.32)$$

From Eq. (2.31), the following is obtained

$$\frac{P}{R_{gv} T} \phi_{gv} = \rho_g \phi_g + \rho_v \phi_v, \quad (2.33)$$

using the relation, $\phi_l + \phi_{gv} = 1$, yields

$$\frac{P}{R_{gv}T} (1 - \phi_l) = \rho_g \phi_g + \rho_v \phi_v. \quad (2.34)$$

Simplification gives

$$P (\rho_l - \rho_l \phi_l) = (\rho_g \phi_g + \rho_v \phi_v) \rho_l R_{gv} T. \quad (2.35)$$

To obtain a close form solution of Eq. (2.35), the constitutive equation of state of the liquid must be defined. Introducing Eq. (2.11) to Eq. (2.35), yields the exact solution of the mixture equation of state

$$P = \frac{\psi_1 - \psi_2 + \sqrt{(\psi_2 - \psi_1)^2 + 4\psi_2\psi_3}}{2}, \quad (2.36)$$

where

$$\begin{aligned} \psi_1 &= C_l^2 \left(\rho_o - \left(\frac{\beta_l}{C_l} \right)^2 (T - T_o) - \frac{P_o}{C_l^2} - \rho_l \phi_l \right), \\ \psi_2 &= (\rho_v \phi_v R_v + \rho_g \phi_g R_g) T, \\ \psi_3 &= C_l^2 \left(\rho_o - \left(\frac{\beta_l}{C_l} \right)^2 (T - T_o) - \frac{P_o}{C_l^2} \right). \end{aligned}$$

2.3.2 Mixture Pressure using Amagat-Leduc Law

In Amagat-Leduc law, the volume of a gas mixture is equal to the sum of the volumes of all constituents at the same temperature and pressure as the mixture. Hence, Amagat-Leduc law when applied to multicomponent mixture of gas and vapor can be written in the form

$$P_{gv} = P_g = P_v, \quad (2.37)$$

$$V_{gv} = \sum_{i=g,v} V_i = V_g + V_v, \quad (2.38)$$

where P_{gv} is the total pressure and V_{gv} is the volume of the multicomponent mixture of gas and vapor. Applying Eqs. (2.9) and (2.10) to Eqs. (2.37) and (2.38), supplemented with the mass balance of the gas and vapor mixture, yields

$$P_{gv} = \rho_{gv} R_{gv} T, \quad (2.39)$$

where

$$\begin{aligned}\rho_{gv} &= \frac{\rho_g\phi_g + \rho_v\phi_v}{\phi_{gv}}, \\ \phi_{gv} &= \phi_g + \phi_v, \\ R_{gv} &= \frac{\rho_g\phi_g R_g + \rho_v\phi_v R_v}{\rho_g\phi_g + \rho_v\phi_v}.\end{aligned}$$

Again, let us consider the case for a mixture of liquid, gas and vapor. The pressure exerted by the multicomponent mixture of gas and vapor, P_{gv} , and the pressure exerted by the liquid, P_l , in the overall mixture are assumed in equilibrium. Thus,

$$P = P_l = P_{gv}. \quad (2.40)$$

From Eq. (2.39), the following is obtained

$$\frac{P}{R_{gv}T}\phi_{gv} = \rho_g\phi_g + \rho_v\phi_v, \quad (2.41)$$

using the relation, $\phi_l + \phi_{gv} = 1$, yields

$$\frac{P}{R_{gv}T}(1 - \phi_l) = \rho_g\phi_g + \rho_v\phi_v. \quad (2.42)$$

Simplification gives

$$P(\rho_l - \rho_l\phi_l) = (\rho_g\phi_g + \rho_v\phi_v)\rho_l R_{gv}T, \quad (2.43)$$

which is the same with Eq. (2.35). In order to obtain a close form solution of Eq. (2.43), the constitutive equation of state of the liquid must be defined. Introducing Eq. (2.11) to Eq. (2.43), yields the exact solution of the mixture equation of state, which is the same with Eq. (4.17).

2.4 Mixture Speed of Sound

The acoustic differential of Eq. (2.8) is given by

$$d\rho_i = \frac{1}{C_i^2}dP + \left(\frac{\beta_i}{C_i}\right)^2dT, \quad (2.44)$$

where $C_i = (\partial P / \partial \rho_i)^{1/2}$ and $\beta_i = (\partial P / \partial T)_i^{1/2}$ are the isothermal speed of sound and compressibility of the i th component, respectively. Using Eqs. (2.1) and (3.13), the mixture-density differential can be written as

$$d\rho_m = (\rho_v - \rho_l)d\phi_v + (\rho_g - \rho_l)d\phi_g + \left(\frac{1}{C_\phi^2} - \frac{1}{C_{\phi\beta}^2} \right) dP, \quad (2.45)$$

where $1/C_\phi^2 = \sum_i \phi_i / C_i^2$ and $1/C_{\phi\beta}^2 = \sum_i \phi_i \beta_i^2 / C_i^2$.

The mixture speed of sound can be obtained easily by transforming Eq. (2.5) from conservative variables to primitive variables form

$$\Gamma \frac{\partial \mathbf{Q}_v}{\partial t} + \frac{\partial \mathbf{E}}{\partial x} + \frac{\partial \mathbf{F}}{\partial y} + \frac{\partial \mathbf{G}}{\partial z} = \frac{\partial \mathbf{E}_v}{\partial x} + \frac{\partial \mathbf{F}_v}{\partial y} + \frac{\partial \mathbf{G}_v}{\partial z} + \mathbf{S}, \quad (2.46)$$

where \mathbf{Q}_v is the vector of the primitive variables

$$\mathbf{Q}_v = [P, u, v, w, T, \phi_g, \phi_v]^T \quad (2.47)$$

and Γ is the transformation matrix defined by

$$\Gamma = \left[\frac{dQ_i}{dv_j} \right]_{i,j=1,\dots,7} = \left[\frac{\partial Q_i}{\partial Q_{vj}} \right] \quad (2.48)$$

The elements of the matrix are computed, for example; $\partial Q_5 / \partial Q_{v1} = \partial(\rho_m e_{mT}) / \partial P = e_l \phi_l / C_l^2 + e_g \phi_g / C_g^2 + e_v \phi_v / C_v^2$. After careful evaluation of all the elements in the matrix, the following is obtained

$$\Gamma = \begin{bmatrix} \frac{1}{C_\phi^2} & 0 & 0 & 0 & -\frac{1}{C_{\phi\beta}^2} & \rho_g - \rho_l & \rho_v - \rho_l \\ \frac{u}{C_\phi^2} & \rho_m & 0 & 0 & -\frac{u}{C_{\phi\beta}^2} & (\rho_g - \rho_l)u & (\rho_v - \rho_l)u \\ \frac{v}{C_\phi^2} & 0 & \rho_m & 0 & -\frac{v}{C_{\phi\beta}^2} & (\rho_g - \rho_l)v & (\rho_v - \rho_l)v \\ \frac{w}{C_\phi^2} & 0 & 0 & \rho_m & -\frac{w}{C_{\phi\beta}^2} & (\rho_g - \rho_l)w & (\rho_v - \rho_l)w \\ \frac{e_l \phi_l}{C_l^2} + \frac{e_g \phi_g}{C_g^2} + \frac{e_v \phi_v}{C_v^2} & \rho_m u & \rho_m v & \rho_m w & \rho_l \phi_l c_{vl} + \beta_T c_{vl} \phi_l T - \frac{1}{2} \left(\frac{u^2 + v^2 + w^2}{C_{\phi\beta}^2} \right) & \rho_g e_g - \rho_l e_l & \rho_v e_v - \rho_l e_l \\ \frac{\phi_g}{C_g^2} & 0 & 0 & 0 & -\frac{\beta_g^2 \phi_g}{C_g^2} & \rho_g & 0 \\ \frac{\phi_v}{C_v^2} & 0 & 0 & 0 & -\frac{\beta_v^2 \phi_v}{C_v^2} & 0 & \rho_v \end{bmatrix}.$$

The eigenvalues of the transformation matrix give the speed of sound. The resulting eigenvalues, λ_i of the system are all real and have an exact analytical expressions. These are given by

$$\lambda_i = (\mathbf{V} \cdot \hat{\mathbf{n}} - C_m, \mathbf{V} \cdot \hat{\mathbf{n}}, \mathbf{V} \cdot \hat{\mathbf{n}}, \mathbf{V} \cdot \hat{\mathbf{n}}, \mathbf{V} \cdot \hat{\mathbf{n}}, \mathbf{V} \cdot \hat{\mathbf{n}} + C_m), \quad (2.49)$$

where $\mathbf{V} = (u, v, w)$ is the velocity vector, $\hat{\mathbf{n}} = (n_x, n_y, n_z)$ is the unit normal vector, and C_m is the speed of sound of the mixture given by

$$C_m^2 = \frac{\rho_m c_{vm} + P \sum_i \frac{\phi_i}{\rho_i} \left(\frac{\beta_i}{C_i} \right)^2}{\rho_m^2 c_{vm} \sum_i \frac{\phi_i}{\rho_i} \frac{1}{C_i^2}}. \quad (2.50)$$

Note that in the case of multicomponent gases, Eq. (2.50) becomes

$$C_m = (\gamma_m R_m T)^{1/2}, \quad (2.51)$$

where $\gamma_m = c_{pm}/c_{vm} = \sum_i Y_i c_{pi}/\sum_i Y_i c_{vi}$, $R_m = \sum_i Y_i R_i$, and R_i is the gas constant of the i th gas component. Furthermore, it should be noted that due to the assumption of thermodynamic and mechanical equilibrium, the speed of sound predicted by Eq. (2.50) is applicable only to disturbances whose frequency tends to zero.

The speed of sound of a mixture of water and air at sea-level conditions predicted by Eq. (2.50) is plotted in Figure 2.1 as a function of the volume fraction of air. Note that over a wide range of volume fractions, the speed of sound of the mixture is much lower than the speed of sound of either medium [98]. The presence of gas in a liquid dramatically reduces the speed of sound in the liquid [14, 72, 90, 93]. The speed of sound in water is about 1480 m/s and about 340 m/s in air, but in an air-water mixture lies to about 20 m/s. A 1% by volume of air in water drops the speed of sound of the liquid by 95% to 100 m/s. This dramatic phenomenon occurs due to the compressibility effect of the gas in the liquid.

Similarly, the speed of sound of a mixture of water and air at sea-level conditions predicted by Eq. (2.50) and using Eq. (2.4) is plotted in Figure 2.3 as a function of the mass fraction of air. The speed of sound is approximately 1350 m/s for mass fraction of air at 10^{-8} , and decreases to 25 m/s for mass fraction of air at 10^{-3} . As shown in Figure 2.4, there is a definite dependence of speed of sound on frequency, but in general the measured data by Karplus [72] confirm the theoretical prediction of a large decrease of the value of speed of sound with admixture of gas into liquid.

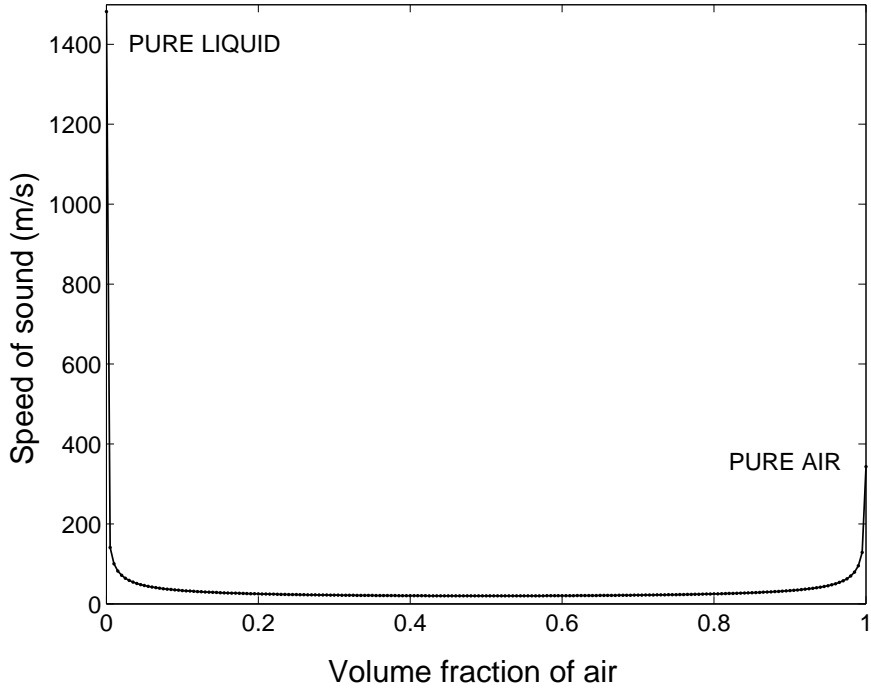


Figure 2.1: Speed of sound of a water-air mixture at $P = 1 \cdot 10^5$ Pa and $T = 298.15K$ as a function of the volume fraction of air. Speed of sound predicted by Eq. (2.50).

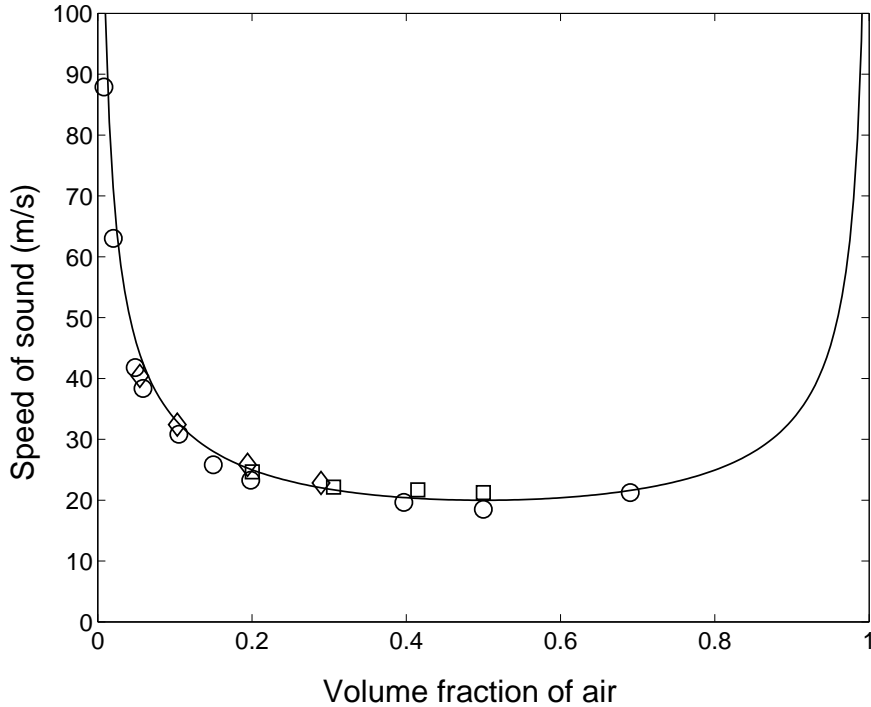


Figure 2.2: Speed of sound of a water-air mixture at $P = 1 \cdot 10^5$ Pa and $T = 298.15K$ as a function of the volume fraction of air. Comparison of predicted speed of sound with experimental data of Karplus [72] for frequencies of 1 kHz (diamonds), 0.5 kHz (squares) and extrapolated to zero frequency (circles).

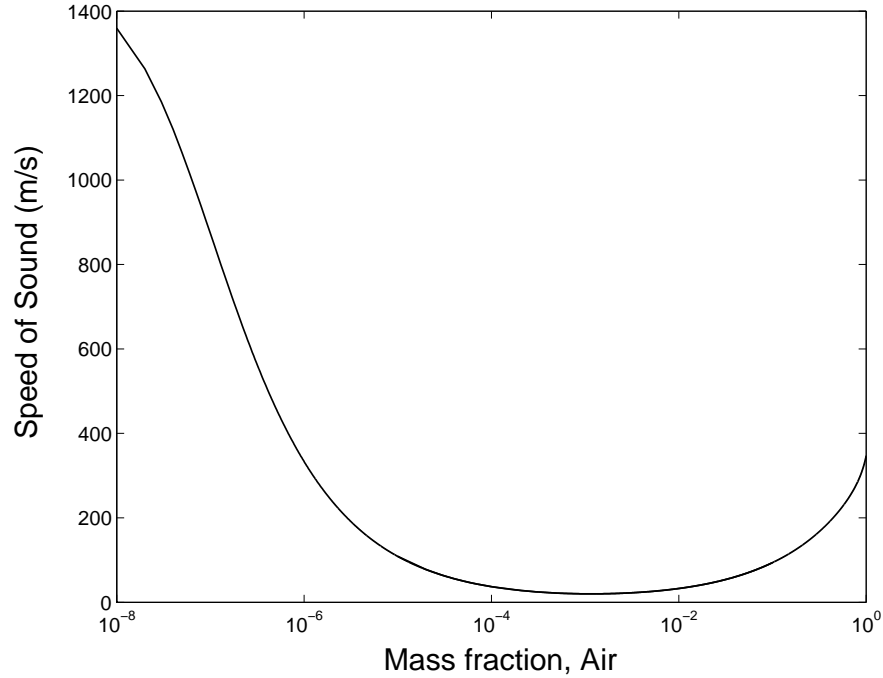


Figure 2.3: Speed of sound of a water-air mixture at $P = 1 \cdot 10^5$ Pa and $T = 298.15K$ as a function of the mass fraction of air. Speed of sound predicted by Eq. (2.50) and using Eq. (2.4).

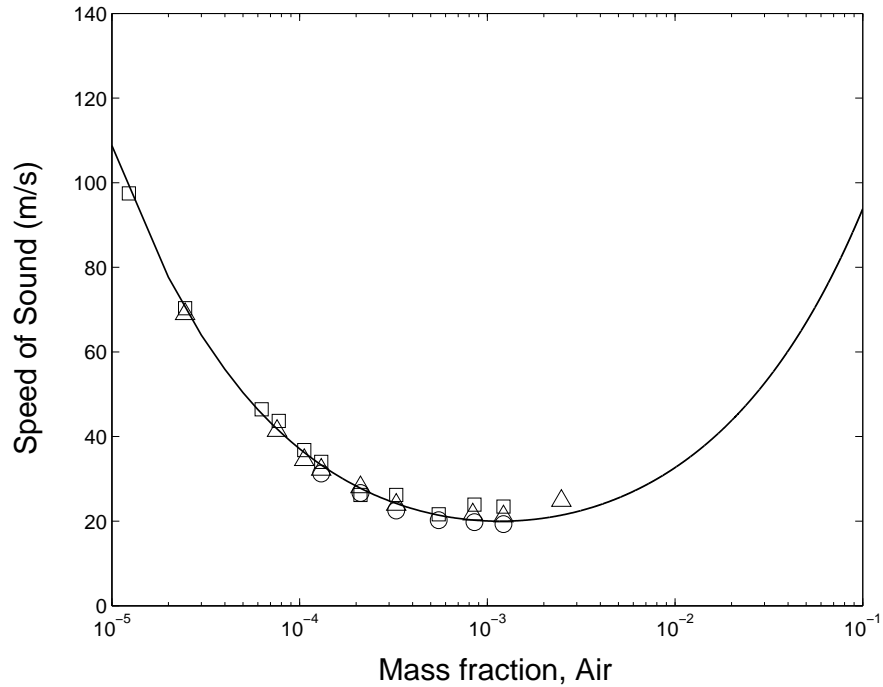


Figure 2.4: Speed of sound of a water-air mixture at $P = 1 \cdot 10^5$ Pa and $T = 298.15K$ as a function of the mass fraction of air. Comparison of predicted speed of sound with experimental data of Karplus [72] for frequencies of 1 kHz (diamonds), 0.5 kHz (squares) and extrapolated to zero frequency (circles).

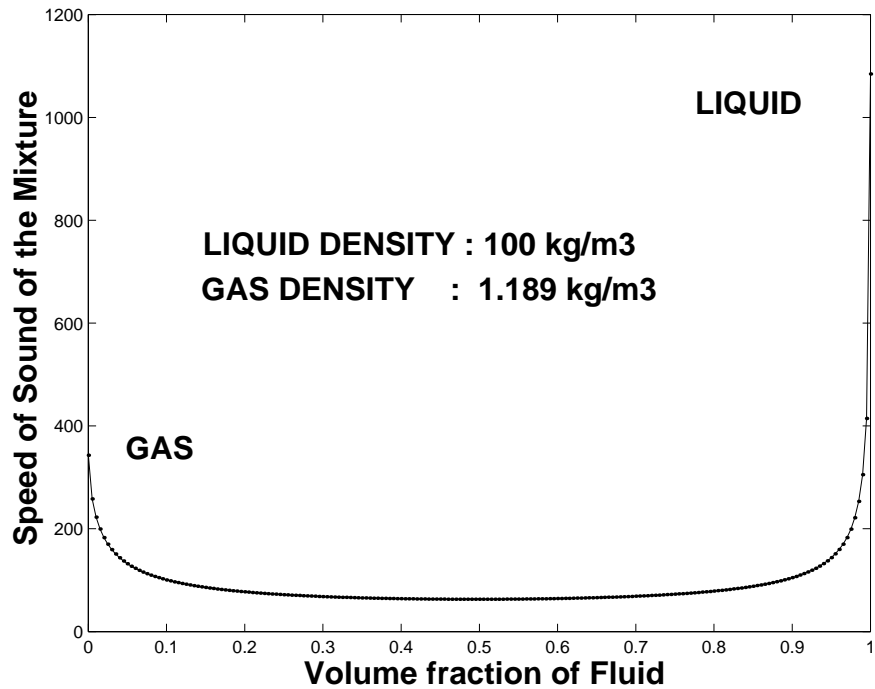


Figure 2.5: Speed of sound of a liquid-gas mixture predicted by Eq. (2.50) at $P = 1 \cdot 10^5$ Pa and $T = 298.15K$, for a liquid-gas density ratio, $\rho_{\text{liquid}}/\rho_{\text{gas}} \approx 100$.

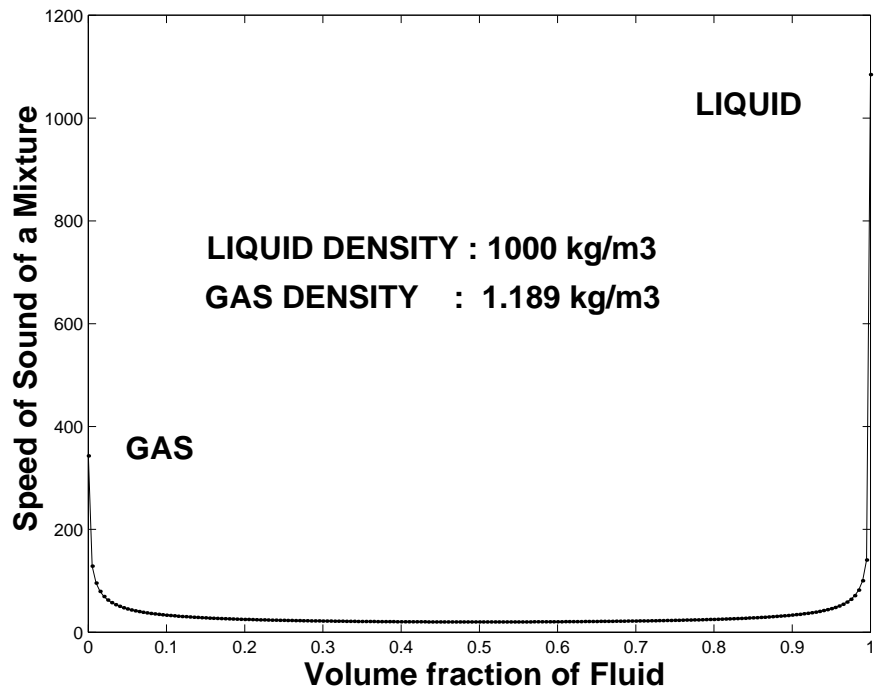


Figure 2.6: Speed of sound of a liquid-gas mixture predicted by Eq. (2.50) at $P = 1 \cdot 10^5$ Pa and $T = 298.15K$, for a liquid-gas density ratio, $\rho_{\text{liquid}}/\rho_{\text{gas}} \approx 1000$.

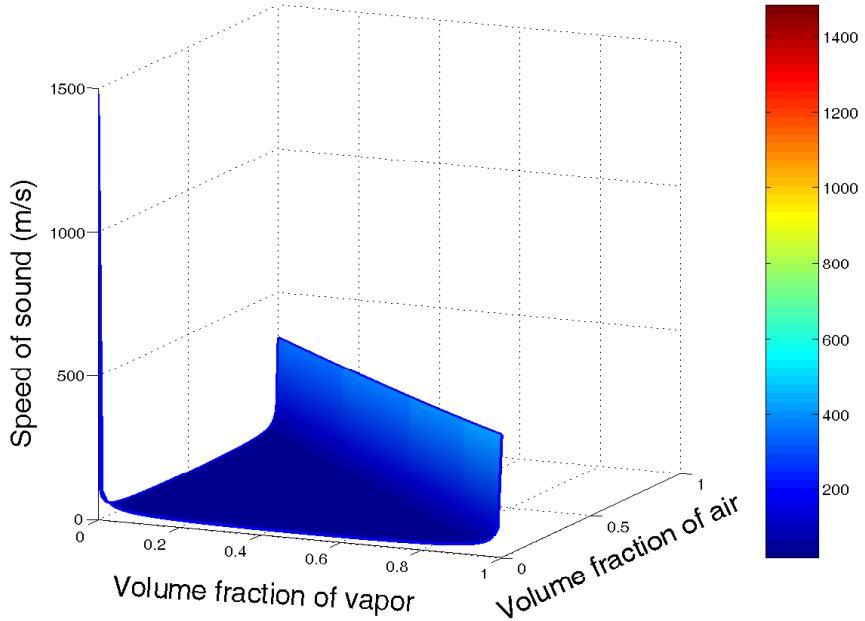


Figure 2.7: Speed of sound of a liquid-gas-vapor mixture predicted by Eq. (2.50) at $P = 1 \cdot 10^5$ Pa and $T = 298.15K$.

Figures 2.2 and 2.4 show a good agreement between the value predicted by Eq. (2.50) and the experimental data of Karplus [72]. The predicted speed of sound was also compared to Refs. [3, 4, 35, 74, 143] and, although not plotted, is in good agreement.

Moreover, the speed of sound of the mixture varies also with the variation of the density ratio of the liquid and gas. A high density ratio of liquid and gas will have a much lower speed of sound as compared to a low density ratio. For a density ratio of 100, the speed of sound of the mixture is about 100 m/s, see Figure 2.5, however, for a density ratio of 1000, the speed of sound of the mixture drops off rapidly to about 25 m/s, see Figure 2.6. In addition, for a mixture of liquid, gas, and vapor at sea-level conditions, the speed of sound is shown in Figure 2.7.

Chapter 3

Idealized Fluid-Mixture Model

The governing equations for the multiphase and multicomponent flows cannot be solved analytically for arbitrary mixtures. The equation of state for each component must be carefully chosen if an exact solution is to be found. In this section, a novel idealized fluid-mixture model is developed, and exact solutions for one dimensional multiphase and multicomponent Riemann problem are derived. In addition, the Riemann invariants and eigenvectors of the idealized fluid mixture are presented.

3.1 Density and Equation of State for Idealized Fluid-Mixture

To obtain a closed-form solution of the governing equations, the mixture entropy is assumed to be a function of pressure, temperature and mass fractions of the species, i.e. $s_m = s_m(P, T, Y_i)$. Differentiation gives

$$ds_m = \frac{\partial s_m}{\partial P} dP + \frac{\partial s_m}{\partial T} dT + \sum_{i=l,g,v} \frac{\partial s_m}{\partial Y_i} dY_i, \quad (3.1)$$

and because ds_m is assumed to be an exact differential, then it follows that

$$\frac{\partial^2 s_m}{\partial P \partial T} = \frac{\partial^2 s_m}{\partial T \partial P}, \quad (3.2)$$

$$\frac{\partial^2 s_m}{\partial Y_i \partial T} = \frac{\partial^2 s_m}{\partial T \partial Y_i}, \quad (3.3)$$

$$\frac{\partial^2 s_m}{\partial Y_i \partial P} = \frac{\partial^2 s_m}{\partial P \partial Y_i}. \quad (3.4)$$

Using the T - ds equation applied to the mixture gives

$$ds_m = c_{vm} \frac{dT}{T} + \frac{P}{T} d\left(\frac{1}{\rho_m}\right) + \frac{1}{T} \sum_{i=l,g,v} L_i dY_i, \quad (3.5)$$

where L_i is the latent heat of phase change and is assumed to be a function of pressure and temperature, i.e. $L_i = L_i(P, T)$.

From Eq. (2.4) the following relation is obtained

$$\frac{1}{\rho_m} = \sum_{i=l,g,v} \frac{Y_i}{\rho_i}, \quad (3.6)$$

and differentiation gives

$$d\left(\frac{1}{\rho_m}\right) = \sum_{i=l,g,v} \left(\frac{dY_i}{\rho_i} - Y_i \frac{d\rho_i}{\rho_i^2} \right). \quad (3.7)$$

Substituting the differential form of Eq. (2.8) into Eq. (3.7) results

$$d\left(\frac{1}{\rho_m}\right) = \sum_{i=l,g,v} \left(\frac{dY_i}{\rho_i} + Y_i \frac{\partial}{\partial P} \left(\frac{1}{\rho_i} \right) dP + Y_i \frac{\partial}{\partial T} \left(\frac{1}{\rho_i} \right) dT \right). \quad (3.8)$$

Subsequent substitution of Eqs. (2.3) and (3.8) into Eq. (3.5) yields

$$ds_m = \sum_{i=l,g,v} \left\{ \left[\frac{c_{vi} Y_i}{T} + \frac{P}{T} Y_i \frac{\partial}{\partial T} \left(\frac{1}{\rho_i} \right) \right] dT + \left[\frac{P}{T} Y_i \frac{\partial}{\partial P} \left(\frac{1}{\rho_i} \right) \right] dP + \left[\frac{P}{T \rho_i} + \frac{L_i}{T} \right] dY_i \right\}. \quad (3.9)$$

Applying exact differential properties (3.1)-(3.4) to Eq. (3.9) results in the following constraints

$$\sum_{i=l,g,v} \frac{Y_i}{\rho_i^2} \left(\frac{\partial \rho_i}{\partial T} + \frac{P}{T} \frac{\partial \rho_i}{\partial P} \right) = 0, \quad (3.10)$$

$$\frac{\partial}{\partial T} \left(\frac{L_i}{T} \right) = \frac{c_{vi}}{T} + \frac{P}{T^2 \rho_i}, \quad (3.11)$$

$$\frac{\partial}{\partial P} \left(\frac{L_i}{T} \right) = -\frac{1}{T \rho_i}. \quad (3.12)$$

In order for Eq. (3.10) to be satisfied for arbitrary mass fractions, the expression inside of the brackets must be equal to zero for each phase/component. Consequently, the constitutive equation for each phase/component must be a function of the ratio of pressure and temperature, i.e.

$$\rho_i = \rho_i \left(\frac{P}{T} \right). \quad (3.13)$$

Thus, to obtain an analytical solution for the mixture entropy, the density of each component must be a function of the ratio of pressure and temperature. Because the gas and vapor are assumed to follow the ideal-gas laws, see Eqs. (2.9) and (2.10), they automatically satisfy Eq. (3.13). For the liquid, the following relation is proposed

$$\rho_l = \rho_o + \alpha \frac{P}{T}, \quad (3.14)$$

where $\alpha = T_o/C_{l_o}^2$, T_o is the reference temperature, C_{l_o} is the reference speed of sound, and ρ_o is the reference density of the liquid. A liquid obeying Eq. (3.14) is called an **idealized liquid** in this thesis. Equation (3.14) can be regarded as a model for a liquid described by Eq. (2.8). To see this, note that the linearized model given in Eq. (2.11) can be approximated by Eq. (3.14), provided that the temperature variations are small.

Combining Eqs. (2.9), (2.10), (3.14) and (3.6), the mixture density can be written as

$$\rho_m = \frac{z}{zY_l/\rho_l + R_g Y_g + R_v Y_v} = \frac{z}{zY_l(\rho_o + \alpha z)^{-1} + R_g Y_g + R_v Y_v}, \quad (3.15)$$

where $z = P/T$. The mixture defined by Eq. (3.15) is called an idealized fluid mixture because it is derived from the idealized liquid defined above and an ideal gas and vapor.

Note that Eq. (3.15) can also be interpreted as the equation of state of the mixture.

3.2 Entropy for Idealized Fluid-Mixture

Integrating Eqs. (3.11) and (3.12) from some reference state (P^r, T^r) the following equation for the latent heat of phase change is obtained

$$\frac{L_i}{T} = c_{vi} \ln \frac{T}{T^r} + F_i(z) + \frac{L_i^r}{T^r}, \quad (3.16)$$

where

$$F_i(z) = - \int_{z^r}^z \frac{1}{\rho_i(\zeta)} d\zeta. \quad (3.17)$$

Integrating Eq. (3.9) results in the following expression for the entropy of the

mixture

$$s_m = \sum_{i=l,g,v} \left\{ c_{vi} Y_i \ln \frac{T}{T^r} + \frac{PY_i}{T\rho_i} + \left[F_i \left(\frac{P}{T} \right) + \frac{L_i^r}{T^r} \right] Y_i \right\}. \quad (3.18)$$

The expression (3.18) can be further simplified by using Eqs. (2.3) and (3.6)

$$s_m = c_{vm} \ln \frac{T}{T^r} + \frac{P}{\rho_m T} + \sum_{i=l,g,v} \left[F_i \left(\frac{P}{T} \right) + \frac{L_i^r}{T^r} \right] Y_i. \quad (3.19)$$

Substituting equations of state (2.9), (2.10), (3.14) for the gas-vapor-liquid mixture into Eq. (3.19) yields

$$s_m = c_{vm} \ln \frac{T}{T^r} + \left(a_1 + \frac{Y_l}{\alpha} \right) - \frac{Y_l}{\alpha} \ln \left(\frac{\rho_l}{\rho_l^r} \right) - a_1 \ln \left(\frac{z}{z^r} \right) - \frac{Y_l \rho_0}{\alpha \rho_l} + \sum_{i=l,g,v} \frac{L_i^r}{T^r} Y_i, \quad (3.20)$$

where $a_1 = R_g Y_g + R_v Y_v$.

Evaluating Eq. (3.20) at two different states and subtracting one from another, one obtains

$$\begin{aligned} [s_m]_1^2 &= \left[c_{vm} \ln \frac{T}{T^r} \right]_1^2 + \left[a_1 + \frac{Y_l}{\alpha} \right]_1^2 - \frac{1}{\alpha} \left[Y_l \ln \left(\frac{\rho_l}{\rho_l^r} \right) \right]_1^2 - \left[a_1 \ln \left(\frac{z}{z^r} \right) \right]_1^2 \\ &- \frac{\rho_0}{\alpha} \left[\frac{Y_l}{\rho_l} \right]_1^2 + \sum_{i=l,g,v} \frac{L_i^r}{T^r} [Y_i]_1^2, \end{aligned} \quad (3.21)$$

where square brackets denote the following operation $[(\cdot)]_1^2 = (\cdot)_2 - (\cdot)_1$.

If no mass transfer between the phases is present, i.e. the mass fractions are assumed constant, $Y_{i1} = Y_{i2} = Y_i$, Eq. (3.21) reduces to

$$s_{m2} - s_{m1} = c_{vm} \ln \frac{T_2}{T_1} - \frac{Y_l}{\alpha} \ln \frac{\rho_{l2}}{\rho_{l1}} - a_1 \ln \frac{z_2}{z_1} - \frac{\rho_o Y_l}{\alpha} \left(\frac{1}{\rho_{l2}} - \frac{1}{\rho_{l1}} \right), \quad (3.22)$$

For isentropic changes of state, Eq. (3.22) leads to

$$\frac{T_2}{T_1} = \left(\frac{z_2}{z_1} \right)^{\frac{a_1}{c_{vm}}} \left(\frac{\rho_{l2}}{\rho_{l1}} \right)^{\frac{Y_l}{\alpha c_{vm}}} \exp \left[\frac{\rho_o Y_l}{\alpha c_{vm}} \left(\frac{1}{\rho_{l2}} - \frac{1}{\rho_{l1}} \right) \right]. \quad (3.23)$$

For the case of a pure gas, Eq. (3.23) reduces to

$$\frac{T_2}{T_1} = \left(\frac{P_2}{P_1} \right)^{(\gamma_g - 1)/\gamma_g}, \quad (3.24)$$

where $\gamma_g = 1 + R_g/c_{vg}$. For the case of a pure liquid Eq. (3.23) reduces to

$$\frac{T_2}{T_1} = \left(\frac{\rho_{l2}}{\rho_{l1}} \right)^{\frac{1}{\alpha c_{vm}}} \exp \left[\frac{\rho_o}{\alpha c_{vm}} \left(\frac{1}{\rho_{l2}} - \frac{1}{\rho_{l1}} \right) \right]. \quad (3.25)$$

3.3 Speed of Sound for Idealized Fluid-Mixture

The speed of sound of the idealized fluid mixture can be obtained by applying Eqs. (2.9)-(3.14) to Eq. (2.50), giving

$$C_m^2 = \frac{\rho_m c_{vm} + P\beta^2 \left(\frac{\phi_l}{\rho_l C_l^2} + \frac{\phi_v}{\rho_v C_v^2} + \frac{\phi_g}{\rho_g C_g^2} \right)}{\rho_m^2 c_{vm} \left(\frac{\phi_l}{\rho_l C_l^2} + \frac{\phi_v}{\rho_v C_v^2} + \frac{\phi_g}{\rho_g C_g^2} \right)}, \quad (3.26)$$

where $C_l = (T/\alpha)^{1/2}$, $C_g = (R_g T)^{1/2}$, and $C_v = (R_v T)^{1/2}$ are the isothermal speeds of sound in the liquid, gas, and vapor, respectively, and $\beta = \beta_l = \beta_g = \beta_v = (P/T)^{1/2}$ is the compressibility. Note that the compressibilities are identical for the idealized mixture. Simplification yields

$$C_m^2 = \frac{\rho_m c_{vm} C_{\phi/\rho}^2 + P\beta^2}{\rho_m^2 c_{vm}}, \quad (3.27)$$

where

$$\frac{1}{C_{\phi/\rho}^2} = \frac{\phi_l}{\rho_l C_l^2} + \frac{\phi_v}{\rho_v C_v^2} + \frac{\phi_g}{\rho_g C_g^2}. \quad (3.28)$$

Equations (3.27) and (2.50) give practically identical results if the sound speeds of the idealized and non-idealized liquid are matched at the reference temperature T_o .

3.4 Riemann Invariants for Idealized Fluid-Mixture

For one-dimensional problems, the eigenvalues are given by

$$\boldsymbol{\lambda} = (u - C_m, u, u, u, u + C_m)^T, \quad (3.29)$$

and the corresponding set of eigenvectors are

$$\boldsymbol{\Pi} = \begin{bmatrix} \frac{1}{\rho_m C_m^2} & -\frac{1}{C_m} & 0 & 0 & 0 \\ \frac{P}{\rho_m^2 C_m^2 c_{vm} T} & 0 & \frac{1}{T} & 0 & 0 \\ -\frac{\phi_g}{\rho_g \rho_m C_g^2 C_m^2} \left(\rho_g C_g^2 - \rho_m C_m^2 + \frac{\beta_g^2 P}{\rho_m c_{vm}} \right) & 0 & 0 & 1 & 0 \\ -\frac{\phi_v}{\rho_v \rho_m C_v^2 C_m^2} \left(\rho_v C_v^2 - \rho_m C_m^2 + \frac{\beta_v^2 P}{\rho_m c_{vm}} \right) & 0 & 0 & 0 & 1 \\ \frac{1}{\rho_m C_m^2} & \frac{1}{C_m} & 0 & 0 & 0 \end{bmatrix}. \quad (3.30)$$

The Riemann invariants are computed from the relation $d\boldsymbol{\Upsilon} = \boldsymbol{\Pi} d\boldsymbol{K}$, where $\boldsymbol{K} = [P, u, T, \phi_g, \phi_v]^T$,

$$d\boldsymbol{\Upsilon} = \begin{bmatrix} \frac{dP}{\rho_m C_m^2} - \frac{du}{C_m} \\ -\frac{P dP}{\rho_m^2 C_m^2 c_{vm} T} + \frac{dT}{T} \\ -\frac{\phi_g}{\rho_g \rho_m C_g^2 C_m^2} \left(\rho_g C_g^2 - \rho_m C_m^2 + \frac{\beta_g^2 P}{\rho_m c_{vm}} \right) dP + d\phi_g \\ -\frac{\phi_v}{\rho_v \rho_m C_v^2 C_m^2} \left(\rho_v C_v^2 - \rho_m C_m^2 + \frac{\beta_v^2 P}{\rho_m c_{vm}} \right) dP + d\phi_v \\ \frac{dP}{\rho_m C_m^2} + \frac{du}{C_m} \end{bmatrix}. \quad (3.31)$$

3.5 Riemann Problem for Idealized Fluid-Mixture

The Riemann problem is characterized by uniform initial conditions except for a discontinuity at $x = 0$ on an infinite one-dimensional domain. The lack of an intrinsic length or time scale means that the solution to the Riemann problem is self-similar. The solution of the Riemann problem for scalar conservation laws, linear hyperbolic systems of equations, and the single phase Euler equations can be derived, see, e.g., [78] and [141]. For this reason, the Riemann problem is often used to verify numerical methods. In this section, the solution of the Riemann problem for the idealized mixture is presented.

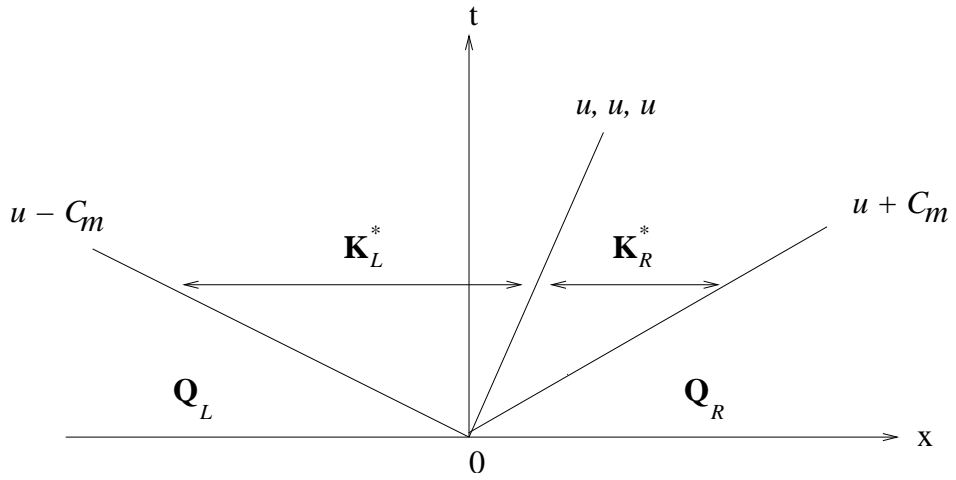


Figure 3.1: Structure of the solution of the Riemann problem for the idealized-mixture formulation.

Let us consider the initial conditions

$$\mathbf{Q}(x, 0) = \begin{cases} \mathbf{Q}_L & \text{if } x < 0, \\ \mathbf{Q}_R & \text{if } x \geq 0, \end{cases} \quad (3.32)$$

where $\mathbf{Q} = [\rho_m, \rho_m u, \rho_m e_{mT}, \rho_m Y_g, \rho_m Y_v]^T$. The solution of the Riemann problem involves expansion waves, shock waves, and a contact discontinuity. The structure of the solution is shown in Figure 3.1. The four regions with constant solutions are separated by five wave families. The challenge in finding the solution of the Riemann problem lies in determining the unknown states \mathbf{Q}_L^* and \mathbf{Q}_R^* to the left and right of the contact discontinuity, see Figure 3.1. These regions are referred to as the left and right star regions, respectively. The corresponding unknown primitive variables are

$$\mathbf{K}_L^* = [P_L^*, u_L^*, T_L^*, Y_{gL}^*, Y_{vL}^*]^T, \quad (3.33)$$

$$\mathbf{K}_R^* = [P_R^*, u_R^*, T_R^*, Y_{gR}^*, Y_{vR}^*]^T. \quad (3.34)$$

There are four possible wave patterns in the solution of the Riemann problem as shown in Figure 3.2, see, e.g, Toro [141]. These wave patterns are considered in constructing the exact solution. The eigenstructure of the mixture formulation reveals

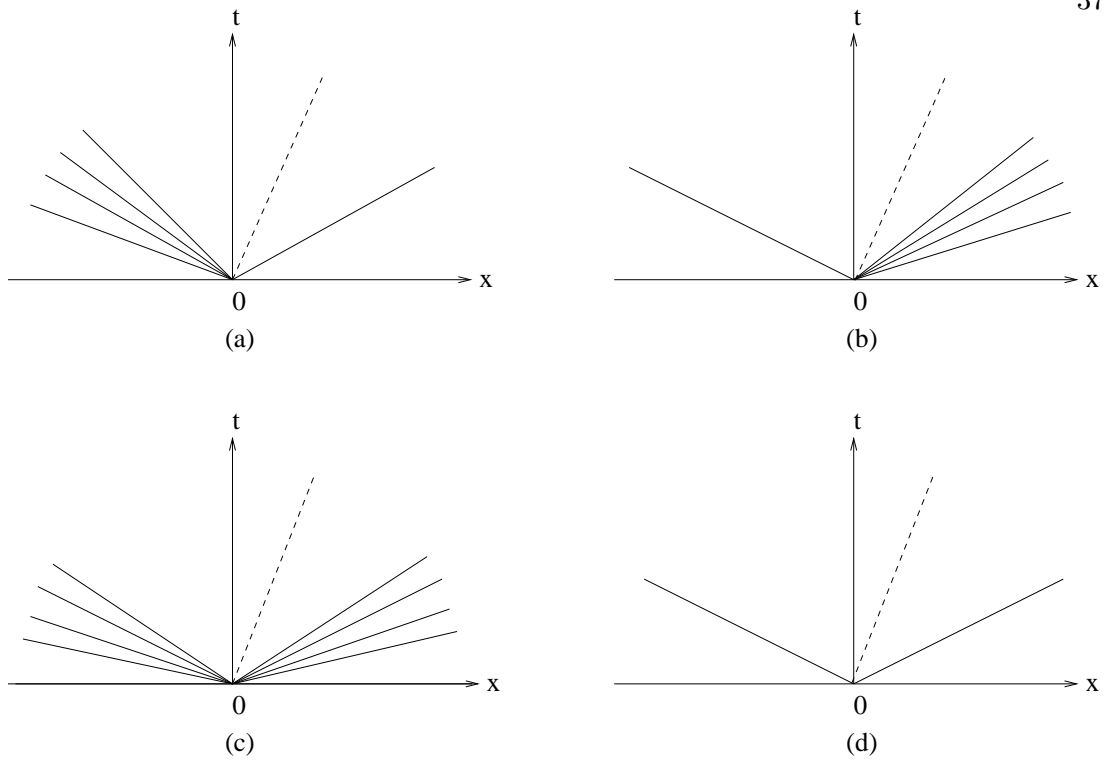


Figure 3.2: Four possible wave patterns of the solution of the Riemann problem [141]: (a) left rarefaction, contact, and right shock; (b) left shock, contact, and right rarefaction; (c) left rarefaction, contact, and right rarefaction; (d) left shock, contact, and right shock.

that the pressure P^* and velocity u^* are constant across the contact discontinuity, while other thermodynamic variables such as ρ_m^* and T^* are discontinuous. The unknown variables \mathbf{K}_L^* and \mathbf{K}_R^* are connected by the condition that the pressure P^* and velocity u^* are constant across the contact discontinuity. In the following, detailed analyses of the conditions across the left shock wave and left rarefaction wave, denoted by a subscript L , are presented. The conditions across the right shock and right rarefaction wave can be obtained by replacing the subscript L by R .

3.5.1 Left Shock Wave Analysis

The left wave is assumed to be a shock wave moving with speed S_L , see Figure 3.2(b) and (d). The pre-shock variables are P_L, u_L, T_L, Y_{gL} , and Y_{vL} . The post-shock

variables are P_L^* , u_L^* , T_L^* , Y_{gL}^* , and Y_{vL}^* . The Rankine-Hugoniot conditions are applied across the left shock, leading to

$$\rho_{mL}u_L - \rho_{mL}^*u_L^* = S_L(\rho_{mL} - \rho_{mL}^*), \quad (3.35)$$

$$(\rho_{mL}u_L^2 + P_L) - (\rho_{mL}^*u_L^{*2} + P_L^*) = S_L(\rho_{mL}u_L - \rho_{mL}^*u_L^*), \quad (3.36)$$

$$(\rho_{mL}e_{mL}u_L + P_Lu_L) - (\rho_{mL}^*e_{mL}^*u_L^* + P_L^*u_L^*) = S_L(\rho_{mL}e_{mL} - \rho_{mL}^*e_{mL}^*), \quad (3.37)$$

$$\rho_{mL}Y_{gL}u_L - \rho_{mL}^*Y_{gL}^*u_L^* = S_L(\rho_{mL}Y_{gL} - \rho_{mL}^*Y_{gL}^*), \quad (3.38)$$

$$\rho_{mL}Y_{vL}u_L - \rho_{mL}^*Y_{vL}^*u_L^* = S_L(\rho_{mL}Y_{vL} - \rho_{mL}^*Y_{vL}^*). \quad (3.39)$$

Equations (3.35)-(3.39) can be solved to give

$$u_L^* = u_L - f_L(P_L^*, \rho_{mL}^*, \mathbf{Q}_L), \quad (3.40)$$

$$g_L(P_L^*, \rho_{mL}^*, T_L^*, \mathbf{Q}_L) = 0, \quad (3.41)$$

$$Y_{iL}^* = Y_{iL}, \quad (3.42)$$

$$c_{vmL}^* = c_{vmL}, \quad (3.43)$$

where

$$f_L(P_L^*, \rho_{mL}^*, \mathbf{Q}_L) = \left[\frac{(P_L^* - P_L)(\rho_{mL}^* - \rho_{mL})}{\rho_{mL}\rho_{mL}^*} \right]^{\frac{1}{2}}, \quad (3.44)$$

and

$$g_L(P_L^*, \rho_{mL}^*, T_L^*, \mathbf{Q}_L) = c_{vmL}T_L - c_{vmL}^*T_L^* - \frac{1}{2}(P_L + P_L^*) \left(\frac{1}{\rho_{mL}^*} - \frac{1}{\rho_{mL}} \right). \quad (3.45)$$

3.5.2 Right Shock Wave Analysis

The analysis is analogous to that for the left shock wave. By replacing the subscript L by R , the following conditions are obtained,

$$u_R^* = u_R - f_R(P_R^*, \rho_{mR}^*, \mathbf{Q}_R), \quad (3.46)$$

$$g_R(P_R^*, \rho_{mR}^*, T_R^*, \mathbf{Q}_R) = 0, \quad (3.47)$$

$$Y_{iR}^* = Y_{iR}, \quad (3.48)$$

$$c_{vmR}^* = c_{vmR}, \quad (3.49)$$

where

$$f_R(P_R^*, \rho_{mR}^*, \mathbf{Q}_R) = \left[\frac{(P_R^* - P_R)(\rho_{mR}^* - \rho_{mR})}{\rho_{mR}\rho_{mR}^*} \right]^{\frac{1}{2}}, \quad (3.50)$$

and

$$g_R(P_R^*, \rho_{mR}^*, T_R^*, \mathbf{Q}_R) = c_{vmR}T_R - c_{vmR}^*T_R^* - \frac{1}{2}(P_R + P_R^*) \left(\frac{1}{\rho_{mR}^*} - \frac{1}{\rho_{mR}} \right). \quad (3.51)$$

3.5.3 Left Rarefaction Wave Analysis

Let us assume that the left wave is a rarefaction wave, see Figure 3.2(a) and (c).

Then the unknown state \mathbf{K}_L^* is connected to the known left state \mathbf{Q}_L using the isentropic relation given by Eq. (3.23) and the generalized Riemann invariants for the left wave.

The Riemann invariant across the left rarefaction is given by

$$d\Upsilon_1 = 0 = \frac{dP}{\rho_m C_m^2} - \frac{du}{C_m}, \quad (3.52)$$

from Eq. (3.31). Integration across the left rarefaction yields

$$u_L^* = u_L + f_L(P_L^*, \rho_{mL}^*, \mathbf{Q}_L), \quad (3.53)$$

where

$$f_L(P_L^*, \rho_{mL}^*, \mathbf{Q}_L) = \int_L^* \frac{dP}{\rho_m C_m}. \quad (3.54)$$

The integral in Eq. (3.54) is evaluated using adaptive Simpson quadrature [88] due to the complexity of the integrand.

Similarly, from Eq. (3.21) the following is obtain for isentropic conditions the non-linear algebraic equation

$$\begin{aligned} g_L(P_L^*, T_L^*, \mathbf{Q}_L) &= \left[c_{vm} \ln \frac{T}{T^r} \right]_L^* + \left[a_1 + \frac{Y_l}{\alpha} \right]_L^* - \frac{1}{\alpha} \left[Y_l \ln \left(\frac{\rho_l}{\rho_l^r} \right) \right]_L^* \\ &- \left[a_1 \ln \left(\frac{z}{z^r} \right) \right]_L^* - \frac{\rho_0}{\alpha} \left[\frac{Y_l}{\rho_l} \right]_L^* + \sum_{i=l,g,v} \frac{L_i^r}{T^r} \left[Y_i \right]_L^* = 0, \end{aligned} \quad (3.55)$$

where square brackets denote the following operation $[(\cdot)]_L^* = (\cdot)_L^* - (\cdot)_L$.

3.5.4 Right Rarefaction Wave Analysis

The analysis is analogous to that for the left rarefaction wave, except that the Riemann invariant across the right rarefaction is given by

$$d\Upsilon_5 = 0 = \frac{dP}{\rho_m C_m^2} + \frac{du}{C_m}, \quad (3.56)$$

from Eq. (3.31). By replacing the subscript L by R , the following conditions are obtained,

$$u_R^* = u_R - f_R(P_R^*, \rho_{mR}^*, \mathbf{Q}_R), \quad (3.57)$$

where

$$f_R(P_R^*, \rho_{mR}^*, \mathbf{Q}_R) = \int_R^* \frac{dP}{\rho_m C_m}, \quad (3.58)$$

and

$$\begin{aligned} g_R(P_R^*, T_R^*, \mathbf{Q}_R) &= \left[c_{vm} \ln \frac{T}{T^r} \right]_R^* + \left[a_1 + \frac{Y_l}{\alpha} \right]_R^* - \frac{1}{\alpha} \left[Y_l \ln \left(\frac{\rho_l}{\rho_l^r} \right) \right]_R^* \\ &- \left[a_1 \ln \left(\frac{z}{z^r} \right) \right]_R^* - \frac{\rho_0}{\alpha} \left[\frac{Y_l}{\rho_l} \right]_R^* + \sum_{i=l,g,v} \frac{L_i^r}{T^r} \left[Y_i \right]_R^* = 0 \end{aligned} \quad (3.59)$$

where square brackets denote the following operation $\left[(\cdot) \right]_R^* = (\cdot)_R^* - (\cdot)_R$.

3.5.5 Complete Solution

Now the conditions for all four possible wave patterns, shown in Figure 3.2, can be determined. The unknown states \mathbf{K}_L^* and \mathbf{K}_R^* can be computed by utilizing the condition that the pressure and velocity are constant across the contact discontinuity, i.e.

$$P_L^* = P_R^* = P^*, \quad (3.60)$$

and

$$u_L^* = u_R^* = u^*. \quad (3.61)$$

By eliminating u^* from Eqs. (3.40) or (3.53) and (3.46) or (3.57), a single non-linear algebraic equation is obtained,

$$f_L(P^*, \rho_{mL}^*, \mathbf{Q}_L) + f_R(P^*, \rho_{mR}^*, \mathbf{Q}_R) + u_R - u_L = 0. \quad (3.62)$$

Note that Eq. (3.62) has three unknowns, namely, P^* , ρ_{mL}^* , and ρ_{mR}^* . To close the problem, Eqs. (3.41) and (3.55) for the state to the left of the contact discontinuity and Eqs. (3.47) and (3.59) for the state to the right of the contact discontinuity are used, in addition to Eq. (3.15). Therefore, the following four cases are considered.

1. If $P^* > P_L$ then a shock wave is traveling to the left and the function f_L is given by Eq. (3.44) supplemented by Eqs. (3.41) and (3.15) for the left star region.
2. If $P^* \leq P_L$ then a rarefaction wave is moving to the left and the function f_L is given by Eq. (3.54) supplemented by Eqs. (3.55) and (3.15) for the left star region.
3. If $P^* > P_R$ then a shock wave is traveling to the right and the function f_R is given by Eq. (3.50) supplemented by Eqs. (3.47) and (3.15) for the right star region.
4. If $P^* \leq P_R$ then a rarefaction wave is moving to the right and the function f_R is given by Eq. (3.58) supplemented by Eqs. (3.59) and (3.15) for the right star region.

The speed of the contact discontinuity can be determined from

$$u^* = \frac{1}{2}(u_L + u_R) + \frac{1}{2}[f_R(P^*, \rho_{mR}^*, \mathbf{Q}_R) - f_L(P^*, \rho_{mL}^*, \mathbf{Q}_L)]. \quad (3.63)$$

Chapter 4

Numerical Method for Simulation of Multiphase/Multicomponent Flows

This chapter presents the development of the numerical method for modeling and numerical simulation of multiphase and multicomponent flows. The numerical method is used to solve the governing equations of multiphase and multicomponent flows, which are systems of non-linear hyperbolic partial differential equations. Two advanced numerical scheme such as Roe's approximate Riemann solver [112] and the modified Harten, Lax and van Leer scheme (HLLC) [15] are extended to multiphase and multicomponent flows and used to capture shock waves and contact discontinuities.

4.1 Extended Roe's Approximate Riemann Solver

The Roe's approximate Riemann solver [112] is widely known in finding an approximate solution of the Riemann problem. The method has been applied to a variety of physical problems. For example, Toro [140] has used the method to solve reactive two-phase flow problems via a phase-splitting procedure, and Sainaulieu [116] has extended the method to a class of two-phase flow problems without phase-splitting.

In this thesis, the Roe's approximate Riemann solver is utilized and extended to the mixture of liquid, gas and vapor. The extended Roe scheme is used to compute the convective fluxes of the mixture. The flux at the cell interface is calculated by evaluating the change in flux associated with each wave strength component characterized by the

eigenvalues of the Jacobian matrix and the right characteristic vector. The convective fluxes of the gas and vapor are computed as suggested by [79] to ensure positivity. The face states required by the flux computation are computed from a simplified WENO scheme [58].

To demonstrate the Roe approach in calculating the fluxes at the cell interface, a one dimensional time dependent Euler equations for the mixture of liquid, gas and vapor is presented for simplicity. However, in the actual solver a three dimensional time dependent Euler equations for the mixture is solved.

Let us consider a Riemann problem for one dimensional time dependent Euler equations for the mixture of liquid, gas and vapor given by

$$\frac{\partial \mathbf{Q}}{\partial t} + \frac{\partial \mathbf{F}}{\partial x} = \mathbf{0}, \quad (4.1)$$

$$\mathbf{Q}(x, 0) = \begin{cases} \mathbf{Q}_L & \text{if } x < 0, \\ \mathbf{Q}_R & \text{if } x \geq 0, \end{cases} \quad (4.2)$$

where the vectors of conserved variables and fluxes are

$$\mathbf{Q} = \begin{bmatrix} \rho_m \\ \rho_m u \\ \rho_m e_{m_T} \\ \rho_g \phi_g \\ \rho_v \phi_v \end{bmatrix}, \quad \mathbf{F} = \begin{bmatrix} \rho_m u \\ \rho_m u^2 + P \\ (\rho_m e_{m_T} + P)u \\ \rho_g \phi_g u \\ \rho_v \phi_v u \end{bmatrix} \quad (4.3)$$

Roe linearized Eq. (4.1) by introducing the Jacobian matrix $\mathbf{A}(\mathbf{Q}) = \partial \mathbf{F} / \partial \mathbf{Q}$.

Using chain rule, Eq. (4.1) can be written as

$$\frac{\partial \mathbf{Q}}{\partial t} + \mathbf{A}(\mathbf{Q}) \frac{\partial \mathbf{Q}}{\partial x} = \mathbf{0} \quad (4.4)$$

Roe then replaced the Jacobian matrix $\mathbf{A}(\mathbf{Q})$ by a constant Jacobian matrix $\tilde{\mathbf{A}} = \tilde{\mathbf{A}}(\mathbf{Q}_L, \mathbf{Q}_R)$, which is a function of the left and right states. The original non-linear

system of equations (4.1) are replaced by a linearized system of equations with constant coefficients

$$\frac{\partial \mathbf{Q}}{\partial t} + \tilde{\mathbf{A}} \frac{\partial \mathbf{Q}}{\partial x} = \mathbf{0} \quad (4.5)$$

Now, the original Riemann problem Eq. (4.1) is replaced by the approximate Riemann problem

$$\frac{\partial \mathbf{Q}}{\partial t} + \tilde{\mathbf{A}} \frac{\partial \mathbf{Q}}{\partial x} = \mathbf{0}, \quad (4.6)$$

$$\mathbf{Q}(x, 0) = \begin{cases} \mathbf{Q}_L & \text{if } x < 0, \\ \mathbf{Q}_R & \text{if } x \geq 0, \end{cases} \quad (4.7)$$

which is then solved exactly. The initial condition of the approximate Riemann problem is the same from the original Riemann problem. The elements on the Roe Jacobian matrix $\tilde{\mathbf{A}}$ are the Roe average quantities. Furthermore, the Roe Jacobian matrix $\tilde{\mathbf{A}}$ must satisfy the following properties [141]:

1. Hyperbolicity of the system of equations: The linearized system of equations must preserve the mathematical character of the original non-linear system of equations. The Roe Jacobian matrix $\tilde{\mathbf{A}}$ must have real eigenvalues and complete set of linearly independent right eigenvectors.
2. The Roe Jacobian matrix $\tilde{\mathbf{A}}$ must be consistent with the exact Jacobian matrix \mathbf{A} :

$$\tilde{\mathbf{A}}(\mathbf{Q}, \mathbf{Q}) = \mathbf{A}(\mathbf{Q}) \quad (4.8)$$

3. Conservation across discontinuities:

$$\mathbf{F}(\mathbf{Q}_R) - \mathbf{F}(\mathbf{Q}_L) = \tilde{\mathbf{A}}(\mathbf{Q}_R - \mathbf{Q}_L) \quad (4.9)$$

The Riemann wave diagram used in the Roe scheme is shown in Figure 4.1. The contact wave, whose speed is denoted by S_M , separates the left, \mathbf{U}_L , and right, \mathbf{U}_R ,

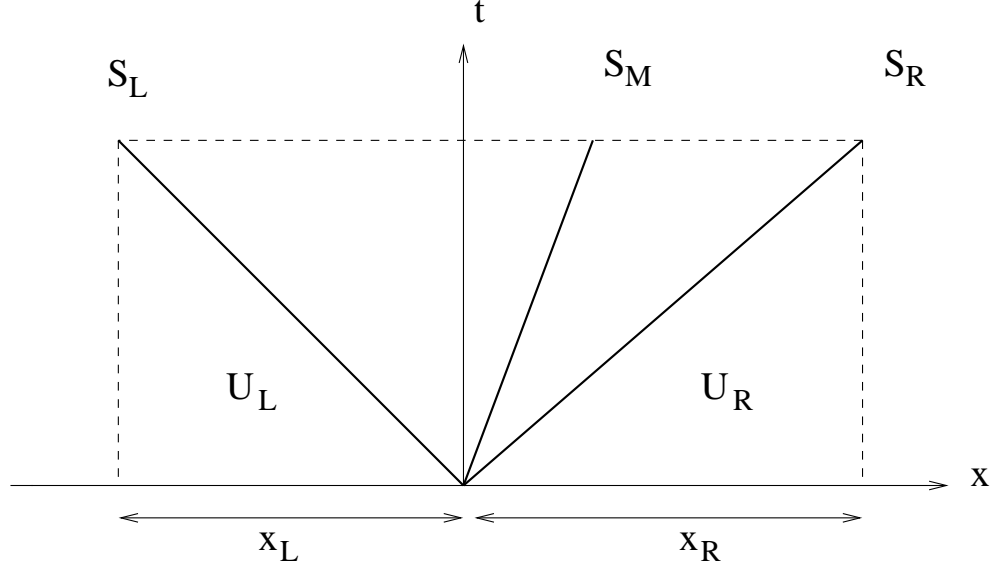


Figure 4.1: The Riemann wave diagram used in the Roe scheme.

states. The minimum and maximum velocities of the acoustic waves are denoted by S_L and S_R , respectively. In Roe's scheme, the approximate Riemann solution is defined as

$$\mathbf{U} = \begin{cases} \mathbf{U}_L & \text{if } S_L > 0, \\ \mathbf{U}_R & \text{if } S_R < 0, \end{cases} \quad (4.10)$$

where \mathbf{U} is the vector of the conserved variables defined similar to \mathbf{Q} in Eq. (4.3). The corresponding interface flux, \mathbf{F} , is defined as

$$\mathbf{F} = \begin{cases} \mathbf{F}_L & \text{if } S_L > 0, \\ \mathbf{F}_R & \text{if } S_R < 0. \end{cases} \quad (4.11)$$

The flux at the cell interface, $x/t = 0$ is given by

$$\mathbf{F}[\mathbf{Q}(0)] = \frac{1}{2} [\mathbf{F}(\mathbf{Q}_R) + \mathbf{F}(\mathbf{Q}_L)] - \frac{1}{2} \sum_{i=1}^n \tilde{\mathbf{r}}_i |\tilde{\lambda}_i| d\tilde{v}_i \quad (4.12)$$

where $\tilde{\mathbf{r}}_i$ are the right characteristic vectors, $\tilde{\lambda}_i$ are the eigenvalues of the system and $d\tilde{v}_i$ are the wave strengths or Riemann invariants.

In the following, the algorithm in calculating the fluxes at the cell interface using the Roe's approximate Riemann solver are outlined.

1. Given the conserved variables, $\mathbf{Q} = [\rho_m, \rho_m u, \rho_m e_{mT}, \rho_m Y_g, \rho_m Y_v]^T$, for the left (L) and right (R) states, the primitive variables, $\mathbf{K} = [P, u, T, Y_g, Y_v]^T$, for the left (L) and right (R) states are calculated in the following:

$$u = \frac{\rho_m u}{\rho_m}, \quad (4.13)$$

$$T = \frac{\rho_m e_{mT} - \frac{1}{2} \rho_m u^2}{\rho_m c_{vm}}, \quad (4.14)$$

$$Y_g = \frac{\rho_m Y_g}{\rho_m}, \quad (4.15)$$

$$Y_v = \frac{\rho_m Y_v}{\rho_m}, \quad (4.16)$$

and

$$P = \frac{\psi_1 - \psi_2 + \sqrt{(\psi_2 - \psi_1)^2 + 4\psi_2\psi_3}}{2}, \quad (4.17)$$

where

$$\begin{aligned} \psi_1 &= C_l^2 \left(\rho_o - \left(\frac{\beta_l}{C_l} \right)^2 (T - T_o) - \frac{P_o}{C_l^2} - \rho_m Y_l \right), \\ \psi_2 &= (\rho_m Y_v R_v + \rho_m Y_g R_g) T, \\ \psi_3 &= C_l^2 \left(\rho_o - \left(\frac{\beta_l}{C_l} \right)^2 (T - T_o) - \frac{P_o}{C_l^2} \right), \end{aligned}$$

2. Compute the Roe-average quantities of the mixture as follows:

$$\tilde{\rho}_m = R_\rho \rho_{mL}, \quad (4.18)$$

$$\tilde{u} = \frac{u_L + u_R R_\rho}{1 + R_\rho}, \quad (4.19)$$

$$\tilde{P} = \frac{P_L + P_R R_\rho}{1 + R_\rho}, \quad (4.20)$$

$$\tilde{T} = \frac{T_L + T_R R_\rho}{1 + R_\rho}, \quad (4.21)$$

$$\tilde{Y}_i = \frac{Y_{iL} + Y_{iR} R_\rho}{1 + R_\rho}, \quad (4.22)$$

$$\tilde{c}_{vm} = \sum_i \tilde{Y}_i c_{vi}. \quad (4.23)$$

where $R_\rho = \sqrt{\rho_{mR}/\rho_{mL}}$.

For the mixture speed of sound, the Roe-average is computed from Eq. (2.50)

$$\tilde{C}_m^2 = \frac{\tilde{\rho}_m \tilde{c}_{vm} + \tilde{P} \sum_i \frac{\tilde{\rho}_m \tilde{Y}_i}{\tilde{\rho}_i^2} \left(\frac{\tilde{\beta}_i}{\tilde{C}_i} \right)^2}{\tilde{\rho}_m^2 \tilde{c}_{vm} \sum_i \frac{\tilde{\rho}_m \tilde{Y}_i}{\tilde{\rho}_i^2} \frac{1}{\tilde{C}_i^2}}, \quad (4.24)$$

The remaining variables appearing in Eq. (4.24) are computed as $\tilde{\rho}_i = \rho_i(\tilde{P}, \tilde{T})$, $\tilde{\beta}_i = \beta_i(\tilde{P}, \tilde{T})$, and $\tilde{C}_i = C_i(\tilde{P}, \tilde{\rho}_i)$.

3. Compute the Roe-average wave speeds of the mixture. The Roe-average wave speeds are the eigenvalues of the systems from Eq. (2.49) in one dimension.

$$\lambda_1 = \tilde{u} - \tilde{C}_m, \quad (4.25)$$

$$\lambda_2 = \tilde{u}, \quad (4.26)$$

$$\lambda_3 = \tilde{u}, \quad (4.27)$$

$$\lambda_4 = \tilde{u}, \quad (4.28)$$

$$\lambda_5 = \tilde{u} + \tilde{C}_m. \quad (4.29)$$

4. Compute the wave strengths of the mixture. The wave strengths are computed using the relation $\Delta \mathbf{v} = \boldsymbol{\Pi} \Delta \mathbf{K}$, where \mathbf{K} are the primitive variables, and $\boldsymbol{\Pi}$ are the eigenvectors of the system. The resulting wave strengths are

$$\Delta v_1 = \frac{1}{\tilde{\rho}_m \tilde{C}_m^2} \Delta P - \frac{1}{\tilde{C}_m} \Delta u, \quad (4.30)$$

$$\Delta v_2 = -\frac{\tilde{P}}{\tilde{\rho}_m \tilde{C}_m^2 \tilde{\rho}_m \tilde{c}_{vm} \tilde{T}} \Delta P + \frac{1}{\tilde{T}} \Delta T, \quad (4.31)$$

$$\Delta v_3 = -\frac{\tilde{\phi}_g}{\tilde{\rho}_g \tilde{C}_g^2 \tilde{\rho}_m \tilde{C}_m^2} \left[\tilde{\rho}_g \tilde{C}_g^2 - \tilde{\rho}_m \tilde{C}_m^2 + \frac{\tilde{\beta}_g^2 \tilde{P}}{\tilde{\rho}_m \tilde{c}_{vm}} \right] \Delta P + \Delta \phi_g, \quad (4.32)$$

$$\Delta v_4 = -\frac{\tilde{\phi}_v}{\tilde{\rho}_v \tilde{C}_v^2 \tilde{\rho}_m \tilde{C}_m^2} \left[\tilde{\rho}_v \tilde{C}_v^2 - \tilde{\rho}_m \tilde{C}_m^2 + \frac{\tilde{\beta}_v^2 \tilde{P}}{\tilde{\rho}_m \tilde{c}_{vm}} \right] \Delta P + \Delta \phi_v, \quad (4.33)$$

$$\Delta v_5 = \frac{1}{\tilde{\rho}_m \tilde{C}_m^2} \Delta P + \frac{1}{\tilde{C}_m} \Delta u. \quad (4.34)$$

where $\Delta P = P_R - P_L$, $\Delta T = T_R - T_L$, $\Delta u = u_R - u_L$, $\Delta \phi_g = \phi_{gR} - \phi_{gL}$ and $\Delta \phi_v = \phi_{vR} - \phi_{vL}$.

5. Compute the right characteristic vectors. The right characteristic vectors are as follows (note: all the quantities are in Roe-average) :

$$\mathbf{r}_1 = \begin{bmatrix} -\left(\frac{\beta_\phi^2}{C_\phi^2}\right)T \\ -\left(\frac{\beta_\phi^2}{C_\phi^2}\right)Tu \\ \rho_l \phi_l c_{vl} T + \beta c_{vl} T^2 \phi_l - \frac{1}{2} \left(\frac{\beta_\phi^2}{C_\phi^2}\right) Tu^2 \\ -\frac{\beta_g^2 \phi_g T}{C_g^2} \\ -\frac{\beta_v^2 \phi_v T}{C_v^2} \end{bmatrix}, \quad \mathbf{r}_2 = \begin{bmatrix} \rho_g - \rho_l \\ (\rho_g - \rho_l)u \\ \rho_g e_g - \rho_l e_l \\ \rho_g \\ 0 \end{bmatrix}, \quad (4.35)$$

$$\mathbf{r}_3 = \begin{bmatrix} \rho_v - \rho_l \\ (\rho_v - \rho_l)u \\ \rho_v e_v - \rho_l e_l \\ 0 \\ \rho_v \end{bmatrix}, \quad \mathbf{r}_4 = \begin{bmatrix} \Pi_1 \\ \Pi_1 u - \frac{\rho_m C_m}{2} \\ \Pi_2 - \frac{\rho_m C_m u}{2} \\ \frac{\rho_g \phi_g}{2} \\ \frac{\rho_v \phi_v}{2} \end{bmatrix}, \quad \mathbf{r}_5 = \begin{bmatrix} \Pi_1 \\ \Pi_1 u + \frac{\rho_m C_m}{2} \\ \Pi_2 + \frac{\rho_m C_m u}{2} \\ \frac{\rho_g \phi_g}{2} \\ \frac{\rho_v \phi_v}{2} \end{bmatrix}, \quad (4.36)$$

where

$$\begin{aligned} \Pi_1 &= \frac{\rho_m C^2}{2C_\phi^2} - \frac{1}{2} \left(\frac{\beta_\phi^2}{C_\phi^2}\right) \frac{P}{\rho_m c_{vm}} + \frac{(\rho_g - \rho_l)\phi_g}{2\rho_g C_g^2} \left[\rho_g C_g^2 - \rho_m C_m^2 + \frac{\beta_g^2 P}{\rho_m c_{vm}} \right] + \\ &\quad \frac{(\rho_v - \rho_l)\phi_v}{2\rho_v C_v^2} \left[\rho_v C_v^2 - \rho_m C_m^2 + \frac{\beta_v^2 P}{\rho_m c_{vm}} \right], \end{aligned} \quad (4.37)$$

$$\begin{aligned} \Pi_2 &= \frac{\rho_m C_m^2}{2} \left[\frac{e_l \phi_l}{C_l^2} + \frac{e_v \phi_v}{C_v^2} \frac{e_g \phi_g}{C_g^2} \right] + \frac{P}{2\rho_m c_{vm}} \left[\rho_l \phi_l c_{vl} + \beta_T c_{vl} \phi_l T - \frac{1}{2} \left(\frac{\beta_\phi^2}{C_\phi^2}\right) u^2 \right] + \\ &\quad \frac{(\rho_g e_g - \rho_l e_l)\phi_g}{2\rho_g C_g^2} \left[\rho_g C_g^2 - \rho_m C_m^2 + \frac{\beta_g^2 P}{\rho_m c_{vm}} \right] + \\ &\quad \frac{(\rho_v e_v - \rho_l e_l)\phi_v}{2\rho_v C_v^2} \left[\rho_v C_v^2 - \rho_m C_m^2 + \frac{\beta_v^2 P}{\rho_m c_{vm}} \right], \end{aligned} \quad (4.38)$$

and

$$e_l = c_{vl}T + \frac{1}{2}u^2, \quad (4.39)$$

$$e_v = c_{vv}T + \frac{1}{2}u^2, \quad (4.40)$$

$$e_g = c_{vg}T + \frac{1}{2}u^2. \quad (4.41)$$

6. Finally, calculate the flux at $x/t = 0$

$$\mathbf{F}[\mathbf{Q}(0)] = \frac{1}{2}[\mathbf{F}(\mathbf{Q}_R) + \mathbf{F}(\mathbf{Q}_L)] - \frac{1}{2}\sum_{i=1}^n \tilde{\mathbf{r}}_i |\tilde{\lambda}_i| d\tilde{v}_i \quad (4.42)$$

where $\frac{1}{2}[\mathbf{F}(\mathbf{Q}_R) + \mathbf{F}(\mathbf{Q}_L)]$ is the arithmetic average of the convective fluxes and $\frac{1}{2}\sum_{i=1}^n \tilde{\mathbf{r}}_i |\tilde{\lambda}_i| d\tilde{v}_i$ is the numerical dissipation, where $n = 5$.

Note that in the Roe's approximate Riemann solver, all three waves have zero spread, which means that the method cannot capture the finite spread of the expansion fan.

4.2 Extended HLLC Approximate Riemann Solver

Approximately two years after Roe's [112] breakthrough in developing an approximate Riemann solver, Harten, Lax, and van Leer [55] have devised a new approximate Riemann solver denoted as HLL scheme. In their scheme, a single state approximate Riemann solver can be constructed in a way that the entropy condition will be automatically satisfied and will yield an exact resolution of isolated shocks. A modification of the scheme was designed by Toro *et al.* [142], where a two-state approximate Riemann solver can be devised so that both shocks and contact waves will be resolved exactly. The modified scheme is called HLLC (C stands for Contact) Riemann solver. The scheme has been applied to many physical problems such as supersonic two dimensional, time dependent Euler equations [139] and two dimensional, time dependent shallow water equations [45]. Further improvement of the scheme was presented by Batten *et al.* [15], which show that with proper choice of acoustic and contact wave velocities, the HLLC

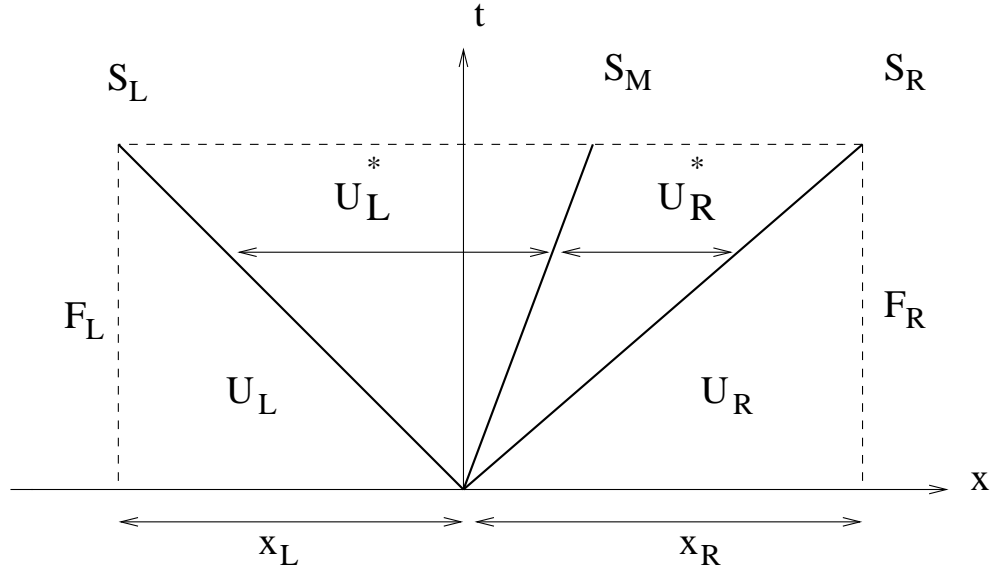


Figure 4.2: The simplified Riemann wave diagram with two intermediate states used in the HLLC scheme.

scheme will yield an exact resolution of isolated shock and contact waves. The resulting scheme is positively conservative, which forces the numerical method to preserve initially positive pressures and densities. For an in-depth description of the HLLC method, see [15], and [141].

In this thesis, the HLLC approximate Riemann solver of [15] is extended and is used to compute the convective fluxes of the mixture. The convective fluxes of the gas and vapor components are computed as suggested by [79] to ensure positivity. The face states required by the flux computation are computed from a simplified WENO scheme [58]. In the following, an outline of the extended HLLC approximate Riemann solver of [15] for the mixture of liquid, gas, and vapor is presented.

The simplified Riemann wave diagram with two intermediate states is illustrated in Figure 4.2. The two averaged intermediate states, \mathbf{U}_L^* and \mathbf{U}_R^* , are separated by a contact wave, whose speed is denoted by S_M . The acoustic waves have the minimum and maximum velocities, S_L and S_R respectively, of all waves exist in the exact solution.

The flow is supersonic from left to right if $S_L > 0$, and the upwind flux is defined from $F = F(U_L)$, where U_L is the left states. Conversely, the flow is supersonic from right to left if $S_R < 0$, and the flux is defined from $F = F(U_R)$, where U_R is the right states. Harten, Lax, and van Leer [56] defined the two-state approximate Riemann solution,

\mathbf{U}_{HLLC} as

$$\mathbf{U}_{HLLC} = \begin{cases} \mathbf{U}_L & \text{if } S_L > 0, \\ \mathbf{U}_L^* & \text{if } S_L \leq 0 < S_M, \\ \mathbf{U}_R^* & \text{if } S_M \leq 0 \leq S_R, \\ \mathbf{U}_R & \text{if } S_R < 0, \end{cases} \quad (4.43)$$

where \mathbf{U} is the vector of the conserved variables defined similar to \mathbf{Q} in Eq. (2.6). The corresponding interface flux, \mathbf{F}_{HLLC} , is defined as

$$\mathbf{F}_{HLLC} = \begin{cases} \mathbf{F}_L & \text{if } S_L > 0, \\ \mathbf{F}_L^* & \text{if } S_L \leq 0 < S_M, \\ \mathbf{F}_R^* & \text{if } S_M \leq 0 \leq S_R, \\ \mathbf{F}_R & \text{if } S_R < 0. \end{cases} \quad (4.44)$$

The two intermediate states \mathbf{U}_L^* and \mathbf{U}_R^* are determined following the approach suggested by Toro *et al.* [142], which assumed constant velocity particle between the acoustic waves. Applying the Rankine-Hugoniot conditions across the S_L waves and simplifying yields

$$\mathbf{F}_L^* = \mathbf{F}_L + S_L(\mathbf{U}_L^* - \mathbf{U}_L), \quad (4.45)$$

$$S_L \mathbf{U}_L^* - \mathbf{F}_L^* = S_L \mathbf{U}_L - \mathbf{F}_L. \quad (4.46)$$

Similarly, for the S_R waves yields

$$\mathbf{F}_R^* = \mathbf{F}_R + S_R(\mathbf{U}_R^* - \mathbf{U}_R), \quad (4.47)$$

$$S_R \mathbf{U}_R^* - \mathbf{F}_R^* = S_R \mathbf{U}_R - \mathbf{F}_R. \quad (4.48)$$

To compute \mathbf{U}_L^* and \mathbf{F}_L^* , Batten *et al.* [15] made a specific assumption such that

$$S_M = q_L^* = q_R^* = q^*, \quad (4.49)$$

where q^* is the average directed velocity between the two acoustic waves, and

$$S_M = \frac{\rho_R q_R (S_R - q_R) - \rho_L q_L (S_L - q_L) + P_L - P_R}{\rho_R (S_R - q_R) - \rho_L (S_L - q_L)}. \quad (4.50)$$

The wave speeds S_L and S_R are computed from

$$S_L = \min[q_L - C_{mL}, \bar{q} - \bar{C}_m], \quad (4.51)$$

$$S_R = \max[q_R + C_{mR}, \bar{q} + \bar{C}_m], \quad (4.52)$$

where q_L , q_R , C_{mL} , and C_{mR} are the face-normal velocities and the speeds of sound of the mixture at the left and right state, respectively, and \tilde{q} is the Roe-averaged [112] face-normal velocity.

The primary difficulty in extending the HLLC method to multiphase and multi-component flows is due to the treatment of the speed of sound of the mixture. In the HLLC method of [15] for single-phase flow, \tilde{C}_m is computed from the constant ratio of specific heats and the Roe-averaged total enthalpy and velocities. For the multiphase and multicomponent mixtures considered in this thesis, this is not possible because the speed of sound given by Eq. (2.50) cannot be related to the total enthalpy in a straightforward fashion. Instead, the following is proposed to compute \tilde{C}_m from Eq. (2.50)

as

$$\tilde{C}_m^2 = \frac{\tilde{\rho}_m \tilde{c}_{vm} + \tilde{P} \sum_i \frac{\tilde{\rho}_m \tilde{Y}_i}{\tilde{\rho}_i^2} \left(\frac{\tilde{\beta}_i}{\tilde{C}_i} \right)^2}{\tilde{\rho}_m^2 \tilde{c}_{vm} \sum_i \frac{\tilde{\rho}_m \tilde{Y}_i}{\tilde{\rho}_i^2} \frac{1}{\tilde{C}_i^2}}, \quad (4.53)$$

where, using the definition,

$$R_\rho = \sqrt{\rho_{mR}/\rho_{mL}}, \quad (4.54)$$

the Roe-averaged of the mixture density is defined as

$$\tilde{\rho}_m = R_\rho \rho_{mL}, \quad (4.55)$$

and the Roe-averaged mass fractions is given by,

$$\tilde{Y}_i = \frac{Y_{iL} + Y_{iR} R_\rho}{1 + R_\rho}. \quad (4.56)$$

Moreover, the Roe-averaged of the specific heat at constant volume of the mixture is defined as

$$\tilde{c}_{vm} = \sum_i \tilde{Y}_i c_{vi}. \quad (4.57)$$

In addition, for lack of a better approach, the mixture pressure and temperature is defined as,

$$\tilde{P} = \frac{P_L + P_R R_\rho}{1 + R_\rho}, \quad (4.58)$$

and

$$\tilde{T} = \frac{T_L + T_R R_\rho}{1 + R_\rho}, \quad (4.59)$$

respectively. The remaining variables appearing in Eq. (4.53) are computed as $\tilde{\rho}_i = \rho_i(\tilde{P}, \tilde{T})$, $\tilde{\beta}_i = \beta_i(\tilde{P}, \tilde{T})$, and $\tilde{C}_i = C_i(\tilde{P}, \tilde{\rho}_i)$.

Chapter 5

Code Verification and Model Validation

The new developed solver for simulation of multiphase and multicomponent flows is verified and validated by solving some benchmark problems including the novel benchmark problems for the idealized fluid-mixture model. The problems considered are:

1. Single-phase two-component shock-tube problem: Tests the accuracy with which shock waves and contact discontinuities are captured.
2. Shock-wave propagation in a single-phase two-component fluid: Tests the accuracy of computing the shock wave refraction at a component interface.
3. Two-phase single-component shock-tube problem for idealized-fluid mixture: Tests the accuracy with which two-phase flows are solved if all solution variables are discontinuous.
4. Two-phase single-component rarefaction problem for idealized fluid mixture: Tests the accuracy for low-density flows.
5. Single-phase two-component shock-bubble interaction: Demonstrates the ability to solve the interaction of a shock-wave and a material interface in two dimensions.

For the first four problems, the accuracy is assessed by comparing the numerical solutions to the appropriate exact solutions. For the fifth problem, the accuracy is evaluated

by comparing the results to the experiments of Haas and Sturtevant [53] and the simulations of Quirk and Karni [105].

5.1 Single-Phase Two-Component Shock-Tube Problem

The initial conditions correspond to two different ideal gases [70, 1, 79, 71, 138],

$$\mathbf{Q}(x, 0) = \begin{cases} \mathbf{Q}_L & \text{if } x < 0.5, \\ \mathbf{Q}_R & \text{if } x \geq 0.5, \end{cases} \quad (5.1)$$

where $\mathbf{Q} = [\rho_m, u, P, \gamma_m, Y_1, Y_2]^T$ and

$$\begin{aligned} \mathbf{Q}_L &= [1.000, 0.0, 1.0 \cdot 10^5, 1.4, 1.0, 0.0]^T, \\ \mathbf{Q}_R &= [0.125, 0.0, 1.0 \cdot 10^4, 1.2, 0.0, 1.0]^T. \end{aligned} \quad (5.2)$$

The primary difficulty is the capturing of the contact discontinuity without oscillations. The computational domain $0 \leq x \leq 1$ is discretized uniformly with 1000 cells. Excellent agreement between the numerical and exact solutions is obtained as shown in Figure 5.1. In particular, the results do not exhibit oscillations like the results presented in [71].

5.2 Shock-Wave Propagation in a Single-Phase Two-Component Fluid

The problem suggested by [71] is considered, in which a shock wave refracts at a gas interface, leading to a transmitted and a reflected shock wave. The transmitted shock wave may travel faster or slower than the incident shock wave depending on the sound speeds of the respective gases. The reflected wave is either a shock wave or a rarefaction wave depending on the ratio of the acoustic impedances [29, 61]. The interface is set into motion by the shock wave.

The initial conditions correspond to a weak shock wave with a Mach number

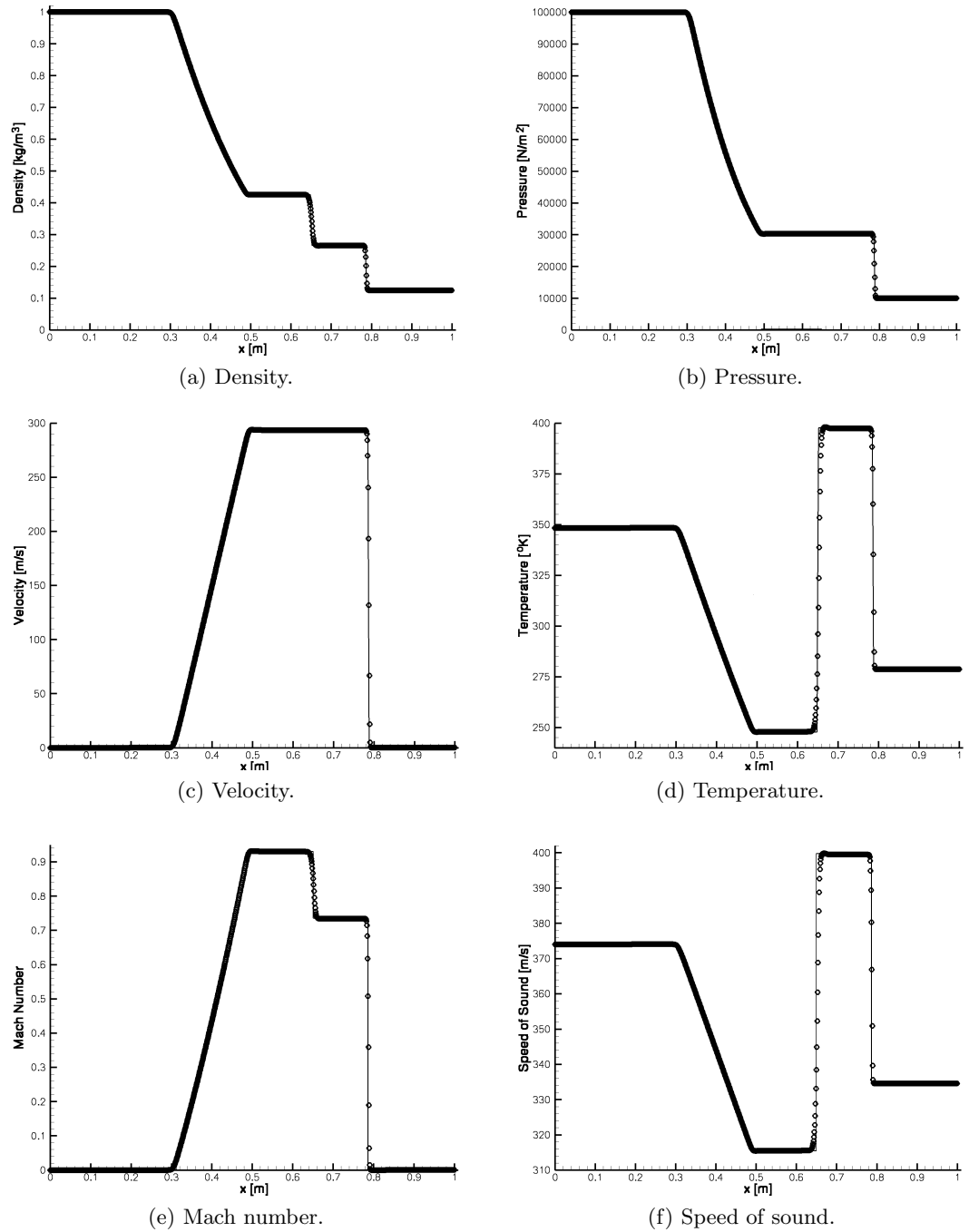


Figure 5.1: Comparison of numerical (\circ) and exact (solid line) solutions for single-phase two-component shock-tube problem at $t \approx 517 \mu\text{s}$. Number of cells = 1000.

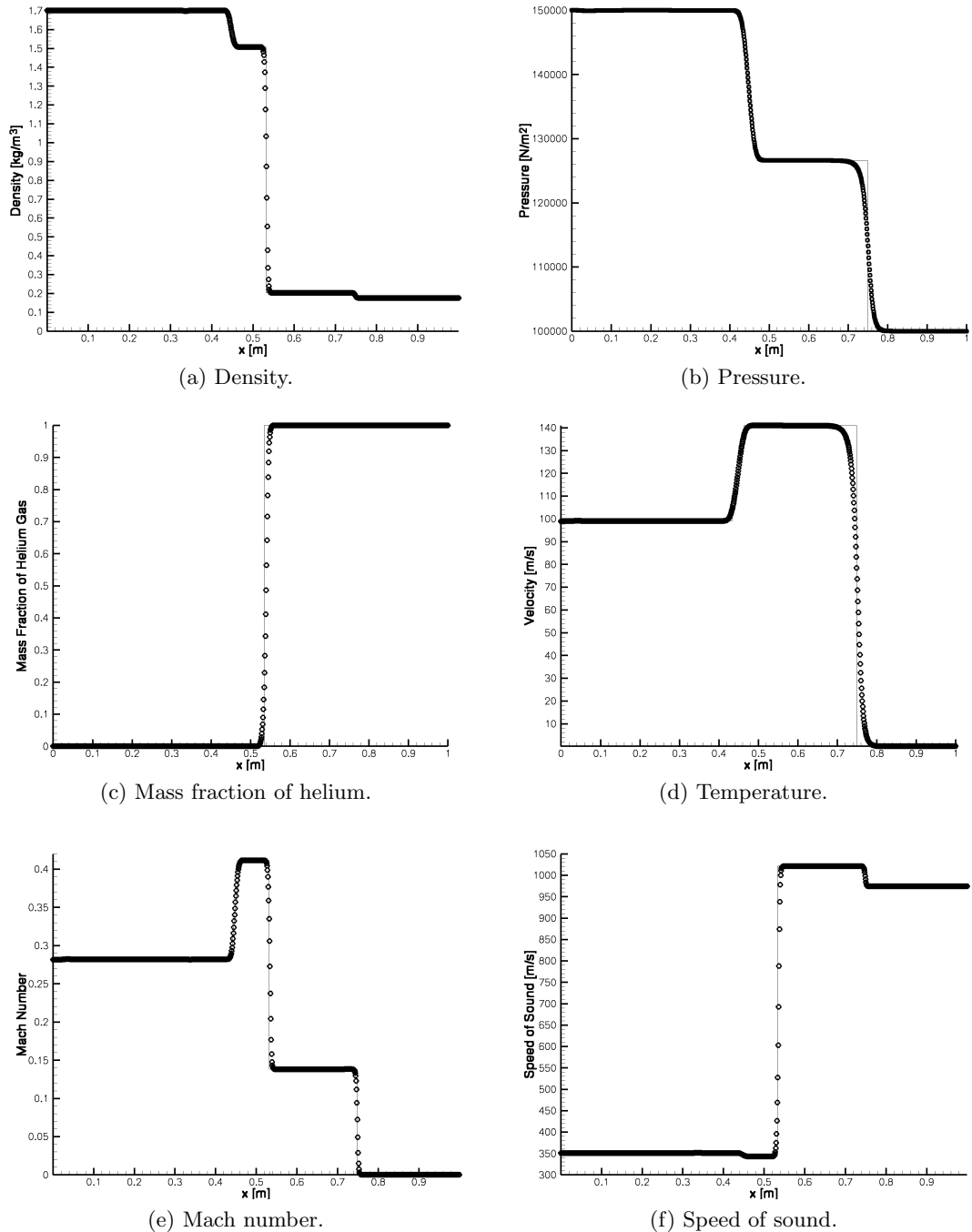


Figure 5.2: Comparison of numerical (○) and exact (solid line) solution for shock-wave propagation in a single-phase two-component fluid at $t \approx 864 \mu\text{s}$. Number of cells = 1000.

$M_s = 1.1952$ in air propagating toward a region occupied by helium,

$$\mathbf{Q}(x, 0) = \begin{cases} \mathbf{Q}_{A1} & \text{if } 0.0 \leq x < 0.25, \\ \mathbf{Q}_{A2} & \text{if } 0.25 \leq x < 0.5, \\ \mathbf{Q}_{He} & \text{if } 0.5 \leq x, \leq 1.0 \end{cases} \quad (5.3)$$

where $\mathbf{Q} = [\rho_m, u, P, \gamma_m, Y_1, Y_2]^T$ and

$$\begin{aligned} \mathbf{Q}_{A1} &= [1.7017, 98.956, 1.5 \cdot 10^5, 1.40, 1.0, 0.0]^T, \\ \mathbf{Q}_{A2} &= [1.2763, 0.000, 1.0 \cdot 10^5, 1.40, 0.0, 1.0]^T, \\ \mathbf{Q}_{He} &= [0.1760, 0.000, 1.0 \cdot 10^5, 1.67, 0.0, 1.0]^T. \end{aligned} \quad (5.4)$$

The vectors \mathbf{Q}_{A1} , \mathbf{Q}_{A2} , and \mathbf{Q}_{He} correspond to the post-shock variables in air, pre-shock variables in air, and pre-shock variables in helium, respectively. For these initial conditions, the transmitted shock wave is very weak and the reflected wave is a slender rarefaction wave. The computational domain $0 \leq x \leq 1$ is discretized uniformly with 1000 cells.

Figure 5.2 shows the comparison of the numerical and exact solution at $t \approx 864 \mu\text{s}$. As for the first test problem, the results exhibit no oscillations like those presented by [71]. The transmitted shock wave travels faster than the incident shock wave since the acoustic speed in helium is greater than the acoustic speed in air.

5.3 Two-Phase Shock-Tube Problem for Idealized Fluid Mixture

The two-phase shock-tube problem of [121] is considered. The driver section contains a liquid at high pressure and the driven section contains a gas at low pressure. The initial conditions are

$$\mathbf{Q}(x, 0) = \begin{cases} \mathbf{Q}_L & \text{if } x < 0.7, \\ \mathbf{Q}_R & \text{if } x \geq 0.7, \end{cases} \quad (5.5)$$

where $\mathbf{Q} = [\rho_m, u, P, Y_1, Y_2]^T$ and

$$\begin{aligned} \mathbf{Q}_L &= [1500.0, 0.0, 1.12 \cdot 10^9, 1.0, 0.0]^T, \\ \mathbf{Q}_R &= [50.0, 0.0, 1.00 \cdot 10^5, 0.0, 1.0]^T. \end{aligned} \quad (5.6)$$

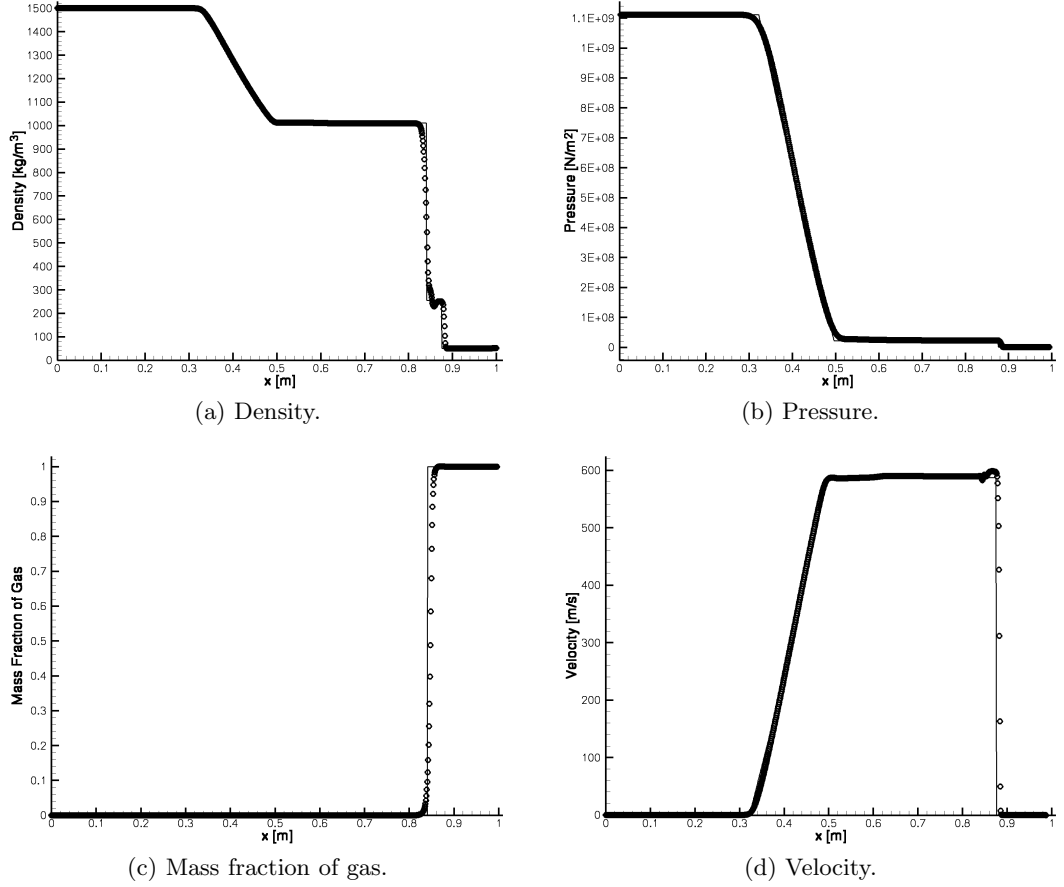


Figure 5.3: Comparison of numerical (○) and exact (solid line) solution for two-phase shock-tube problem for an idealized fluid mixture at $240 \mu\text{s}$. Number of cells = 1000.

Note that the problem is very stiff. The density and pressure differ by ratios of 30 and about 10^4 across the discontinuity, respectively. The computational domain $0 \leq x \leq 1$ is discretized uniformly with 1000 cells.

Figure 5.3 shows the comparison of the numerical and exact solution at $240 \mu\text{s}$. Small oscillations in the density and velocity between the contact discontinuity and shock wave are visible due to the proximity of the contact discontinuity and the shock wave. This was also observed by [121]. However, the solution shows no oscillations at the tail of the rarefaction wave.

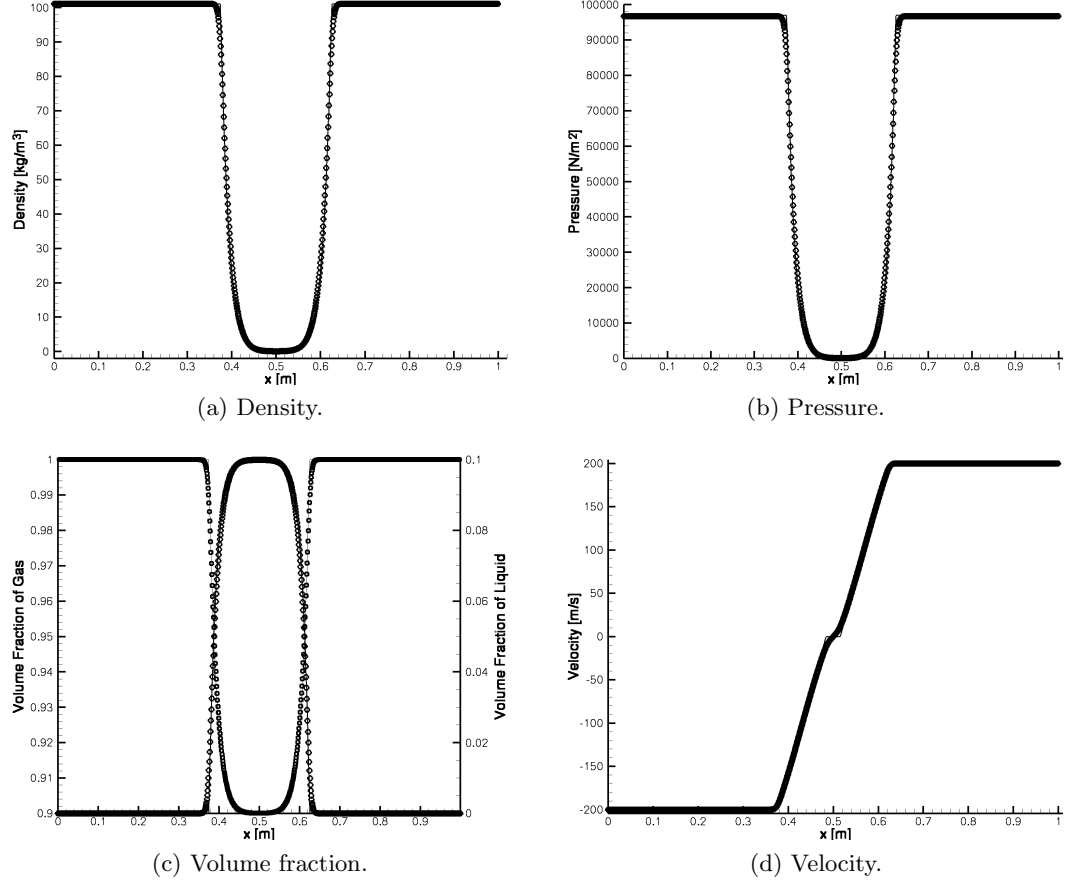


Figure 5.4: Comparison of numerical (○) and exact (solid line) solution for two-phase rarefaction problem for an idealized fluid mixture at $540 \mu\text{s}$. Number of cells = 1000.

5.4 Two-Phase Rarefaction Problem for Idealized Fluid Mixture

A two-phase rarefaction problem is considered. The solution consists of two symmetric rarefaction waves and a trivial stationary contact discontinuity. The initial conditions are

$$\mathbf{Q}(x, 0) = \begin{cases} \mathbf{Q}_L & \text{if } x < 0.5, \\ \mathbf{Q}_R & \text{if } x \geq 0.5, \end{cases} \quad (5.7)$$

where $\mathbf{Q} = [\rho_l, \phi_l, \rho_g, \phi_g, u, P]^T$ and

$$\begin{aligned} \mathbf{Q}_L &= [1000.0, 0.1, 1.2342, 0.9, -200.0, 9.7 \cdot 10^4]^T, \\ \mathbf{Q}_R &= [1000.0, 0.1, 1.2342, 0.9, 200.0, 9.7 \cdot 10^4]^T. \end{aligned} \quad (5.8)$$

Component	γ	R	c_v
Air	1.400	287.0	720.0
He	1.648	1578.0	244.0

Table 5.1: Properties of air and helium used in the simulations of shock-bubble interaction. Note that the helium is contaminated with 28% air and its properties have been adjusted accordingly.

The computational domain $0 \leq x \leq 1$ is discretized uniformly with 1000 cells. Figure 5.4 shows the comparison of the numerical and exact solution at $t = 540 \mu\text{s}$. No problems are encountered despite the low pressure and density.

5.5 Single-Phase Two-Component Shock-Bubble Interaction

Haas and Sturtevant [53] presented experiments of a weak planar shock wave with $M_s = 1.22$ in air interacting with a cylindrical bubble filled with helium. The shock wave is transmitted through the bubble and sets it into motion. The results presented focus only on the early stages of interaction and include a comparison with the experiments of Haas and Sturtevant and the computations of Quirk and Karni [105].

Both air and helium are assumed to be perfect gases with the properties listed in Table 5.5. As indicated by Haas and Sturtevant, the helium bubble is contaminated with air about 28% by mass [53]. The initial flow field is determined from the standard shock relations given the strength of the incident shock wave and considering the density and pressure of the quiescent flow ahead of the shock to be 1 kg/m^3 and 10^5 Pa . The bubble is assumed to be in thermodynamic and mechanical equilibrium with its surroundings. Therefore, its initial density is given by $\rho_{\text{He}} = \rho_{\text{Air}} R_{\text{Air}} / R_{\text{He}}$, where R_{Air} and R_{He} are the gas constants for air and helium, respectively.

The computational domain is shown in Figure 5.5. Only the upper half is actually computed because the flow is symmetric about the shock-tube axis. Quadrilateral grids with uniform resolutions of $h = \Delta x = \Delta y$ of $224 \cdot 10^{-6} \text{ m}$, $112 \cdot 10^{-6} \text{ m}$, and $56 \cdot 10^{-6} \text{ m}$,

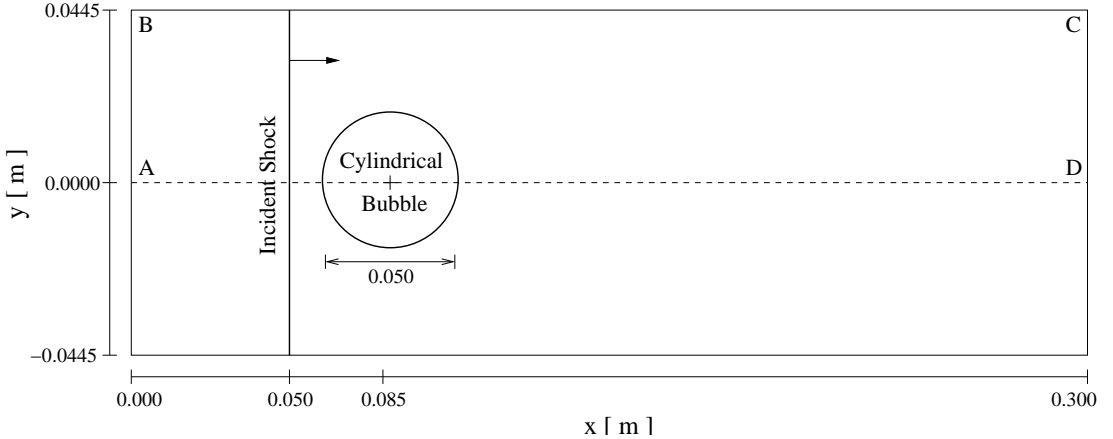


Figure 5.5: Schematic diagram of the computational domain (not drawn to scale).

m are employed. The smallest grid spacing is comparable to that used on the finest refinement level in the adaptive-grid computations of Quirk and Karni. (Of course, this is not to advocate using grids with uniform spacing for purposes other than focussed verification and validation studies.) Referring to Figure 5.5, solid-wall and symmetry conditions are applied to BC and AD, respectively. Along AB, inflow conditions are specified using the conditions behind the incident shock wave. An outflow condition is applied along CD. Figure 5.6 shows a sequence of numerically generated Schlieren images, illustrating the interaction of the shock wave with the bubble as computed on the finest grid. The computation reproduces all the features of the interaction, and is in good agreement with the experiments by Haas and Sturtevant and the simulations by Quirk and Karni.

Figure 5.6(a) shows the helium bubble at $t \approx 32 \mu\text{s}$, after it is hit by the incident shock wave. A curved refracted shock is generated inside the bubble. Since the helium has a higher speed of sound than the surrounding air, the refracted shock wave travels faster than the incident shock wave. Also, a weak expansion wave is reflected outside the bubble. The refracted shock wave eventually emerges from the bubble to become the transmitted wave, see Figure 5.6(b). The incident shock diffracts at approximately

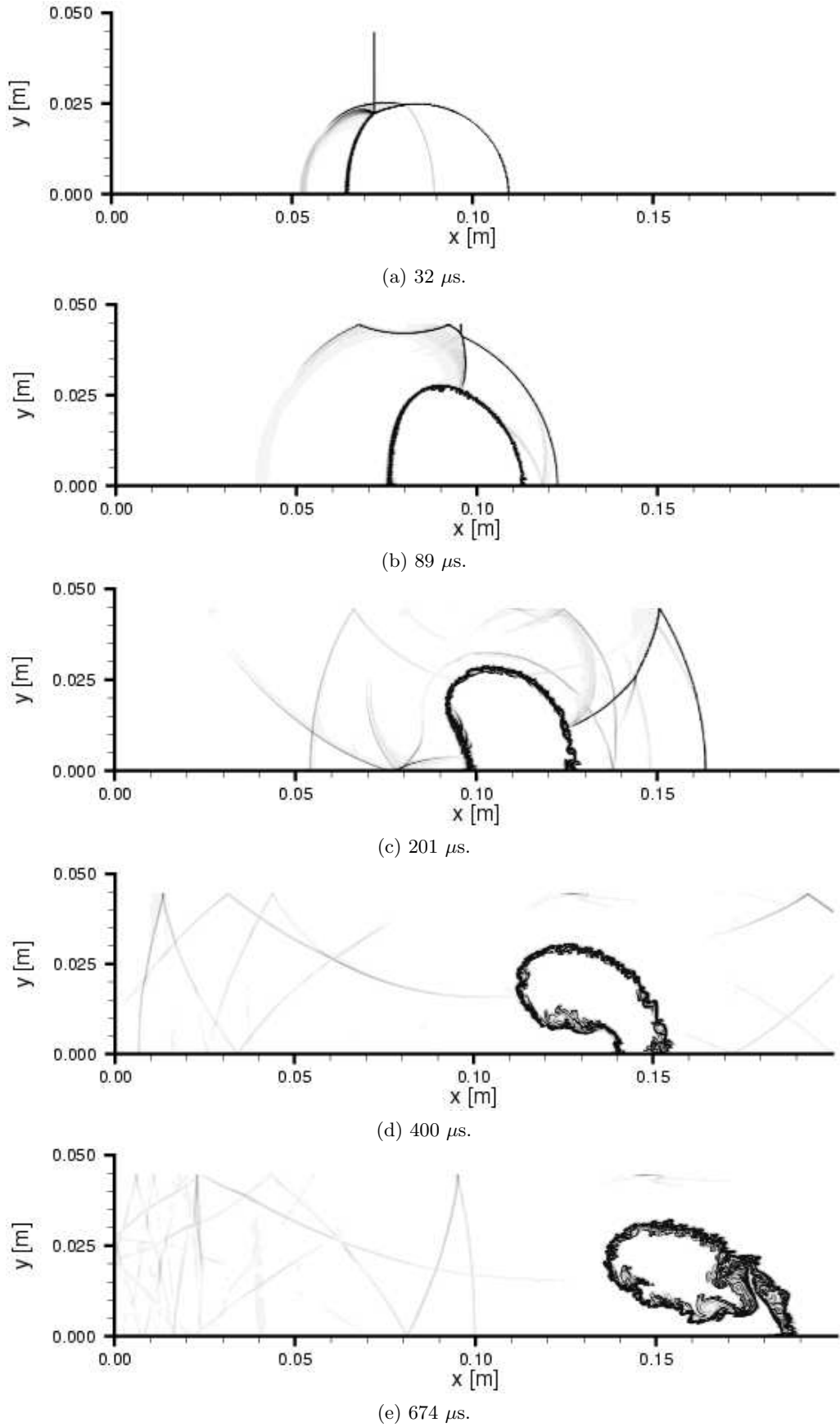


Figure 5.6: Numerically generated Schlieren images of the shock-bubble interaction computations on the fine grid at various times.

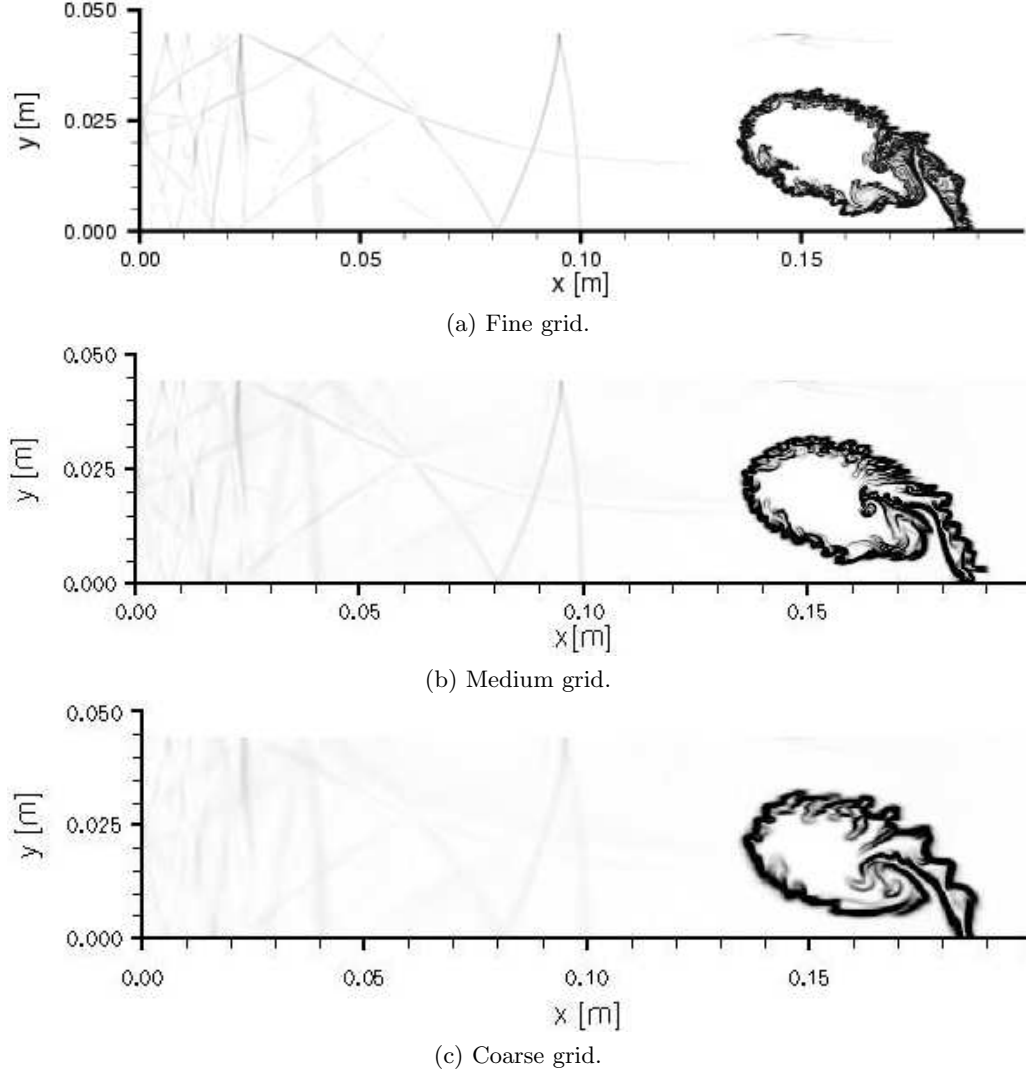


Figure 5.7: Numerically generated Schlieren images of the shock-bubble interaction computations at approximately $674 \mu\text{s}$ for different grid spacings.

$201 \mu\text{s}$ as shown in Figure 5.6(c). The bubble is deformed into a kidney shape and spreads laterally, see Figure 5.6(d). The deformation is caused by vorticity generated at the edge of the bubble due to the passage of the shock, which induces a jet of air along the axis of symmetry [105]. Figure 5.6(e) shows the formation of the bubble into a distinct vortical structure.

The accuracy of the numerical solutions are evaluated by conducting a convergence study. Figure 5.7 shows the comparison of the results on the coarse, medium,

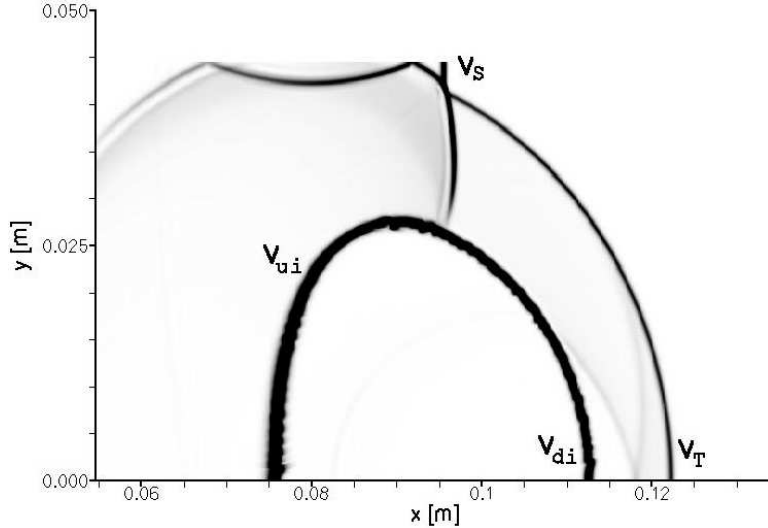


Figure 5.8: Definition of locations at which velocities are measured. V_S - incident shock, V_T - transmitted shock, V_{ui} - upstream edge of bubble, and V_{di} - downstream edge of bubble.

	V_S	E_{V_S}	V_T	E_{V_T}	V_{ui}	$E_{V_{ui}}$	V_{di}	$E_{V_{di}}$
Experiment [53]	410	—	393	—	170	—	145	—
Computation [105]	422	+3.0	377	-4.1	178	+4.7	146	+0.7
Coarse grid	426	+3.9	375	-4.6	172	+1.2	136	-6.2
Medium grid	426	+3.9	380	+3.3	168	-1.2	137	-5.5
Fine grid	423	+3.2	391	-0.5	169	-0.6	140	-3.4

Table 5.2: Comparison of computed velocities with those measured by Haas and Sturtevant [53] and computed by Quirk and Karni [105]. Percentage errors with respect to the measurements by Haas and Sturtevant are also shown. The notation is defined in Figure 5.8.

and fine grids at approximately $674\mu\text{s}$. The location of the bubble is approximately identical for the three grids. As expected, the vortical structures are more pronounced on the fine grid.

To validate the numerical solutions, the computed velocities of some prominent flow features as defined in Figure 5.8 are compared to the measurements of Haas and Sturtevant [53] the computations of Quirk and Karni[105]. The velocities are determined

from a linear least-squares curve fit of positions obtained from digitizing a sequence of numerically generated Schlieren images. Table 5.5 lists the velocities and the percentage errors of the computed results relative to the experimental values. The result are in good agreement with the measured values and thus demonstrate the accuracy of the approach.

Chapter 6

Multiphase and Multicomponent Free Surface Nozzle Jet Flow

This chapter illustrates the capabilities of the new developed analytical and computational approach for modeling and numerical simulation of multiphase and multicomponent flows to model high pressure and supersonic multiphase and multicomponent free surface nozzle jet flow. All numerical simulations performed in this Chapter are based on the governing Euler equations for the mixtures.

The results of the simulations including shock wave generation in the gaseous medium and cavitation in the nozzle injector are presented. The effects of cavitation to the jet flow rate and jet flow distribution are investigated. Furthermore, the effects of fluctuating inflow condition to the external jet formation are studied. In the simulation, the extended Roe and HLLC approximate Riemann solver for multiphase and multicomponent flow are used. First, the two schemes are tested to solve a high speed flow problems in an expanded duct. The purpose of this scenario is to test the capabilities of the scheme to handle problems with sudden expansion. This could help in choosing the appropriate scheme for simulating a supersonic multiphase and multicomponent free surface jet flow. Second, with the appropriate scheme, simulation of high pressure and supersonic multiphase and multicomponent free surface nozzle jet flow is conducted. A shock wave generation in a gaseous medium is captured. Third, cavitation model is introduced into the governing equation of multiphase and multicomponent flow. The purpose of the model is to capture cavitation in the nozzle orifice and to investigate its

effect on the jet flow rate. Finally, simulation of a supersonic multiphase and multi-component nozzle jet flow with a fluctuating inflow condition is performed in order to study the instability and formation of the external jet.

6.1 Shock Tube Analysis in an Expanded Duct

A shock tube analysis in an expanded duct is performed to test the capabilities of the two numerical schemes before simulation of free surface nozzle jet flow, which requires considerably larger resources. There are four scenarios studied. First, a high speed flow gas enters into an expanded duct that is filled with gas (gas into gas scenario). Second, a high speed flow liquid enters into an expanded duct that is filled with liquid (liquid into liquid scenario). Third, a high speed flow liquid enters into an expanded duct that is filled with gas (liquid into gas scenario). Finally, a high speed flow of liquid/gas enters into an expanded duct that is filled with gas (liquid/gas into gas scenario).

In all four scenarios, the two schemes (extended Roe and HLLC approximate Riemann solver) were able to solve the problems like capturing the traveling normal shock in the duct. However, when the shock reaches the region where there is an abrupt change (sudden expansion) of the cross sectional area of the flow, the extended Roe approximate Riemann solver failed, in particular to the third and fourth scenario. It was observed during the simulation that the extended Roe approximate Riemann solver had difficulty in dealing with large contact discontinuities and capturing the finite spread of the expansion fan as compared to the extended HLLC approximate Riemann solver.

The mathematical formulation for multiphase and multicomponent flow was successfully implemented in the incompressible single phase limit, compressible single phase limit and incompressible-compressible two-phase limit. For the compressible and incompressible single phase limit, like in the first scenario and second scenario, the two schemes (extended Roe and HLLC approximate Riemann solver) have no problem in

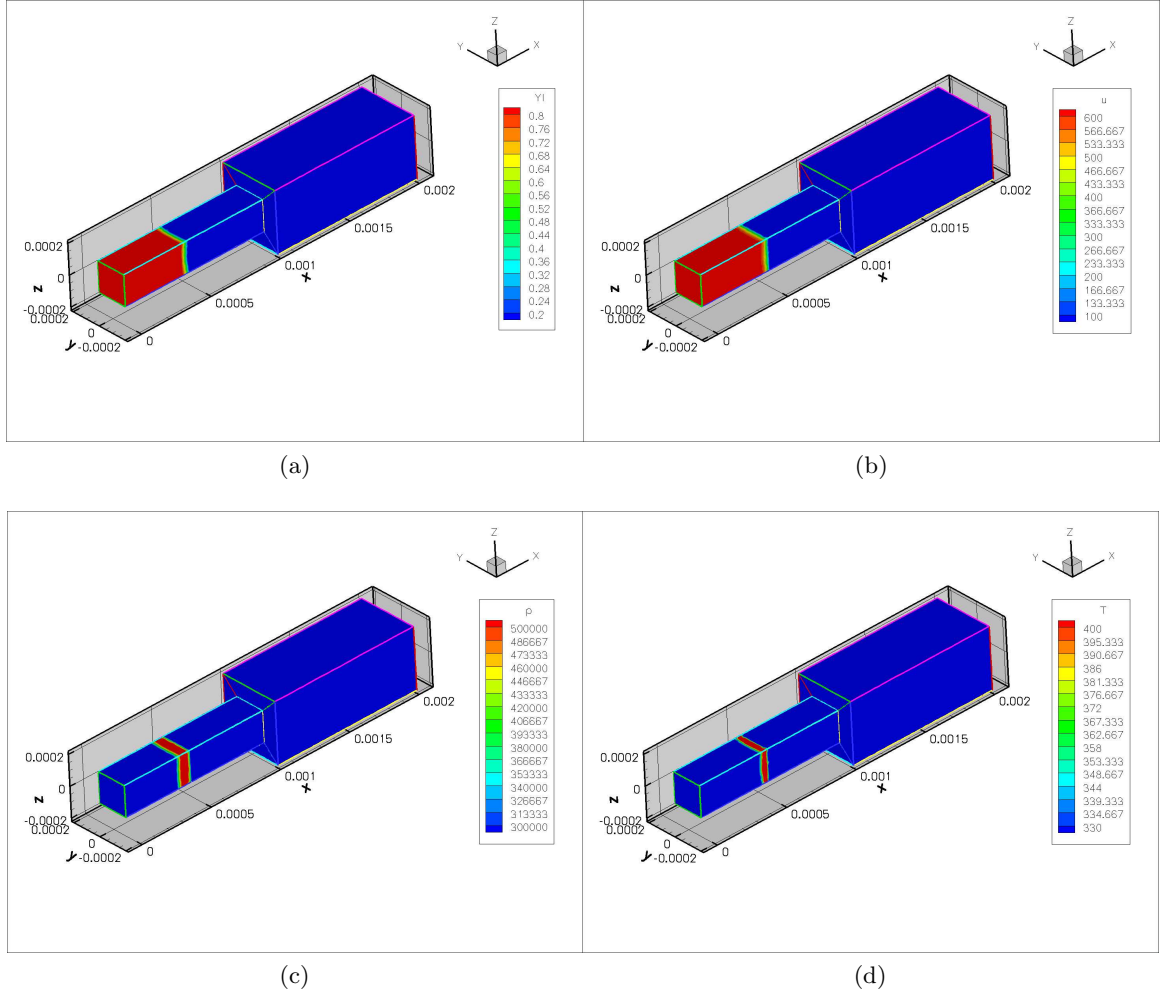


Figure 6.1: Plot of (a) mass fraction of liquid, (b) x-velocity component, (c) mixture pressure, and (d) mixture temperature, after 5.7689×10^{-7} seconds through an expanded duct, showing the normal traveling shock. Liquid density, $\rho_l = 100.0 \text{ kg/m}^3$; gas density, $\rho_g = 1.189 \text{ kg/m}^3$; inflow condition, inflow jet velocity is twice the speed of sound of the gas (Mach = 2.0 with respect to the gas).

dealing with sudden expansion of the cross sectional area of the flow. However, for the incompressible-compressible two-phase limit, like in the third and fourth scenario, the extended Roe approximate Riemann solver has encountered a problem just after the expansion of the duct. This is due to the large contact discontinuities in the density and velocity fields in both normal and tangential directions. Also, a sudden jump of the momentum occurs when the fluid exits just after the expansion of the duct. Unlike

the extended Roe solver, the extended HLLC solver has no problem in dealing with this region.

For an illustration, a selected third scenario (liquid into gas) is presented. In this case, the duct is initially filled with stationary gas of density $\rho_g = 1.189 \text{ kg/m}^3$. Then a liquid of density $\rho_l = 100 \text{ kg/m}^3$ enters the duct at supersonic condition (Mach=2.0) with respect to the gas. A total of 54,962 computational cells is used in the simulation. Figure 6.1 shows the plot of the mixture density, mass fraction of the liquid, mixture pressure and mixture x-velocity component, respectively. A normal traveling shock is captured and travels with an accurate velocity. At the contact, the pressure is high due to the momentum of the liquid that hits the stationary gas. The results are obtained after $t = 5.7689 \times 10^{-7}$ seconds, where at this time the liquid travels a distance of approximately 0.4 mm.

6.2 Multiphase/Multicomponent Free Surface Jet Flow

A simulation of a high pressure and supersonic multiphase and multicomponent free surface nozzle jet flow is performed. The purpose of this simulation is to support the experimental results of MacPhee *et al.* [89] and to provide more quantitative and qualitative information of the structure of the jet close to the nozzle region. The result of the latter experiment shows an oblique shock wave in a gaseous medium due to a high injection pressure and high speed flow of the jet.

In the simulation, a nozzle with an orifice diameter of $178 \mu\text{m}$ (the same diameter used by MacPhee *et al.* [89]) is connected to a chamber. Then a jet of fluid enters the nozzle and exits the nozzle orifice through a chamber generating an oblique shock wave. The intensity of the shock wave depends on the initial and inflow condition. The injection pressure ranges from 50 MPa to 135 Mpa. The chamber initial condition is at 1 atm. and 30°C . A total of 137,400 computational cells is used in the simulation.

There are four cases considered in the simulation to test the physical capabilities

of the multiphase and multicomponent mixture model. First, a jet of gas is injected into the chamber that is filled with gas (gas into gas case). Second, a jet of liquid is injected into the chamber that is filled with liquid (liquid into liquid case). Third, a jet of liquid is injected into the chamber that is filled with gas (liquid into gas case). Finally, a jet of liquid/gas is injected into the chamber that is filled with gas (liquid/gas into gas case).

The multiphase and multicomponent mixture model was successfully implemented in the incompressible single phase limit (liquid into liquid case), compressible single phase limit (gas into gas case) and incompressible-compressible two-phase limit (liquid into gas and liquid/gas into gas case) at subsonic and supersonic inflow conditions. In all four scenarios, the extended HLLC approximate Riemann solver is used since the extended Roe approximate Riemann solver has difficulty in handling problems where there is a sudden expansion of the cross sectional area of the flow. The extended HLLC solver is capable of solving multiphase and multicomponent flow problems with large density and flow field variations.

Results of the simulation for test case four (liquid/gas into gas) are shown in Figures 6.2 to 6.2. The inflow conditions are homogeneous mixture of 80% liquid, 10% gas and 10% vapor by volume, respectively. It is assumed in the simulation that the jet carries 10% of gas by volume due to gas entrapment and 10% of vapor by volume due to cavitation in the nozzle. The corresponding density of the liquid, gas and vapor are $\rho_l = 1000.0 \text{ kg/m}^3$, $\rho_g = 1.189 \text{ kg/m}^3$ and $\rho_v = 0.722 \text{ kg/m}^3$, respectively. The velocity of the jet at the inflow is assumed supersonic with a Mach number of 2 with respect to the gas inside the chamber. The results presented are at $t \approx 5\mu\text{s}$.

Figure 6.2 shows the contour plot of the mixture density and mass fraction of the liquid with the corresponding plot of the contact discontinuities across the interface in the centerline of the jet axis, respectively. An oblique shock wave in the gaseous medium is generated due to a high speed flow of the jet. The leading part of the jet looks like a tail of a “needle” and in this region the mass is highly concentrated. The

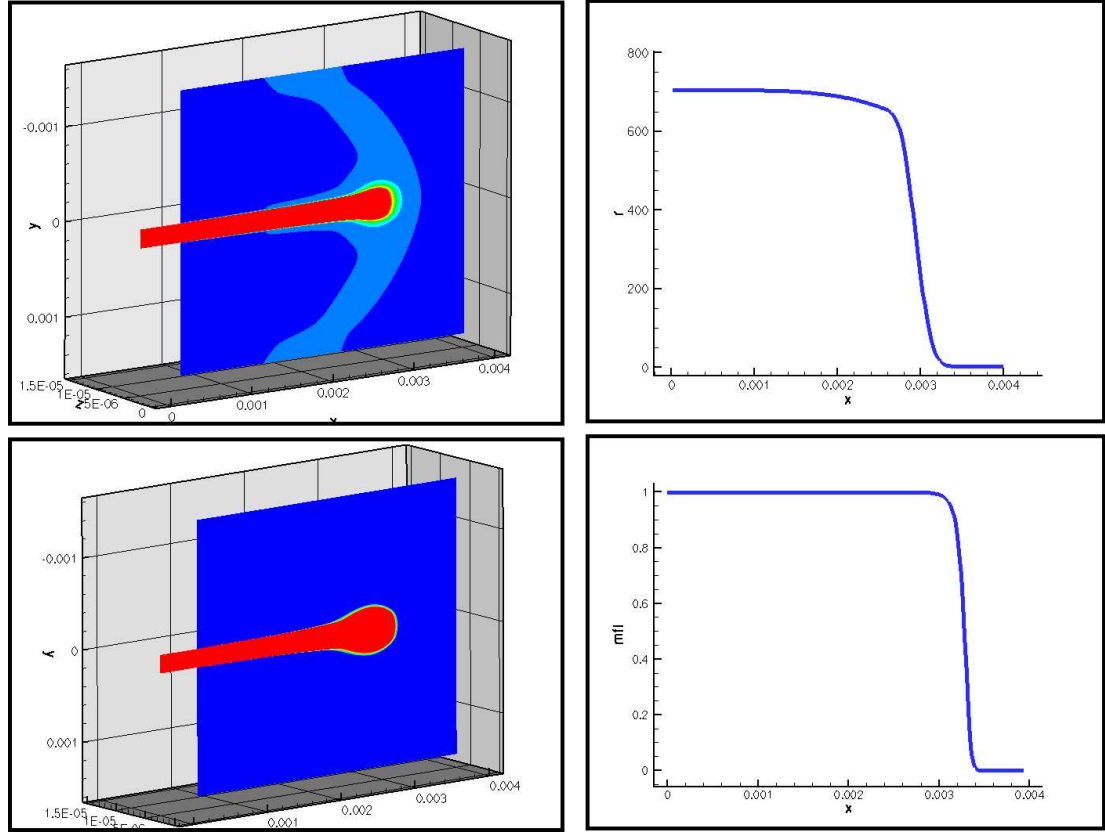


Figure 6.2: Plot of: (top left) mixture density showing an oblique shock wave in a gaseous medium, (top right) contact discontinuities of the mixture density across the interface in the centerline of the jet axis, (bottom left) mass fraction of the liquid, and (bottom right) contact discontinuities of the mass fraction of the liquid across the interface in the centerline of the jet axis. Liquid density, $\rho_l = 1000.0 \text{ kg/m}^3$; gas density, $\rho_g = 1.189 \text{ kg/m}^3$; vapor density, $\rho_v = 0.772 \text{ kg/m}^3$. Inflow condition, Mach = 2.0 with respect to the gas inside the chamber.

jet travels about 3.2 mm after $t \approx 5\mu\text{s}$.

The contour plot of the pressure and temperature of the mixture with the corresponding plot of the magnitude along the centerline of the jet axis is shown in Figure 6.2 respectively. A pressure and temperature wave is captured in the gaseous medium. At the leading edge of the jet, the pressure and temperature increases tremendously due to the strong impact and high momentum of the jet that hits the stationary gas.

The x-velocity component and the corresponding velocity profile across the lead-

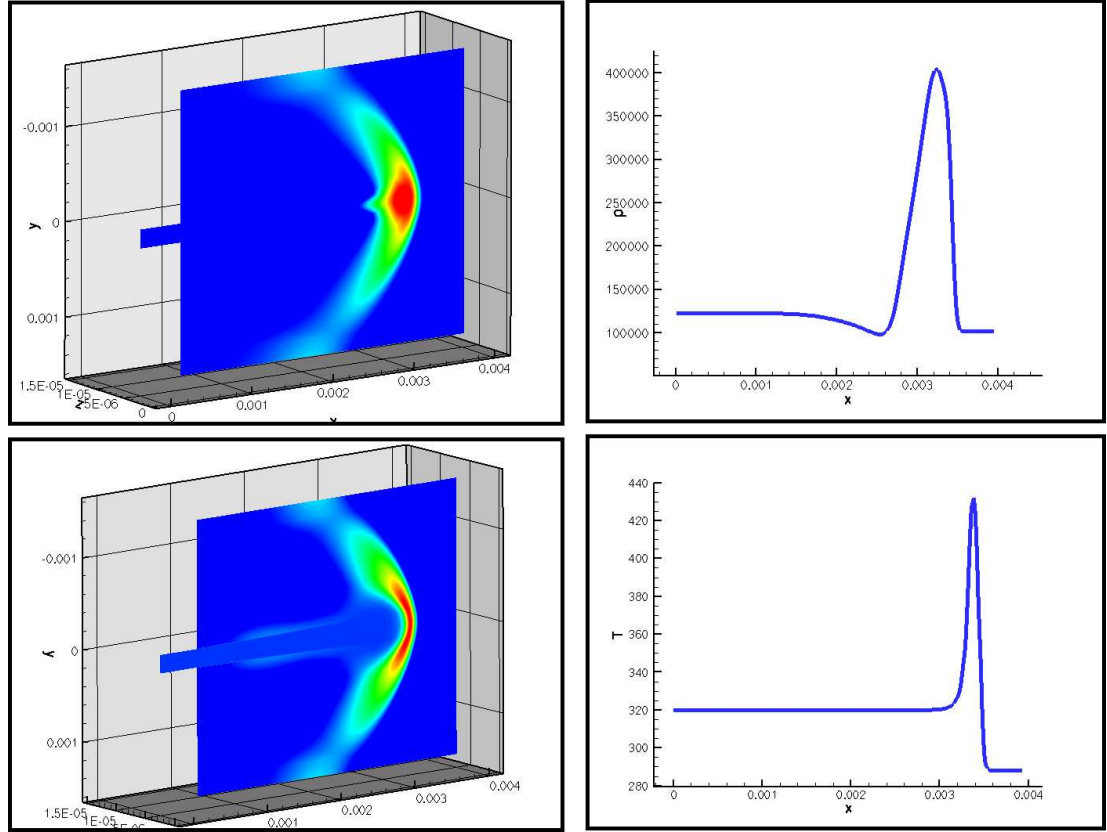


Figure 6.3: Plot of: (top left) mixture pressure showing an oblique shock wave in a gaseous medium, (top right) mixture pressure along the centerline of the jet axis, (bottom left) mixture temperature showing an oblique shock wave in a gaseous medium, and (bottom right) mixture temperature along the centerline of the jet axis. Liquid density, $\rho_l = 1000.0 \text{ kg/m}^3$; gas density, $\rho_g = 1.189 \text{ kg/m}^3$; vapor density, $\rho_v = 0.772 \text{ kg/m}^3$. Inflow condition, Mach = 2.0 with respect to the gas inside the chamber.

ing edge of the jet in the radial direction is plotted in Figure 6.2. The velocity of the jet expands in the radial direction as it travels further downstream with a decreasing magnitude. The jet entrained the near surrounding gas towards the direction of the flow, which results to a recirculation of the gas on the side of the jet near the exit of the nozzle region.

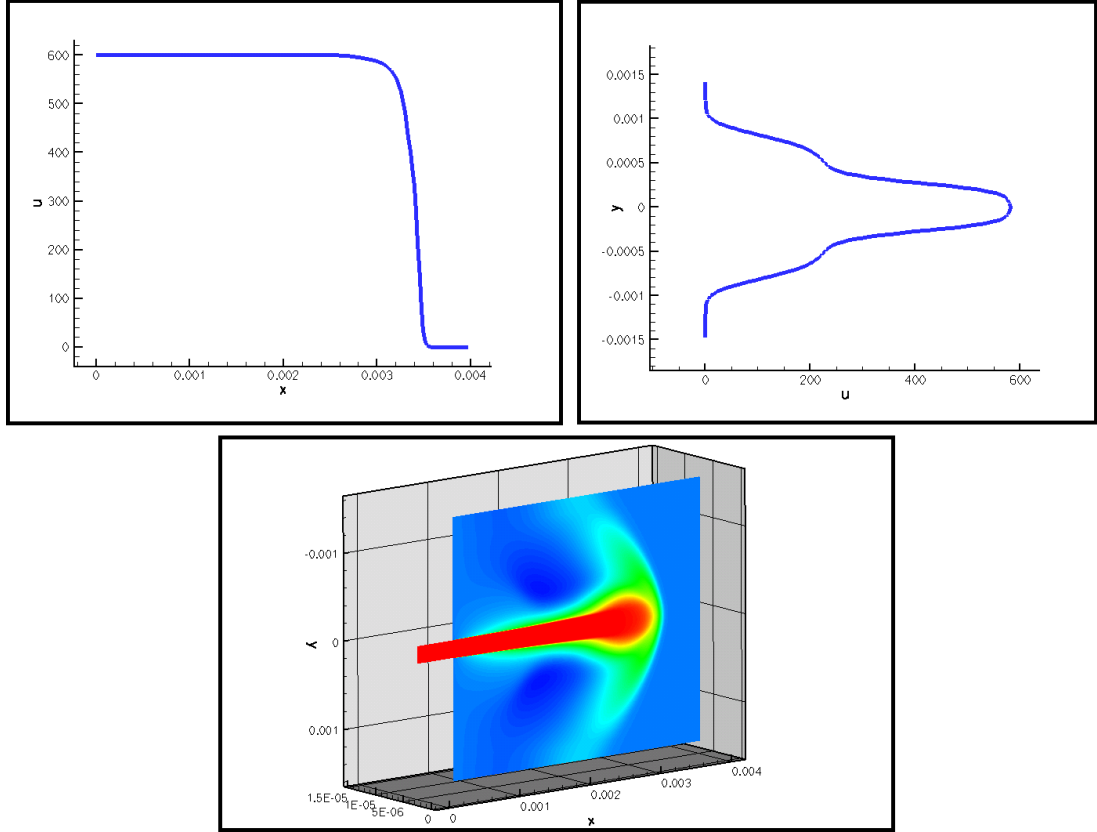


Figure 6.4: Plot of: (top left) contact discontinuities of the x-velocity component of the mixture across the interface in the centerline of the jet axis, (top right) velocity profile of the jet at 1.8 mm from the exit of the nozzle, and (bottom) mixture x-velocity component showing an oblique shock wave in a gaseous medium. Liquid density, $\rho_l = 1000.0 \text{ kg/m}^3$; gas density, $\rho_g = 1.189 \text{ kg/m}^3$; vapor density, $\rho_v = 0.772 \text{ kg/m}^3$. Inflow condition, Mach = 2.0 with respect to the gas inside the chamber.

6.2.1 Jet Formation and Jet Radial Profile

Figure 6.5 shows the jet formation. The leading part of the jet expands (slightly) radially and forms like a tail of a “needle”. A bulk of fluid immediately followed the leading edge of the jet, which is caused by the accumulation of the vapor and gas as the jet impacted on the ambient gas at the leading edge. Note that the jet is composed of a liquid, gas and vapor. The liquid at the leading edge of the jet moves at different rate than those of the average body of the jet. Without the resistance to the surrounding

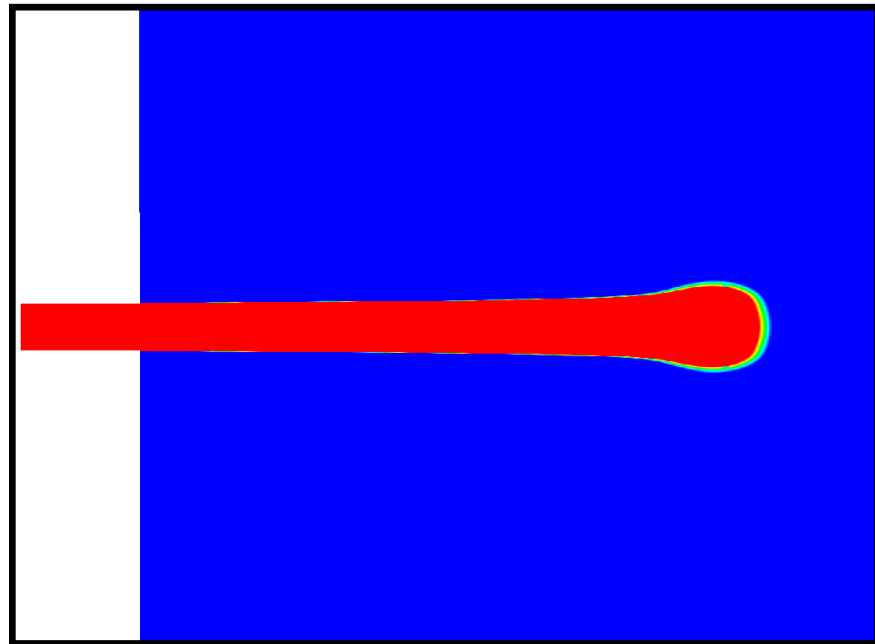


Figure 6.5: Plot of the mass fraction of the liquid. The leading edge of the jet is about 3.0 mm from the nozzle exit.

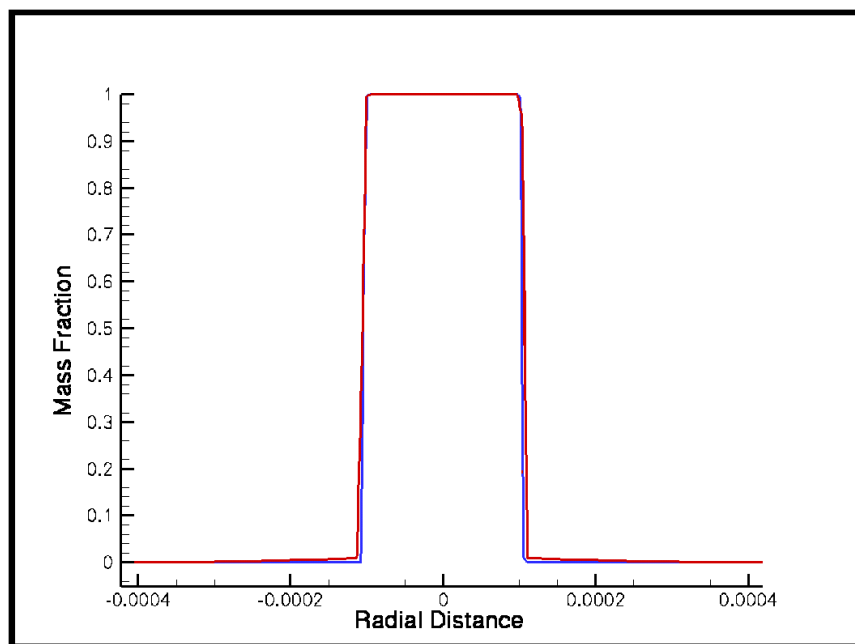


Figure 6.6: Jet radial profile across the body of the jet at a distant of about 3.0 mm from the nozzle exit.

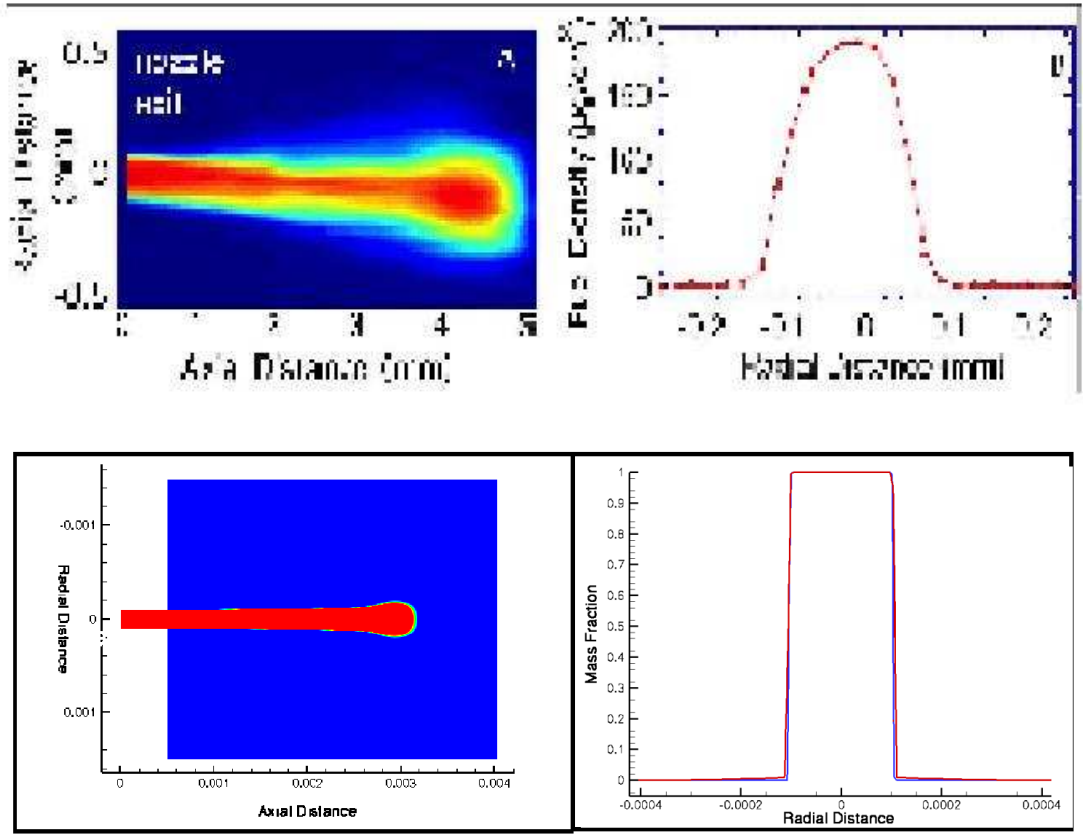


Figure 6.7: Comparison of the results between numerical simulation (bottom) and experimental observation of MacPhee *et al.* [89](top). (Left) Jet formation. (Right) Jet radial profile across the leading part of the jet.

gas, the jet body can move faster than the leading edge and with speeds close to the trailing edge. This phenomenon was observed by MacPhee *et al.* [89].

The jet radial profile across the body of the jet at a distant of 3.0 mm from the exit of the nozzle is shown in Figure 6.6. The results of the numerical simulation is in good agreement with the experimental results of MacPhee *et al.* [89]. A comparison of jet formation and jet radial profile between numerical simulation and experimental observation is shown in Figure 6.2.

6.3 Multiphase/Multicomponent Cavitating Nozzle Jet Flow

6.3.1 Cavitation Overview

Cavitation is a serious physical hydrodynamic phenomenon, which is common problem to many fluid related devices such as in pumps, turbines, control valves and nozzles. It can cause serious wear and tear and possibly damages the devices. This happens when the vapor collapses after evaporation due to the decreased in the flow velocity and to the increased in pressure. Cavitation may occur when the local static pressure in a fluid drops below the saturation vapor pressure of the liquid at the actual temperature for sufficient duration of time by static or dynamic means. Cavitation is a dynamic phenomena since it is concerned with the growth and collapse of cavities. There are two stages of the cavitation process as described in [75]. The first stage is called “incipient stage”, where cavitation is just barely detectable. Here, the discernible bubbles of incipient cavitation is small and a limited zone of cavitation. The second stage is called “developed stage”, where evaporation rates increased and cavitation grows due to the changes in conditions such as pressure, velocity and temperature. The occurrence of the inception and development of cavitation depend on the condition of the liquid, including the presence of contaminations, either solid or gaseous, and on the pressure field in the cavitation zone. A good reference for a general study of cavitation can be found in [75].

6.3.1.1 Types of Cavitation

1. Traveling Cavitation

It is composed of individual transient cavities or bubbles, which form in the liquid and move with the liquid as they expand, shrink, and then collapse. These traveling transient bubbles may occur at the low pressure region along a solid boundary or in the liquid interior either at the cores of the moving vortices

or in the high turbulence region in a turbulent shear field.

2. Fixed Cavitation

A cavitation that develops after inception, in which the liquid flow detaches from the rigid boundary of an immersed body or a flow passage to form a pocket or cavity attached to the boundary.

3. Vortex Cavitation

The cavities are found in the cores of vortices that form in high shear zone. Here, the cavitation may appear as traveling or fixed cavities. This is one of the earliest observed cavitation types, since it often occurs on the tip of the blade's propeller. This may also occur on the boundary surfaces of a submerged jets where there is sufficiently high shear rate. The life of vortex cavity is longer than the traveling cavity due to the angular momentum of the liquid.

4. Vibratory Cavitation

Cavitation occurs and collapse due to a continuous series of high-amplitude, high-frequency pressure pulsations in the liquid. These pressure pulsations are generated by a submerged surface that vibrates normal to its face and sets up pressure waves in the liquid.

6.3.1.2 Effects of Cavitation

Knapps *et al.* [75] classified the effects of cavitation into three general categories. First, cavitation can modify the hydrodynamics of the flow of the fluid. The flow pattern can be modified and the dynamic interaction between the liquid and its boundaries can be altered as the cavity volume displaces the liquid. The effect of cavitation tends to limit or lessen the force that can be applied to the liquid by the surface. Second, cavitation can cause damage on the solid-boundary surface of the flow. It can cause wear and tear of the surface of any solid boundaries including metals either, hard or

soft, brittle or ductile, chemically active or chemically inert. However, nonmetallic solid boundaries like rubber, plastic, glass, quarts and concrete are susceptible to cavitation damage. Third, cavitation can induced noise and vibration when bubbles or cavities collapse.

6.3.1.3 Experimental Studies of Cavitation

The main difficulties of understanding the physical nature of cavitation is due to the fact that cavitation is a high-speed phenomenon. This high-speed phenomenon limits to investigate the process of inception, growth and collapse in both flowing and non-flowing environments. The main problems of cavitation are (1) how to provide a suitable means for producing a controlled cavitation, (2) how to detect and locate the cavitation and (3) how to “arrest” the motion. Knapps *et al.* [75] presented and discussed some special equipment that is developed to produced cavitation under controlled conditions in a specified locations, where observations can be made.

Knapps *et al.* [75] categorized and explained several methods for detecting the presence of cavitation, either direct or indirect observation. For indirect observations, cavitation can be detected (1) by determining the effect of cavitation on the performance of a piece of equipment, (2) by measuring the effect of cavitation on the distribution of pressure over the boundary at which cavitation occurs, (3) by sensing the noise emitted by cavitation and (4) by allowing cavitation to scatter laser-beam light into a photocell [39]. For direct observations, cavitation can be detected by visual and photographic means. This photographic technique has the possibility for detailed study of the hydrodynamic phenomenon either at inception or for advanced stages of cavity development.

The study of cavitation grew rapidly when it was realized that cavitation effect can cause a tremendous damage to many fluid related devices. Since then, there have been many methods developed to detect and locate cavitation. Richards *et al.* [111]

conducted a cavitation experiment using a water shock tube. They used a pressure transducer to monitors the pressure changes and used schlieren photography techniques to study cavitation bubbles. Escaler *et al.* [41] conducted an experimental investigation to evaluate the detection of cavitation in actual hydraulic turbines. Their methodology is based on the analysis of structural vibrations, acoustic emissions and hydrodynamic pressures measured in the machine. A flow visualization of cavitation with particle and bubble using the Particle Image Velocimetry (PIV) image processing method is performed by Kato *et al.* [73]. Another experiment that uses an ultra high speed video camera with the maximum frame speed of 10^6 fps to observe the detailed aspects of three cavitation patterns such as separated vortex cavitation in a convergent-divergent channel, Karman-vortex like cavitation in the wake flow of a circular cylinder and vibratory cavitation in an ultrasonic vibratory apparatus is conducted by Sato *et al.* [119].

6.3.2 Cavitation Modeling and Simulation

Most of the experimental methods in detecting and locating cavitation are in macroscopic scale and are limited to give detailed picture of the hydrodynamic phenomenon. To perform a cavitation study by experimental method, it requires some costly equipments or devices. However, with the advent of the computer and development of the numerical technique, a numerical study of cavitation became the best alternative to supplement the experimental results.

The new developed general framework for simulation of multiphase and multicomponent flow is capable of incorporating a variety of cavitation models. To demonstrate this, a cavitation model by Hosangadi *et al.* [64] is considered. The cavitation source term is given by

$$S_v = K_l \rho_l \phi_l + K_v \rho_v \phi_v \quad (6.1)$$

where K_l and K_v are defined as

$$K_v = \begin{bmatrix} 0 & P < P_v \\ \frac{1}{\tau_v} \left(\frac{Q_\infty}{L_\infty} \right) \left[\frac{P - P_v}{\frac{1}{2} \rho_\infty Q_\infty^2} \right] & P > P_v \end{bmatrix}, \quad (6.2)$$

$$K_l = \begin{bmatrix} 0 & P > P_v \\ \frac{1}{\tau_f} \left(\frac{Q_\infty}{L_\infty} \right) \left[\frac{P - P_v}{\frac{1}{2} \rho_\infty Q_\infty^2} \right] & P < P_v \end{bmatrix}. \quad (6.3)$$

and τ_f and τ_v are the rate for vapor formation and liquid reconversion, respectively, and can be obtained experimentally. The cavitation number is given by:

$$C = \left[\frac{P - P_v}{\frac{1}{2} \rho_\infty Q_\infty^2} \right]. \quad (6.4)$$

where, P_v is the saturation pressure of the vapor at a given temperature.

Some results of unsteady cavitation in a nozzle is shown in Figure 6.3.2 to Figure 6.3.2. Cavitation starts to develop at the entrance of the nozzle orifice as shown in Figure 6.3.2. This is an example of an “incipient stage” as described by Knapps *et al.* [75]. This is followed by a “developed stage”, where evaporation rates increased and cavitation grows due to the changes in conditions of pressure, velocity and temperature, see Figs. 6.3.2 to 6.3.2. In Figs. 6.3.2 to 6.3.2, the cavities or bubbles move with the liquid as they expand, shrink, and then collapse. This type of cavitation is called traveling cavitation. Another type of cavitation that can be observed in this process is the fixed cavitation, see Figs. 6.3.2 and 6.3.2, where a fixed cavity or bubble is attached to the wall of the nozzle orifice. This can cause the fluid flow to detaches from the wall of the nozzle orifice. Furthermore, Figure 6.3.2 shows the contour plot of the pressure. A pressure drop in the nozzle orifice can be observed. Due to a sudden change of the cross sectional area of the flow, the fluid flow accelerates in this region that can cause a pressure drop, which can be below the saturation pressure of the vapor.

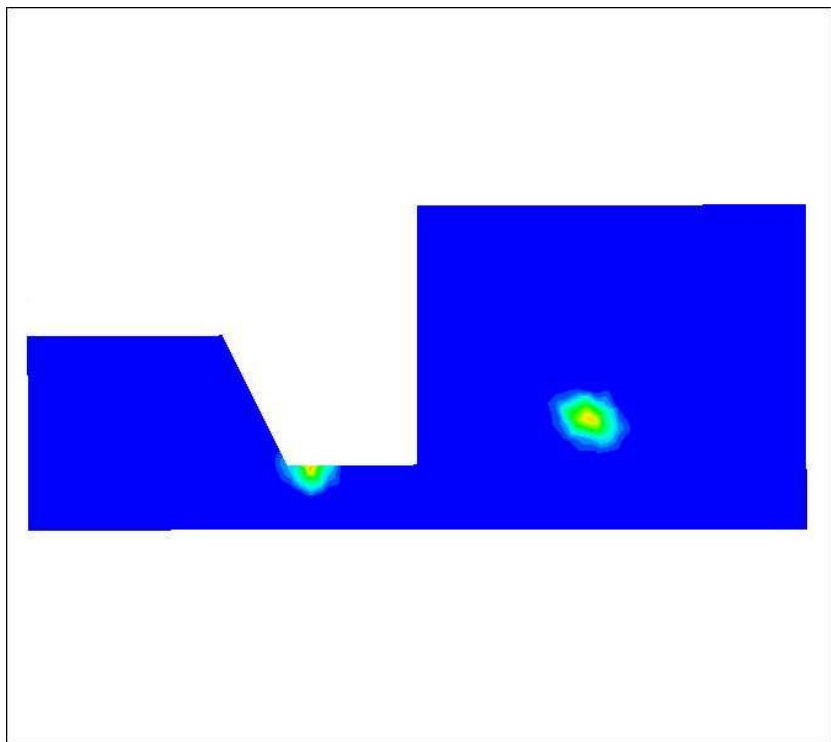


Figure 6.8: Plot of the mass fraction of the vapor after $2.000\text{e-}04$ sec. Inflow condition: $P = 1,161,000 \text{ Pa}$; $u = 10 \frac{\text{m}}{\text{s}^2}$; domain length = 6 mm; orifice over nozzle entrance ratio: $\frac{a_t}{a_i} = 0.3$; mesh size = 8,366.

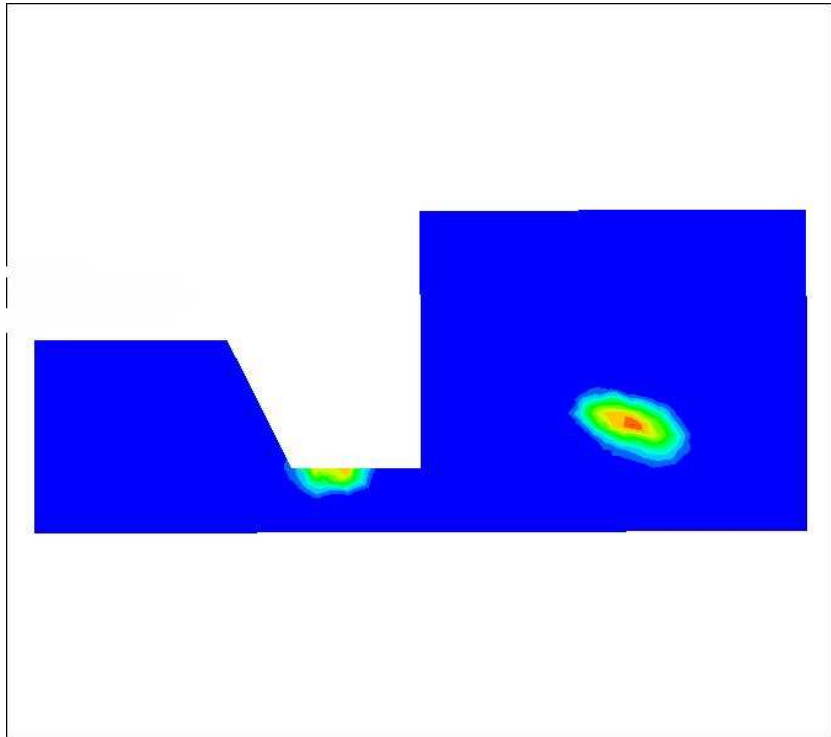


Figure 6.9: Plot of the mass fraction of the vapor after $2.202\text{e-}04$ sec. Inflow condition: $P = 1,161,000 \text{ Pa}$; $u = 10 \frac{\text{m}}{\text{s}^2}$; domain length = 6 mm; orifice over nozzle entrance ratio: $\frac{a_t}{a_i} = 0.3$; mesh size = 8,366.

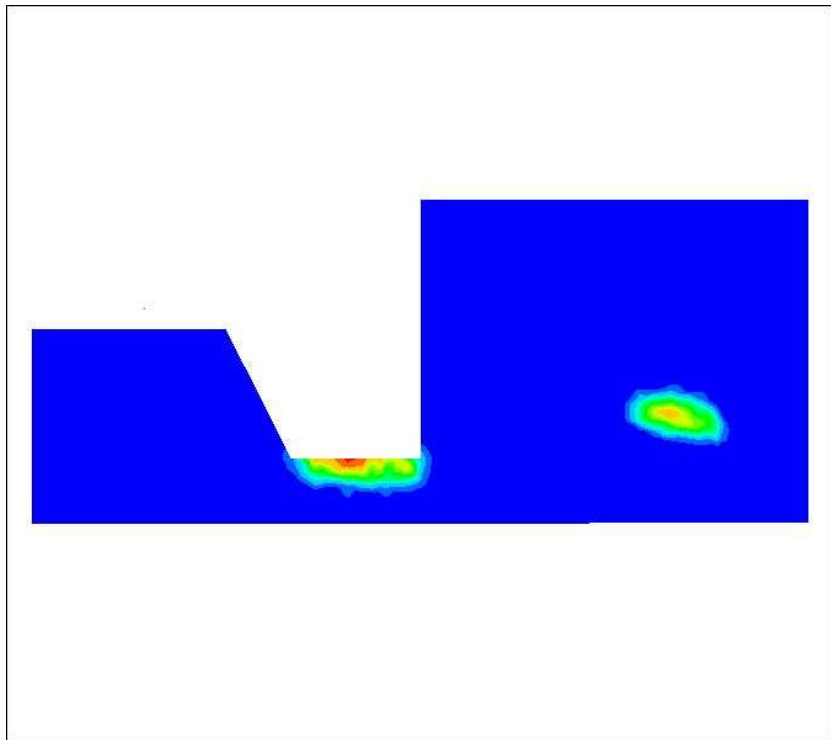


Figure 6.10: Plot of the mass fraction of vapor after $2.502\text{e-}04$ sec. Inflow condition: $P = 1,161,000 \text{ Pa}$; $u = 10 \frac{\text{m}}{\text{s}^2}$; domain length = 6 mm; orifice over nozzle entrance ratio: $\frac{a_t}{a_i} = 0.3$; mesh size = 8,366.

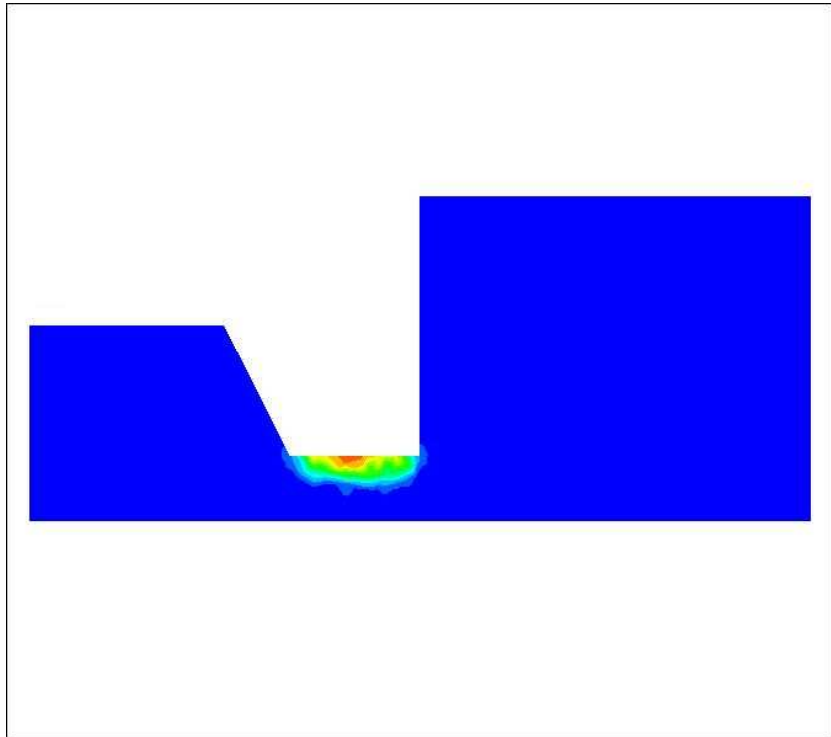
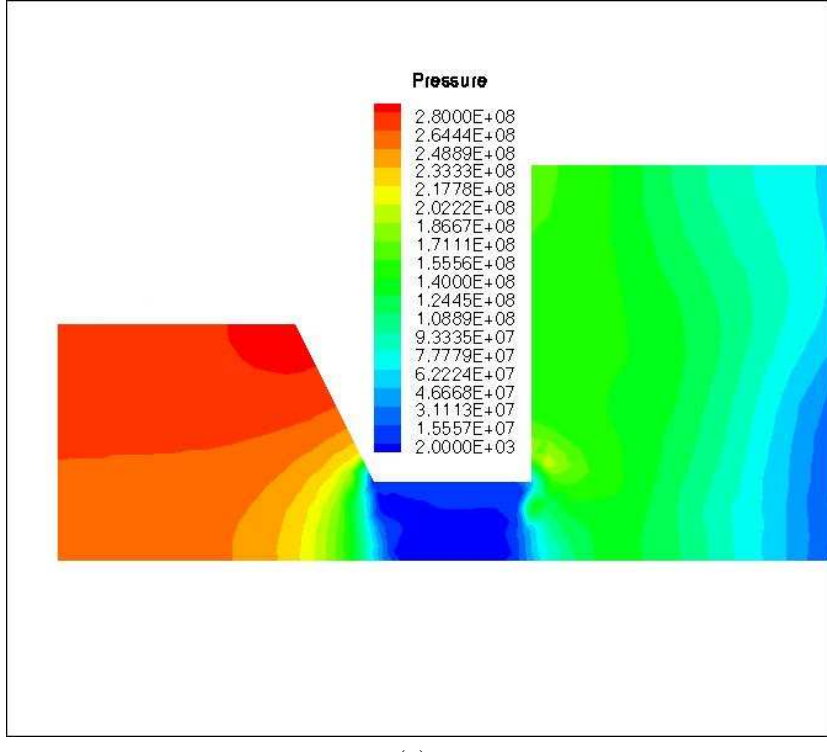


Figure 6.11: Plot of the mass fraction of vapor after $3.000\text{e-}04$ sec. Inflow condition: $P = 1,161,000 \text{ Pa}$; $u = 10 \frac{\text{m}}{\text{s}^2}$; domain length = 6 mm; orifice over nozzle entrance ratio: $\frac{a_t}{a_i} = 0.3$; mesh size = 8,366.



(a) .

Figure 6.12: Plot of the pressure after 3.000e-04 sec. Inflow condition: $P = 1,161,000$ Pa; $u = 10 \frac{m}{s^2}$; domain length = 6 mm; orifice over nozzle entrance ratio: $\frac{a_t}{a_i} = 0.3$; mesh size = 8,366.

6.3.3 Cavitation in Nozzle Injector

Cavitation will normally occur inside the nozzle injector in many modern fuel injection systems primarily due to high injection pressure. Other important parameters that additionally affect cavitation are the orifice inlet curvature, injection angle, and nozzle aspect ratio. A numerical simulation is carried out for a high injection pressure to confirm cavitation inside a nozzle injector. The two-dimensional plane experimental test case of Roosen *et al.* [114] is used in the simulation. The same test case used by Yuan *et al.* [155] to validate their numerical simulation. The dimension of the nozzle hole is 1 mm \times 0.28 mm \times 0.2 mm (length \times height \times width). Figure 6.13 shows the computational domain of the nozzle injector and the treatment of the boundary conditions. To reduce the computational time, a symmetric boundary condition is imposed along the nozzle

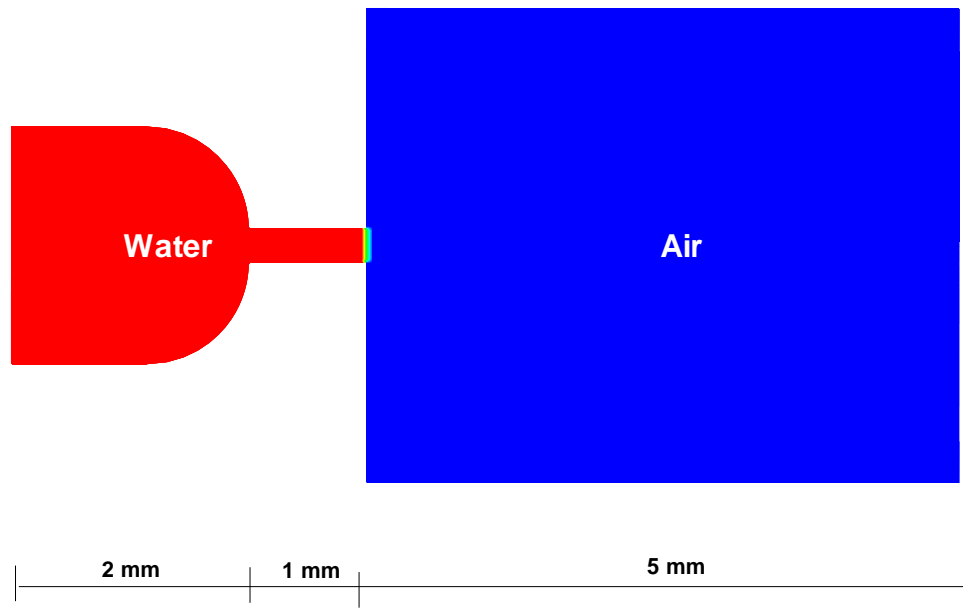


Figure 6.13: Plot of the initial condition of the system. The nozzle region is filled with liquid and the chamber downstream from the exit of the nozzle is filled with gas.

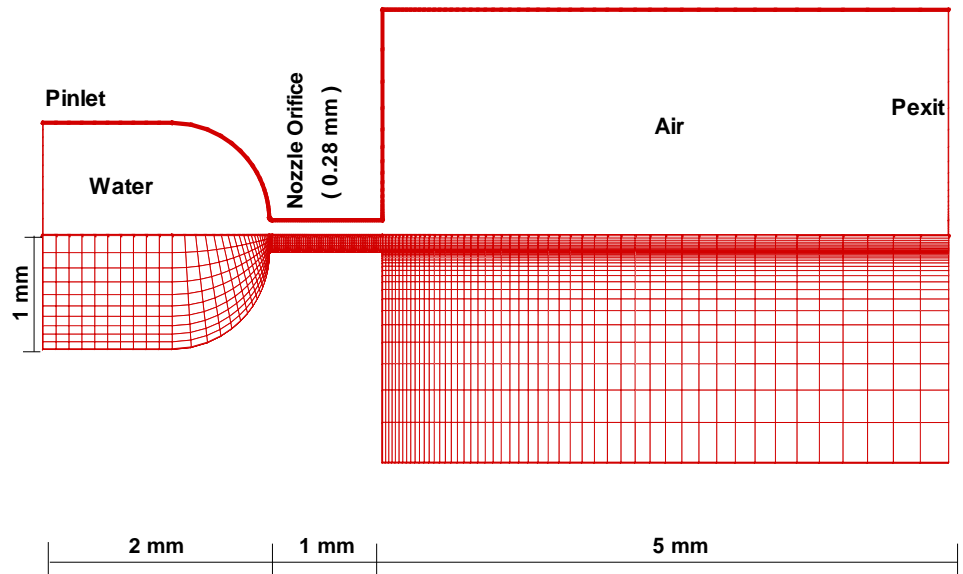


Figure 6.14: Plot of the computational mesh and boundary conditions of the two-dimensional plane model nozzle injector.

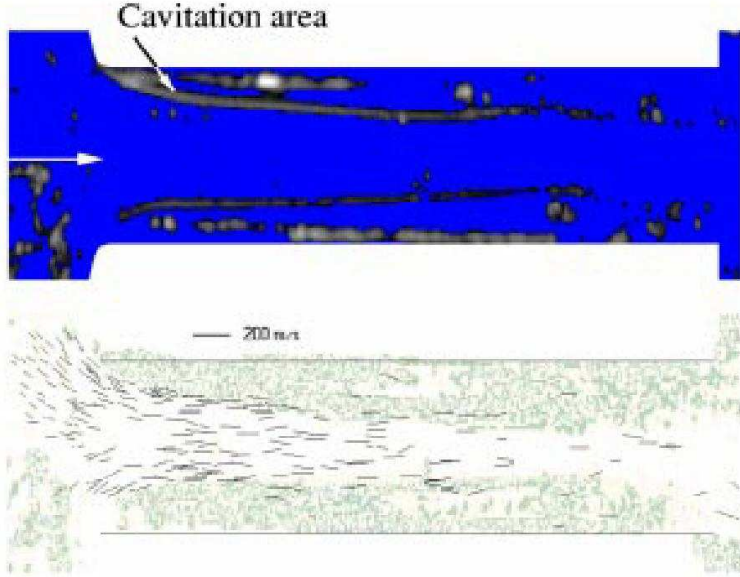


Figure 6.15: Cavitation inside the nozzle injector. Experimental results taken from Roosen *et al.* [114]. Injection pressure, $P_{inlet} = 80$ bar; exit pressure, $P_{exit} = 11$ bar.

axial axis, and solves only the lower half of the computational domain. A total of 7140 computational cells are used in the numerical computation. The system is initialized with liquid in the nozzle region and gas in the exit region. Figure 6.14 shows the initial condition of the system. Note the sharp interface between the liquid and gas just after the nozzle exit.

There are two scenarios performed in the simulation to compare with the experimental results of Roosen *et al.* [114], and the numerical simulation results of Yuan *et al.* [155]. The first scenario considers an injection pressure of 80 bar and an ambient condition of 21 bar, while the second scenario considers an injection pressure of 80 bar and an ambient condition of 11 bar. The injection pressure is assigned a value of the inlet pressure for simplicity and is assumed to be a constant steady inlet pressure throughout the calculation. In the next section, the injection pressure is fluctuated and the effect to the external jet formation is observed.

In both scenarios, the results of the simulation, see Figure 6.17, were in substantial

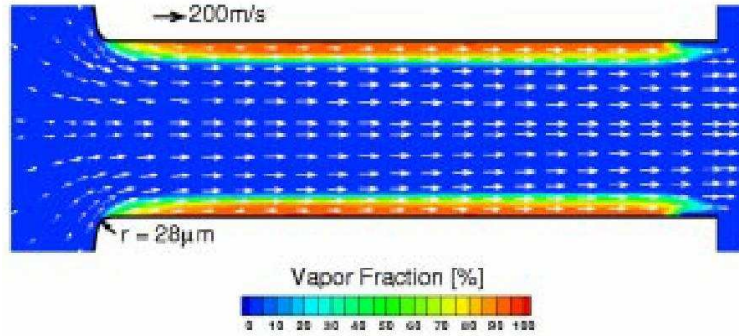


Figure 6.16: Cavitation inside the nozzle injector. Numerical simulation by Yuan *et al.* [155]. Injection pressure, $P_{inlet} = 80$ bar; exit pressure, $P_{exit} = 11$ bar.

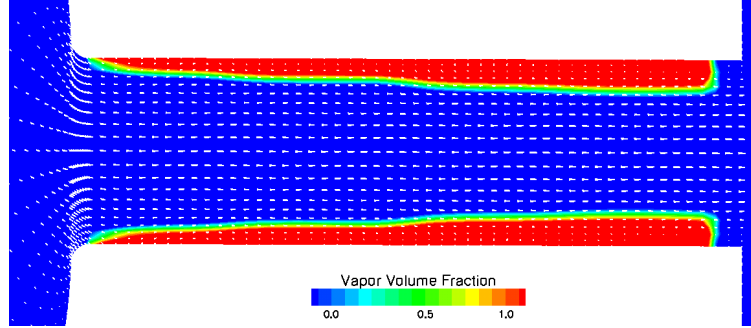


Figure 6.17: Results of the numerical simulation for a cavitating nozzle injector using the multiphase mixture formulation with a cavitation model. Injection pressure, $P_{inlet} = 80$ bar; exit pressure, $P_{exit} = 11$ bar.

agreement with the experimental results of Roosen *et al.* [114], see Figure 6.15, and the numerical simulation results of Yuan *et al.* [155], see Figure 6.16, respectively. Figure 6.18 shows the contour plot of the vapor and gas volume fraction, inside and close to the exit of the nozzle injector at different time levels. It was observed that the time scale of the internal cavitation dynamics is on the order of $10 \mu s$, which confirms the assertion of Yuan *et al.* [155]. It was also noticed that the bubble cavities start to develop near the inlet corner of the nozzle orifice, and extend further downstream to the exit of the nozzle. The maximum length of cavity is observed after steady flow is achieved. Maximum length of cavity is reached after 5×10^{-5} seconds. As can be seen

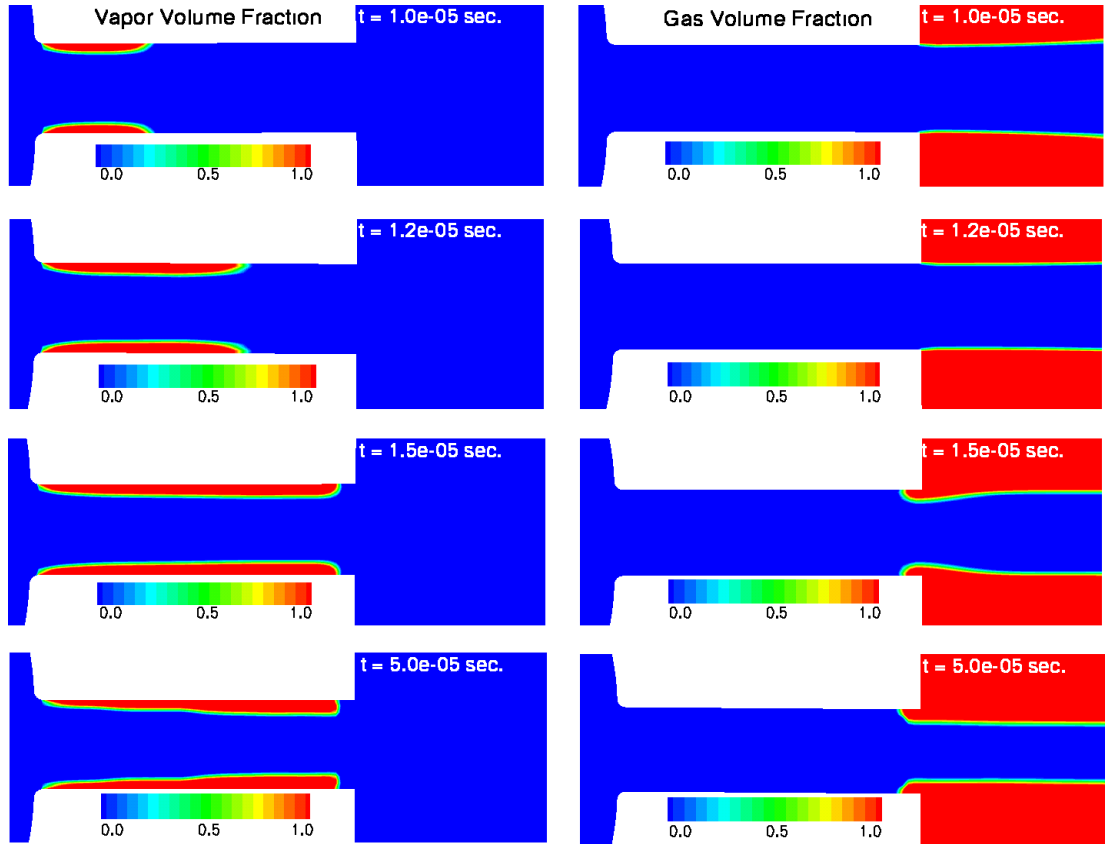


Figure 6.18: Contour plot of the vapor (left) and gas (right) volume fraction inside and close to the exit of the nozzle injector. Constant steady injection pressure, $P_{inlet} = 80$ bar; exit pressure, $P_{exit} = 11$ bar.

in Figure 6.18, for the gas volume fraction, a presence of gas inside and near the exit of the nozzle is observed. This could be a re-entrant jet of gas that starts to penetrate the cavity and causes it to collapse. However, the re-entrant jet is not strong enough to penetrate inside the nozzle further upstream. This might be due to the steadiness of the flow and constant steady injection pressure.

Figure 6.19 shows the contour plot of the liquid volume fraction and velocity, inside and close to the exit of the nozzle injector at different time levels. It is clear that cavitation causes a reduction of the cross sectional area of the liquid jet flow as can be seen on the left of Figure 6.19. This means that cavitation chokes the flow of liquid and

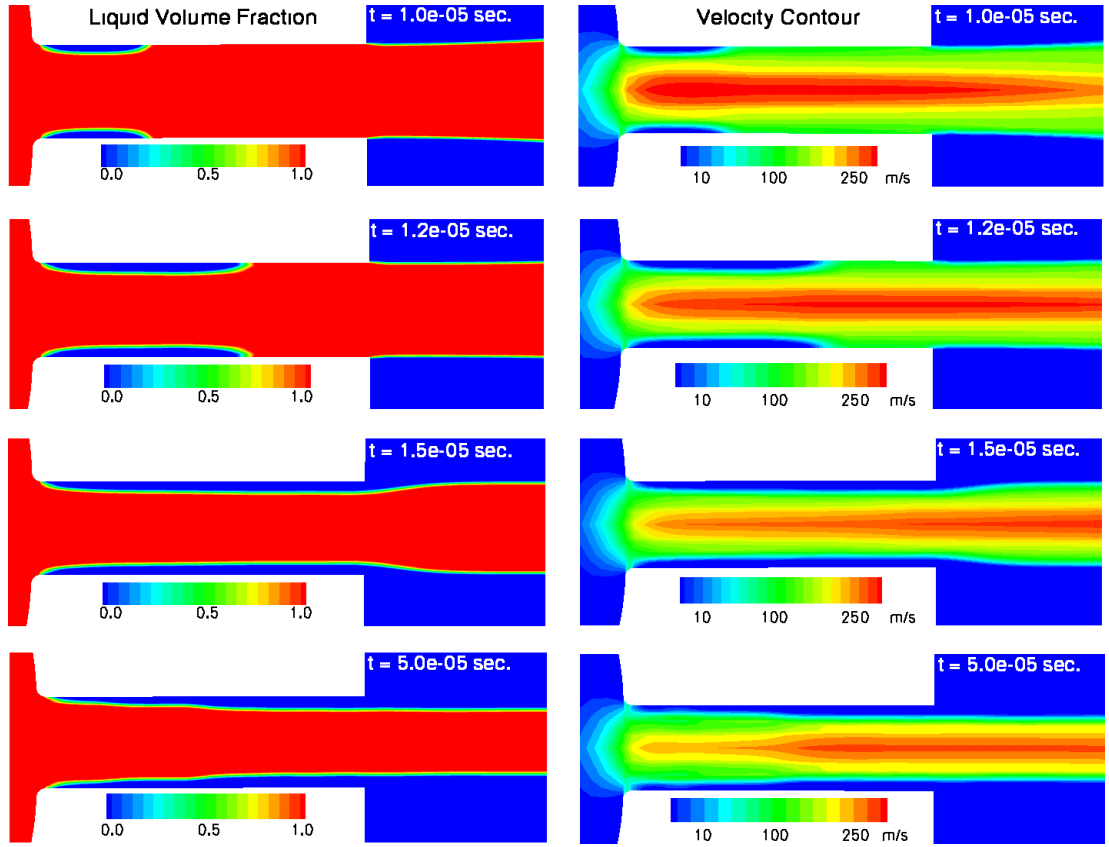


Figure 6.19: Contour plot of the liquid volume fraction (left) and velocity profile (right) inside and close to the exit of the nozzle injector. Constant steady injection pressure, $P_{inlet} = 80 \text{ bar}$; exit pressure, $P_{exit} = 11 \text{ bar}$.

reduces the discharge significantly. The coefficient of discharge within the orifice for a 1.2 cavitation number was computed to be equal to a value of 0.75, which is about 7 % higher as compared to Nurick's [99] correlation and Singhal *et al.* [126] simulation. Also, shown to the right of Figure 6.19 is how cavitation separates the flow inside the nozzle injector and affects the velocity profile of the jet flow.

6.4 The Effect of Fluctuating Inflow Condition to the External Jet Formation

It has been illustrated in the previous section that cavitation occurs inside the nozzle injector and has significant effect on the liquid flow discharge and velocity profile of the flow. In the actual injection process, the injection pressure and exit pressure fluctuate at high frequencies. To understand the effect of injection pressure fluctuation to the cavitation process and the external jet formation, a periodic rectangular inflow pressure condition is implemented. Figure 6.20 shows the results of the simulation at different time levels for a fluctuating inflow pressure condition. The volume fraction of liquid that relates to the amount of liquid discharge and the formation of the external jet is shown on the left of Figure 6.20, while the volume fraction of vapor inside and close to the exit of the nozzle injector is depicted on the right of Figure 6.20.

The cavitation process in the actual injection system becomes more complex due to fluctuating inflow boundary condition. There is significant interaction of the bubble cavities and gas from the nozzle exit. It can be seen on the right of Figure 6.20 that the cavitation process is more complicated. A re-entrant jet of gases from the downstream chamber causes the cavities to collapse and separate. The separation of the bubble cavities creates a bubble cloud downstream of the cavity. The bubble clouds will interact with a large rotating vortex of gas external to the nozzle as it exits from the nozzle injector. Qin *et al.* [104] further postulated that the external pressure propagates into the orifice once the re-entrant jet reaches the nozzle orifice inlet and occupies the entire upper part of the orifice, causing the flow in the nozzle to revert to a non-cavitating mode. This phenomenon is called hydraulic flip, which was observed by Bergwerk *et al.* [16].

The discharge of the nozzle is strongly dependent on the cavitation process and the magnitude of the bubble cavities. As can be seen on the left of Figure 6.20 , the

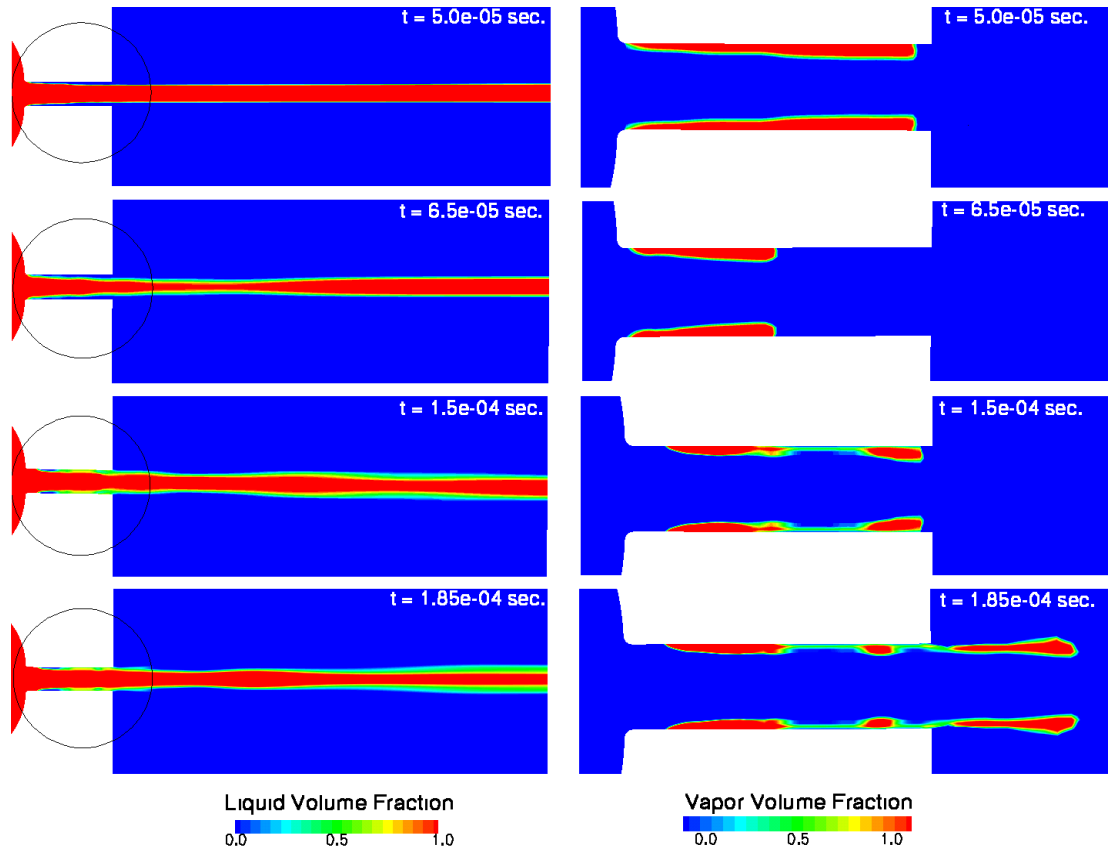


Figure 6.20: Plot of the unsteady external jet formation (left) and distribution of vapor volume fraction (right) inside and close to the exit of the nozzle injector. Periodic unsteady injection pressure, $P_{inlet} = 80 \pm 10$ bar; frequency, $f = 3.725$ mhz; exit pressure, $P_{exit} = 11$ bar.

magnitude of discharge fluctuations is related to the fluctuation of the inflow boundary condition. It should be noticed that the cavitation process for a fluctuating inflow condition intensifies the unsteadiness of the external jet formation. The instability of the jet formation and the fluctuating amount of discharge greatly affect the jet break-up and the atomization process further downstream .

Chapter 7

Multiphase and Multicomponent Turbulent Flows

This chapter extends the multiphase and multicomponent approach to turbulent flows. Multiphase and multicomponent turbulent flows are widely present in various engineering, environmental and geophysical applications. In most cases, flow configurations in these areas are very complex. Due to the complexity of the flow, modeling of turbulent flows of multiphase and multicomponent fluids is very difficult. The development of a turbulence model is the most challenging task due to a high density contrast of the fluids.

Turbulence develops whenever incipient instabilities, which are not dissipated quickly enough by the stabilizing forces acting in the fluid motion, became able to extract continuously energy from the flow [24]. Turbulence can be characterized by the Reynolds number and affected by the density variations of the fluid flow. When the density is no longer constant, new additional driving and stabilizing forces introduces new instability mechanisms. The basic mechanism from which turbulence can originate is dominated by inertia effects. At low Reynolds number, density variations influences the unsteady turbulent flow through gravity, inertia, and viscosity [24]. While, at high Reynolds number, the pressure gradient through the pressure-density coupling gains significant influence on the unsteadiness of turbulent flow. Some study of variable-density effects in low-speed regime can be found in [46, 47].

7.1 Turbulent Modeling

Current methods for modeling and simulation of turbulent flows can be grouped into three general categories: Direct Numerical Simulation (DNS), Reynolds Averaged Navier-Stokes (RANS), and Large Eddy Simulation (LES). The following briefly described the three approaches:

1. Direct Numerical Simulation (DNS) is an approach that solves the Navier-Stokes equations directly, which implies that the numerical simulation employs computational mesh capable of resolving turbulent structures all the way to Kolmogorov scale.
2. Reynolds Averaged Navier-Stokes (RANS) approach is derived by averaging Navier-Stokes equations over time, resulting either in the set of steady equations for mean quantities in the case of steady RANS or a set of evolution equations for slow varying averaged variables in the case of unsteady RANS.
3. Large Eddy Simulation (LES) is an approach, where the formal scale separation is obtained by means of a low-pass filtering operation applied to the Navier-Stokes equations. The filtered Navier-Stokes equations are closed by modeling the subgrid-scale (SGS) stresses that account for the effect of the unresolved small-scale motions [51].

The advantage of DNS approach is no modeling needed to close the governing Navier-Stokes equations, but the approach is limited to feasible small Reynolds number flows due to computational cost. On the other hand, RANS approach is computationally affordable and is widely used in many industrial engineering applications. However, there are some disadvantages of RANS approach such as modeling all the scales, obtaining only the mean flow characteristics, and unable to accurately predict spatio-temporal characteristics of turbulent flows in complex geometries and in transitional regimes.

With respect to LES, the approach is more accurate compared to RANS and able to predict spatio-temporal turbulent flow characteristics. The LES approach is physically and mathematically rigorous, and less empirical in nature. Although the LES method is still computationally intensive compared to RANS, but, with the recent breakthrough in computer technology, LES of flows of engineering interest has become computationally feasible. As a result, LES methodology is gaining momentum and is starting to be widely used in industry. The LES approach has been successfully applied to a variety of turbulent flows [19, 38, 68, 102, 113, 131, 132, 148]. On the other hand, most of the current LES implementations are limited to either single phase and single component flows [11, 18, 31, 76, 92, 107] or single phase and multicomponent flows [24, 27, 95, 110, 147]. In this thesis, the LES methodology is extended to multiphase and multicomponent flows.

7.2 Multiphase/Multicomponent Large Eddy Simulation

In LES, the large scale or the resolve scale flow field is directly calculated while the effects of small scale called subgrid scales (SGS) are modeled. The resolved variables and their governing equations are defined by explicitly applying the spatial low pass filter \mathbf{H} to each term in the governing equations. This can be done by decomposing each field quantity \mathbf{Q} in the flow domain Ω into large and small scale components,

$$\mathbf{Q} = \bar{\mathbf{Q}} + \mathbf{Q}', \quad (7.1)$$

where the filtered quantity $\bar{\mathbf{Q}}$ is defined as

$$\overline{\mathbf{Q}(\mathbf{x})} = \int_{\Omega} \mathbf{H}(\mathbf{x} - \zeta, \Delta) \mathbf{Q}(\zeta) d\zeta, \quad (7.2)$$

and \mathbf{Q}' is the SGS part that accounts for small scales not resolved by the filter width Δ . \mathbf{Q} is the vector of the conserved variables.

In compressible flows, the Favre-filtering [43, 44] is commonly used to avoid the introduction of SGS terms in the equation of mass conservation. A Favre-filtered variable

is defined as

$$\tilde{\mathbf{Q}} = \frac{\overline{\rho \mathbf{Q}}}{\bar{\rho}}. \quad (7.3)$$

In this thesis, the Favre-filtering is utilized for multiphase and multicomponent flows not only to avoid the presence of SGS terms in the continuity equation but also to account the large density fluctuation. Thus, the resolved variables (denoted by tilde) such as velocity, temperature and transport scalar fields in the mixture are written in terms of Favre-filtered quantities [130]. These are given by

$$\tilde{\mathbf{V}} = \frac{\overline{\rho \mathbf{V}}}{\bar{\rho}}, \quad (7.4)$$

$$\tilde{T} = \frac{\overline{\rho T}}{\bar{\rho}}, \quad (7.5)$$

$$\tilde{Y}_v = \frac{\overline{\rho Y_v}}{\bar{\rho}}, \quad (7.6)$$

$$\tilde{Y}_g = \frac{\overline{\rho Y_g}}{\bar{\rho}}. \quad (7.7)$$

7.2.1 Governing Equations

The governing three-dimensional time-dependent Navier-Stokes equations for the mixture given by Eq. 2.5 are extended to a full three-dimensional time-dependent LES equations. Applying the Favre-filtering operation to Navier-Stokes equations, the multiphase/multicomponent LES governing equations for the mixture are written as

$$\frac{\partial \tilde{\mathbf{Q}}}{\partial t} + \frac{\partial \tilde{\mathbf{E}}}{\partial x} + \frac{\partial \tilde{\mathbf{F}}}{\partial y} + \frac{\partial \tilde{\mathbf{G}}}{\partial z} = \frac{\partial \tilde{\mathbf{E}}_v}{\partial x} + \frac{\partial \tilde{\mathbf{F}}_v}{\partial y} + \frac{\partial \tilde{\mathbf{G}}_v}{\partial z} + \tilde{\mathbf{S}}, \quad (7.8)$$

where \mathbf{Q} is the vector of the resolved conservative variables and $\tilde{\mathbf{E}}$, $\tilde{\mathbf{F}}$ and $\tilde{\mathbf{G}}$ are the convective flux vectors given by Eq. 2.6, whose quantities are Favre-filtered. The vectors $\tilde{\mathbf{E}}_v$, $\tilde{\mathbf{F}}_v$ and $\tilde{\mathbf{G}}_v$ on the right hand side of Eq. (7.8) are the viscous flux vectors, which include the SGS terms and whose quantities are Favre-filtered. The viscous flux vectors

are written as

$$\tilde{\mathbf{E}}_v = [0, \tau_{xx}, \tau_{yx}, \tau_{zx}, \Theta_x, \Psi_{gx}, \Psi_{vx}]^T, \quad (7.9)$$

$$\tilde{\mathbf{F}}_v = [0, \tau_{xy}, \tau_{yy}, \tau_{zy}, \Theta_y, \Psi_{gy}, \Psi_{vy}]^T, \quad (7.10)$$

$$\tilde{\mathbf{G}}_v = [0, \tau_{xz}, \tau_{yz}, \tau_{zz}, \Theta_z, \Psi_{gz}, \Psi_{vz}]^T. \quad (7.11)$$

The total stress, τ_{ij} , are defined as

$$\tau_{ij} = 2\tilde{\mu}_m \tilde{S}_{ij} - \frac{2}{3}\tilde{\mu}_m \frac{\partial \tilde{v}_k}{\partial x_k} \delta_{ij} - \tau_{ij}^{SGS}, \quad (7.12)$$

where $\tilde{\mu}_m$ is the resolved viscosity of the mixture, $\tilde{S}_{ij} = \frac{1}{2}(\partial \tilde{u}_i / \partial x_j + \partial \tilde{u}_j / \partial x_i)$ is the resolved strain rate tensor, and τ_{ij}^{SGS} is the SGS stress. The work of the total stress and heat conduction in the fluid mixture are defined as

$$\Theta_x = \tilde{u}\tau_{xx} + \tilde{v}\tau_{xy} + \tilde{w}\tau_{xz} + \tilde{k}_m \frac{\partial \tilde{T}}{\partial x} - E_x^{SGS}, \quad (7.13)$$

$$\Theta_y = \tilde{u}\tau_{yx} + \tilde{v}\tau_{yy} + \tilde{w}\tau_{yz} + \tilde{k}_m \frac{\partial \tilde{T}}{\partial y} - E_y^{SGS}, \quad (7.14)$$

$$\Theta_z = \tilde{u}\tau_{zx} + \tilde{v}\tau_{zy} + \tilde{w}\tau_{zz} + \tilde{k}_m \frac{\partial \tilde{T}}{\partial z} - E_z^{SGS}, \quad (7.15)$$

where, \tilde{k}_m is the resolved thermal conductivity of the mixture and E_i^{SGS} is the SGS energy flux. Furthermore, the scalar fluxes of the gas and vapor are defined as

$$\Psi_{gi} = \tilde{\varphi} \frac{\partial \bar{\rho}_m Y_g}{\partial x_i} - \Psi_{gi}^{SGS}, \quad (7.16)$$

$$\Psi_{vi} = \tilde{\varphi} \frac{\partial \bar{\rho}_m Y_v}{\partial x_i} - \Psi_{vi}^{SGS}, \quad (7.17)$$

where $\tilde{\varphi}$ is the resolved diffusion coefficient, which is considered to be zero, unless otherwise specified. Ψ_{gi}^{SGS} and Ψ_{vi}^{SGS} are the SGS scalar flux of the gas and vapor, respectively. In addition, the vector $\tilde{\mathbf{S}}$ on the right hand side of Eq. (7.8) represents the filtered source terms written as

$$\tilde{\mathbf{S}} = [0, 0, 0, 0, 0, 0, \tilde{S}_v]^T, \quad (7.18)$$

where \tilde{S}_v is the filtered cavitation source term.

7.2.2 Subgrid Scale (SGS) Model

The SGS terms that appears in the momentum, energy and scalar equation due to the low-pass filtering of the governing equations are not known and must be modeled. The most commonly used subgrid scale model in LES is the Smagorinsky eddy-viscosity model [127], which has been widely used for incompressible flows. Piomelli *et al.* [102] have extended the model by using a scale function to avoid the model's excessive damping of SGS instabilities. An extension of the model to compressible isotropic turbulence flow was developed by Speziale *et al.* [130] and Erlebacher *et al.* [40]. To avoid the ad hoc treatment of the model constants, a dynamic subgrid-scale eddy viscosity model for incompressible flows was introduced by Germano *et al.* [49]. Furthermore, Moin *et al.* [95] have extended the dynamic model for compressible flows and scalar transport. So far, most of the subgrid scale models are limited to either incompressible or compressible turbulent flows. In this thesis, the extension of the LES to multiphase/multicomponent flows is proposed. In the following, the SGS model for momentum, energy and scalar flux for the mixture are outlined.

7.2.2.1 SGS Model for the Momentum Equation

The subgrid momentum flux, τ_{ij}^{SGS} , represents the effect of the unresolved subgrid-scales in the momentum equation. This is defined as

$$\tau_{ij}^{SGS} = \bar{\rho}_m (\widetilde{u_i u_j} - \tilde{u}_i \tilde{u}_j). \quad (7.19)$$

The term $\widetilde{u_i u_j}$ on the right hand side of Eq. 7.19 is not available, hence Eq. 7.19 cannot be solved. However, instead of solving the right hand side of Eq. 7.19, it is modeled using the eddy-viscosity model. Here, the proposed subgrid-scale eddy viscosity model of Yoshizawa [153] and Moin *et al.* [95] is utilized for modeling the SGS momentum flux of the mixture. The SGS model for the momentum flux is defined as

$$\tau_{ij}^{SGS} = -\bar{\rho}_m C_S \Delta^2 |\tilde{S}| \tilde{S}_{ij} + \frac{2}{3} \bar{\rho}_m C_I \Delta^2 |\tilde{S}|^2 \delta_{ij} \quad (7.20)$$

where static coefficients $C_S = 0.0512$, $C_I = 0.09$ were used and $|\tilde{S}| = (2\tilde{S}_{ij}\tilde{S}_{ij})^{1/2}$ and $|\tilde{S}|^2 = \tilde{S}_{ij}^2/2$. Note that the two model coefficients can be determined dynamically rather than input a priori [49, 92, 95].

7.2.2.2 SGS Model for the Energy Equation

The subgrid energy flux, E_i^{SGS} , represents the effect of the unresolved subgrid-scales in the energy equation. This comprised the SGS heat flux, E_i^{SGSHF} ; SGS turbulent dissipation, E_i^{SGSTD} ; and SGS viscous dissipation, E_i^{SGSVD} :

$$E_i^{SGS} = E_i^{SGSHF} + E_i^{SGSTD} + E_i^{SGSVD}. \quad (7.21)$$

The SGS heat flux is defined as

$$E_i^{SGSHF} = \rho_m(\widetilde{u_i T} - \tilde{u}_i \tilde{T}), \quad (7.22)$$

and is modeled using an eddy-diffusivity model similar to Refs. [92, 95], except that it is utilized for the mixture

$$E_i^{SGSHF} = -\bar{\rho}_m \tilde{c}_{pm} \frac{\nu_T}{Pr_T} \frac{\partial \tilde{T}}{\partial x_i}. \quad (7.23)$$

The term $\nu_T = C_S \Delta^2 |\tilde{S}|$ is the turbulent eddy viscosity of Eq. 7.20. Simplifying Eq. 7.23 gives

$$E_i^{SGSHF} = -\bar{\rho}_m \tilde{c}_{pm} \frac{C_S \Delta^2 |\tilde{S}|}{Pr_T} \frac{\partial \tilde{T}}{\partial x_i}. \quad (7.24)$$

where C_S is the eddy-viscosity coefficient of Eq. 7.20 that can be either defined statically or computed dynamically [49, 92, 95]. Similarly, the turbulent Prandtl number, Pr_T can be either assigned or computed dynamically [92, 95]. For simplification, a new parameter, $C_T = C_S/Pr_T$ is introduced, which can also be either defined statically or computed dynamically [28, 38, 49, 95, 101]. Finally, the SGS model for heat flux is reduced to

$$E_i^{SGSHF} = -\bar{\rho}_m \tilde{c}_{pm} C_T \Delta^2 |\tilde{S}| \frac{\partial \tilde{T}}{\partial x_i}, \quad (7.25)$$

where $C_T = 0.03125$ is used as in the case of Moin *et al.* [95] experiment.

The SGS turbulent dissipation is defined as

$$E_i^{SGSTD} = \rho_m (\widetilde{u_i u_j u_j} - \widetilde{u_i} \widetilde{u_j} \widetilde{u_j}), \quad (7.26)$$

and is modeled based on the proposed model by Knight *et al.* [76]

$$E_i^{SGSTD} = \widetilde{u_j} \tau_{ij}^{SGS}. \quad (7.27)$$

The effect of SGS turbulent dissipation is included in Eq. 7.13. A dynamic version of the SGS turbulent dissipation has been developed by Martin *et al.* [92]. The effect of SGS viscous dissipation in the energy equation is minimal and is about 5% of the divergence of SGS heat flux [92]. Since the contribution of SGS viscous dissipation to the total energy is small, $E_i^{SGSVD} \approx 0$, the effect of this is neglected in this thesis.

7.2.2.3 SGS Model for the Scalar Equation

The subgrid scalar flux, Ψ_{gi}^{SGS} and Ψ_{vi}^{SGS} , represent the effect of the unresolved subgrid-scales in the gas and vapor species equation, respectively. These are defined as

$$\Psi_{gi}^{SGS} = \bar{\rho}_m (\widetilde{u_i Y_{gi}} - \widetilde{u_i} \widetilde{Y_{gi}}), \quad (7.28)$$

$$\Psi_{vi}^{SGS} = \bar{\rho}_m (\widetilde{u_i Y_{vi}} - \widetilde{u_i} \widetilde{Y_{vi}}). \quad (7.29)$$

These terms can be modeled either using a variety of models, e.g. [95, 101] or the dynamic structure model of Chumakov *et al.* [28]. An eddy viscosity type approach is considered in this thesis and is utilized for the SGS scalar flux of the gas and vapor species equation. The SGS scalar fluxes are modeled as

$$\Psi_{gi}^{SGS} = -\bar{\rho}_m C_{Yg} \Delta^2 |\tilde{S}| \frac{\partial \tilde{Y}_g}{\partial x_i}, \quad (7.30)$$

$$\Psi_{vi}^{SGS} = -\bar{\rho}_m C_{Yv} \Delta^2 |\tilde{S}| \frac{\partial \tilde{Y}_v}{\partial x_i}, \quad (7.31)$$

where, in general, $C_{Yg} \neq C_{Yv}$ are the eddy-viscosity coefficients, which can either be assigned statically or computed dynamically [49, 92, 95]. However, note that in order

the continuity equation for the mixture to be automatically satisfied, the eddy viscosity coefficients must be equal, $C_{Yg} = C_{Yv}$.

7.3 Large Eddy Simulation of a Plane Jet

To demonstrate the capabilities of the extended LES approach for modeling and simulation of multiphase and multicomponent turbulent flows, LES of a plane jet is performed. Numerical simulations of a plane jet are very common in single phase flow [18, 31, 66, 67, 81, 82, 86, 91, 107], but not in multiphase and multicomponent flows. In this section, numerical simulations of multiphase and multicomponent jet flows are presented. In the simulation, the computational domain of the jet that is considered is 40 mm x 30 mm x 4 mm with the corresponding computational grid of 120 x 160 x 16. The computational mesh is shown in Figure 7.1 with a zoom view near the jet inlet shown in Figure 7.2. Note that this grid was chosen based on the information provided by [81, 86]. The center of the jet inlet, having a width $d = 1$ mm, is located at $x = 0$ mm and $y = 0$ mm. A uniform grid is used in the z direction with spacing $h_z = 0.25$. In the x direction, the grid is relatively fine between 0 mm and 2 mm with spacing $h_x = 0.1$ in order to have adequate numerical resolution of the inflow region, and then stretched. In the y direction, the grid is relatively fine in the ± 0.5 mm in order to resolve the initial shear layer and then stretched on both sides of the inlet.

The inflow boundary condition, see Figure 7.3, is adopted from [67], which is a top-hat mean velocity profile with a co-flow velocity of $U_c = 0.1U_j$, where U_j is the jet velocity. A three-dimensional disturbance is applied to the streamwise and cross-flow velocity at a single frequency and single spanwise wavenumber. For the outflow and upper and lower sidewall boundaries, a non-reflecting boundary condition is used.

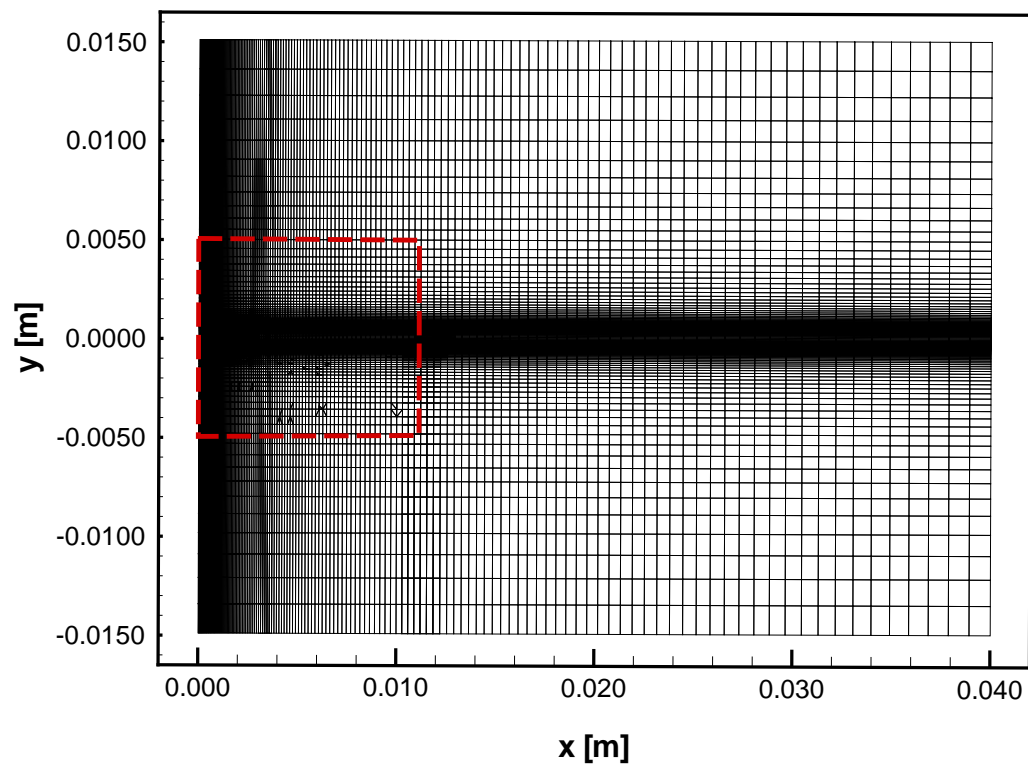


Figure 7.1: Computational grid on a x - y section.

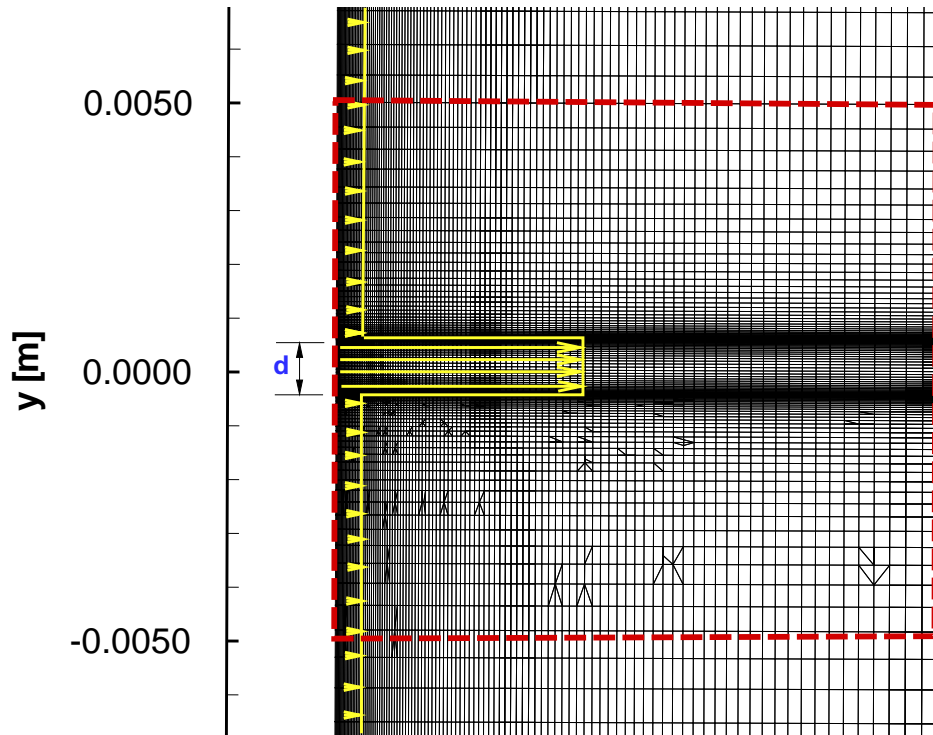


Figure 7.2: Zoom view near the inlet region.

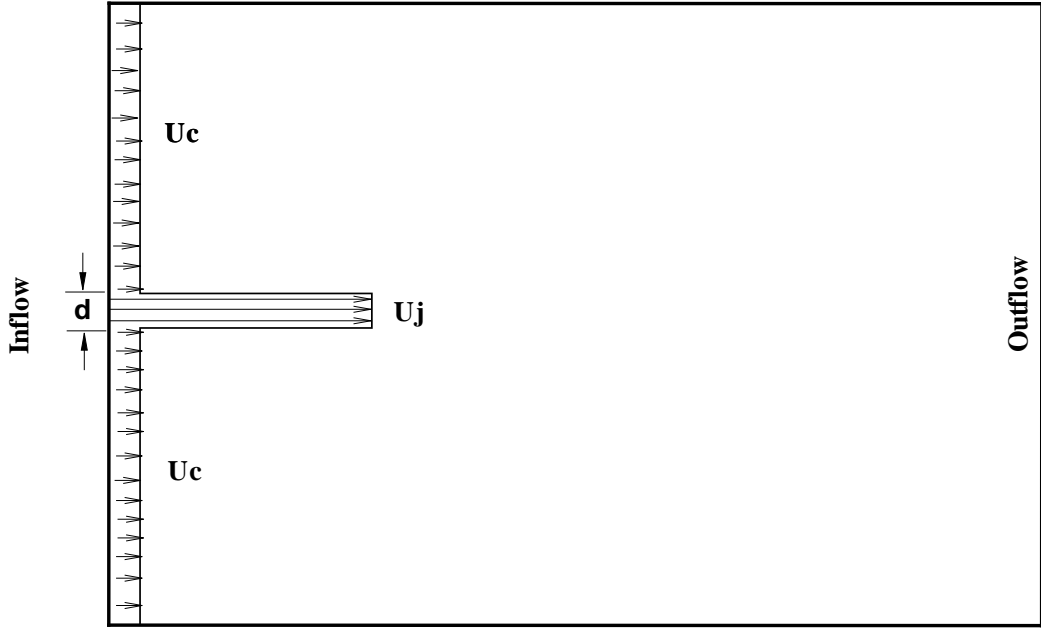


Figure 7.3: Inflow boundary condition.

7.3.1 Single Phase LES of a Plane Jet

A single phase compressible plane jet with Mach number, $M_j = 0.9$ is considered.

The jet Reynolds number is $Re_d = \rho \Delta \bar{U}_j d / \mu \approx 2000$, where $\Delta \bar{U}_j$ is the velocity difference between the two streams at the inflow, d is the slot width, and ρ and μ are the density and viscosity of the jet, respectively. The properties of the gas that are used in the simulations are $\rho = 1.18 \frac{kg}{m^3}$ and $\mu = 0.00089 \frac{N\cdot s}{m^2}$. The jet is strong since the co-flow velocity is weak compared to the jet centerline velocity, which results in a strong shear layer at the jet edges. The ratio of the jet slot width to the inflow momentum thickness is 20. Also, the velocity ratio between the low-speed and high-speed streams is 0.1.

7.3.1.1 Computational Results

The profiles of the longitudinal velocity is shown in Figure 7.4. Similarity coordinates are used with the transverse y direction normalized by the jet half-width and the jet velocity difference with respect to the small co-flow normalized by its value at the centerline. The velocity is obtained by taking the average velocity along the span-wise direction at different stream-wise location, and then computing the average velocity at different time intervals. As can be seen in Figure 7.4, the longitudinal mean velocity profile near the inflow is almost flat and then downstream, for $x > 20$, develops rapidly to self-preserving profiles. In addition, figure 7.5 shows the profiles of stream-wise fluctuation intensity at various locations. The profiles are nearly self-similar. The fluctuations observed in the figure are due to insufficient sampling sizes. The profiles of the longitudinal velocity and turbulence intensity are in good agreement although not plotted, with the experiment and simulation [81].

The early evolution of the jet, plotted with an iso-surface contour of the magnitude of vorticity, is shown in Figure 7.6. The development of the shear layer instabilities, which causes the generation of the Kelvin Helmholtz rollers is observed. The inception of flow instabilities and the amplification of fluctuating vorticity tends to further confine the vorticity. The disturbance of a vortex sheet continues to grow as the jet propagates in the stream-wise direction. The development of the jet is characterized by the dynamics of large scale vortex rings, and by strong vortex interactions that leads to a more disorganized flow regime [52]. The formation of the jet depends on the generation of vorticity near the jet exit and the jet convection and diffusion. Furthermore, the jet regime can be characterized by the Reynolds number. At moderately high Reynolds numbers, laminar jets are not stable, even in the absence of density variation and thermal effects, and rapidly develop into fully three-dimensional turbulent flows [137].

The vortex rollers continues to develop as the jet propagates downstream. The

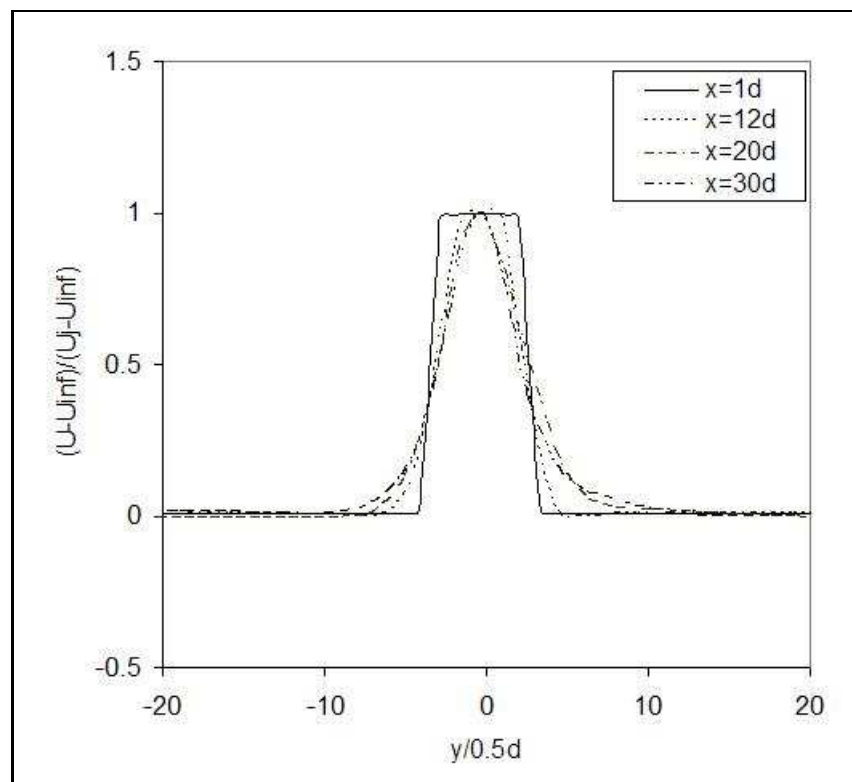


Figure 7.4: Profiles of the longitudinal velocity at different streamwise locations.

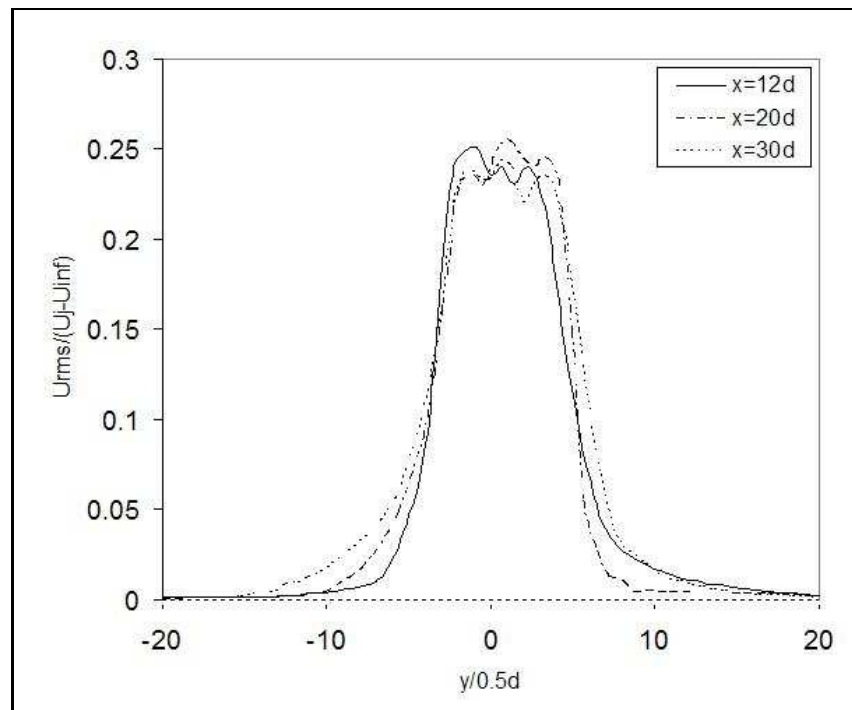


Figure 7.5: Profiles of the streamwise turbulence intensity at different locations.

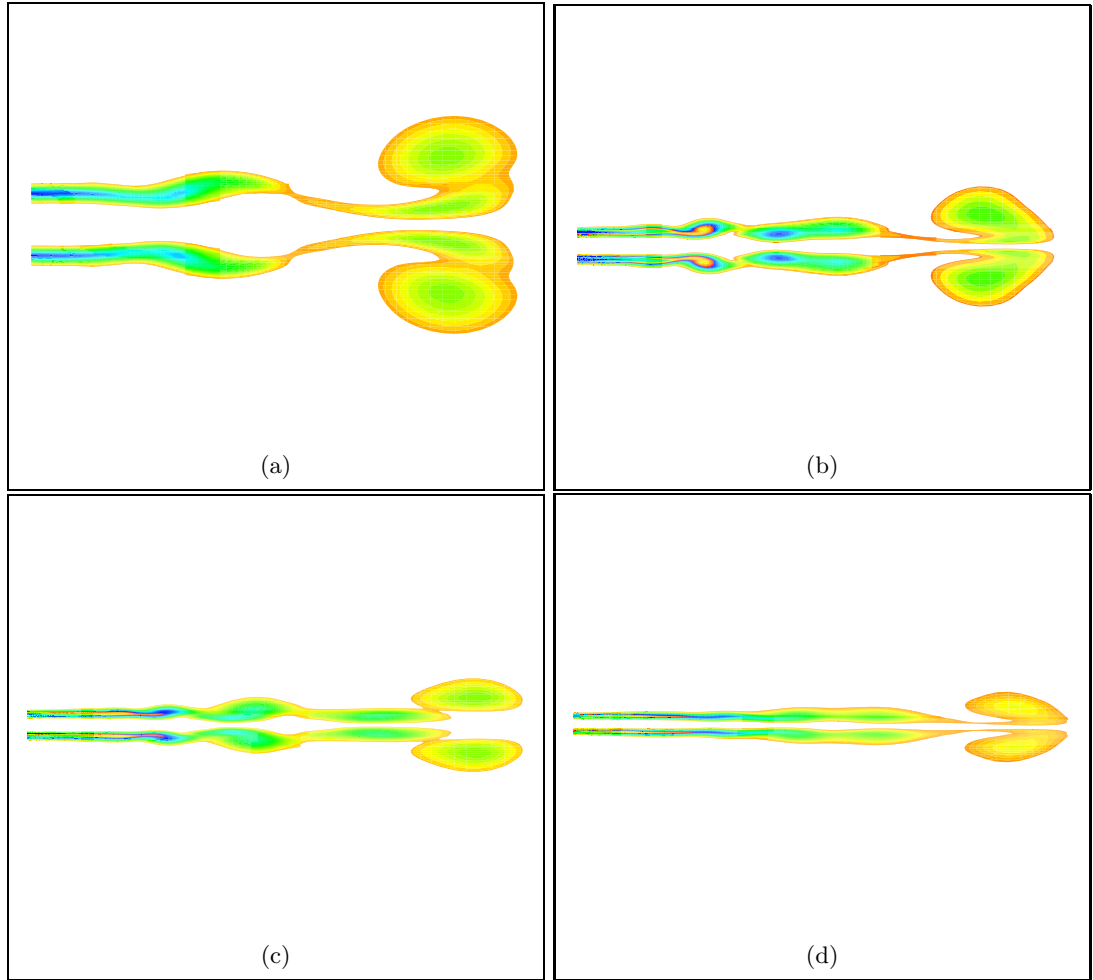


Figure 7.6: Contours of the magnitude of vorticity on an xy -plane at different time. (a) $t=5.0E-05$ sec., (b) $1.04E-04$ sec., (c) $1.4E-04$ sec., (d) $1.88E-04$ sec.

disturbance of the vortex rollers intensifies the fluctuation of the jet downstream. Figure 7.7 shows the evolution of the jet at time, $t = 2.05E - 04$ sec. The contour plot of the magnitude of vorticity as shown in Figure 7.7 (a) illustrates the development of the Kelvin-Helmholtz instability. The jet structure behaves as sinusoidal wave. This is typical behavior for small density variations, where the most dominant unstable mode is the sinusoidal mode. The velocity of the jet spreads downstream with a decreases in momentum, and at the centerline the velocity oscillates in a sinusoidal wave. The

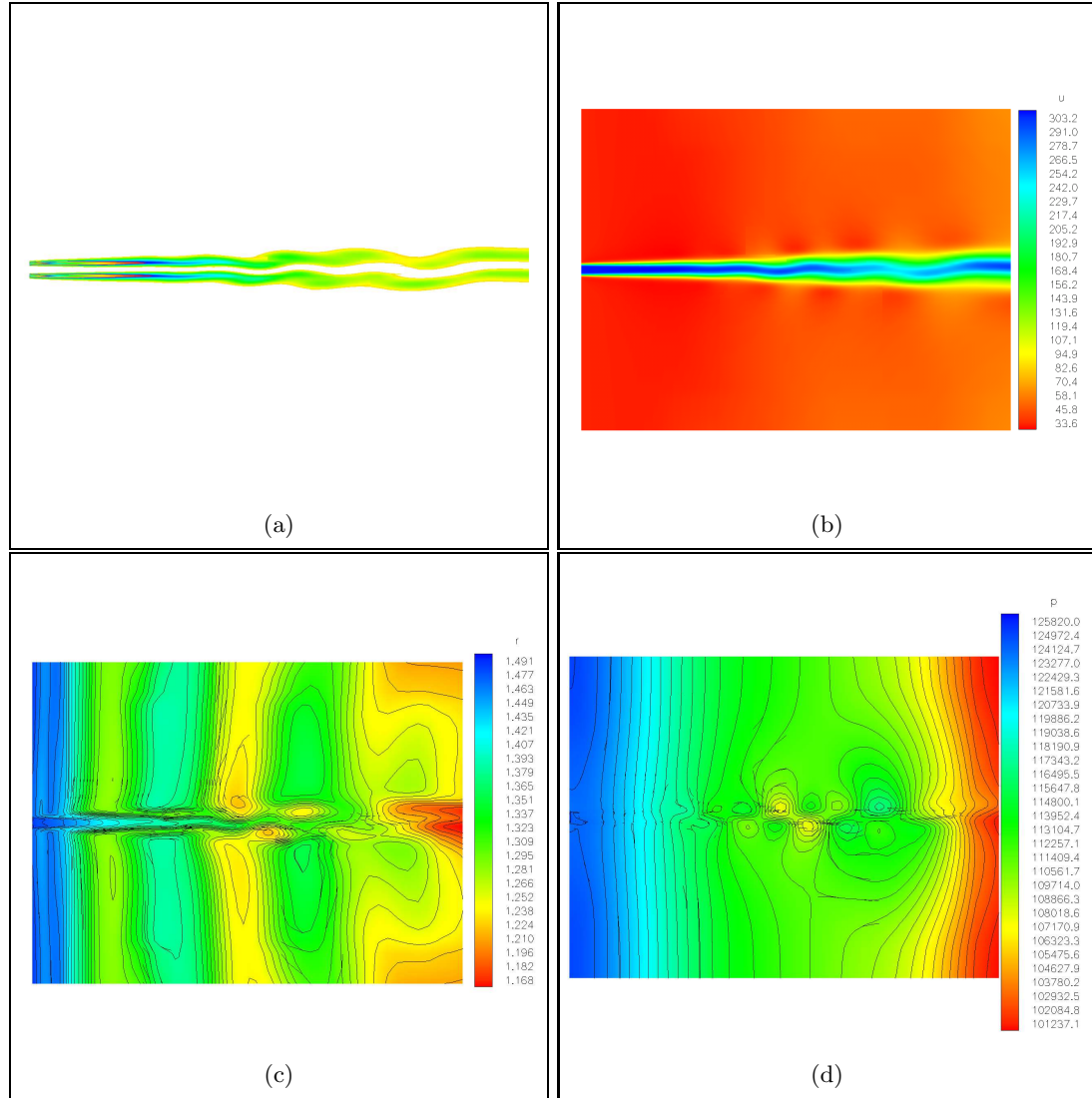


Figure 7.7: Snapshots of contours of the (a)magnitude of vorticity on an xy -plane, (b) velocity, (c) density and (d) pressure at time, $t=2.05\text{E-}04\text{sec}$.

contour plot of the magnitude of velocity is shown in Figure 7.7 (b). The jet diffuses downstream and the magnitude of density decreases as can be seen in Figure 7.7 (c). Series of recirculation zones on both sides of the jet due to the effect of vorticity and the entrainment of the surrounding medium are observed. This is visible in the contour plot of pressure field, see Figure 7.7 (d).

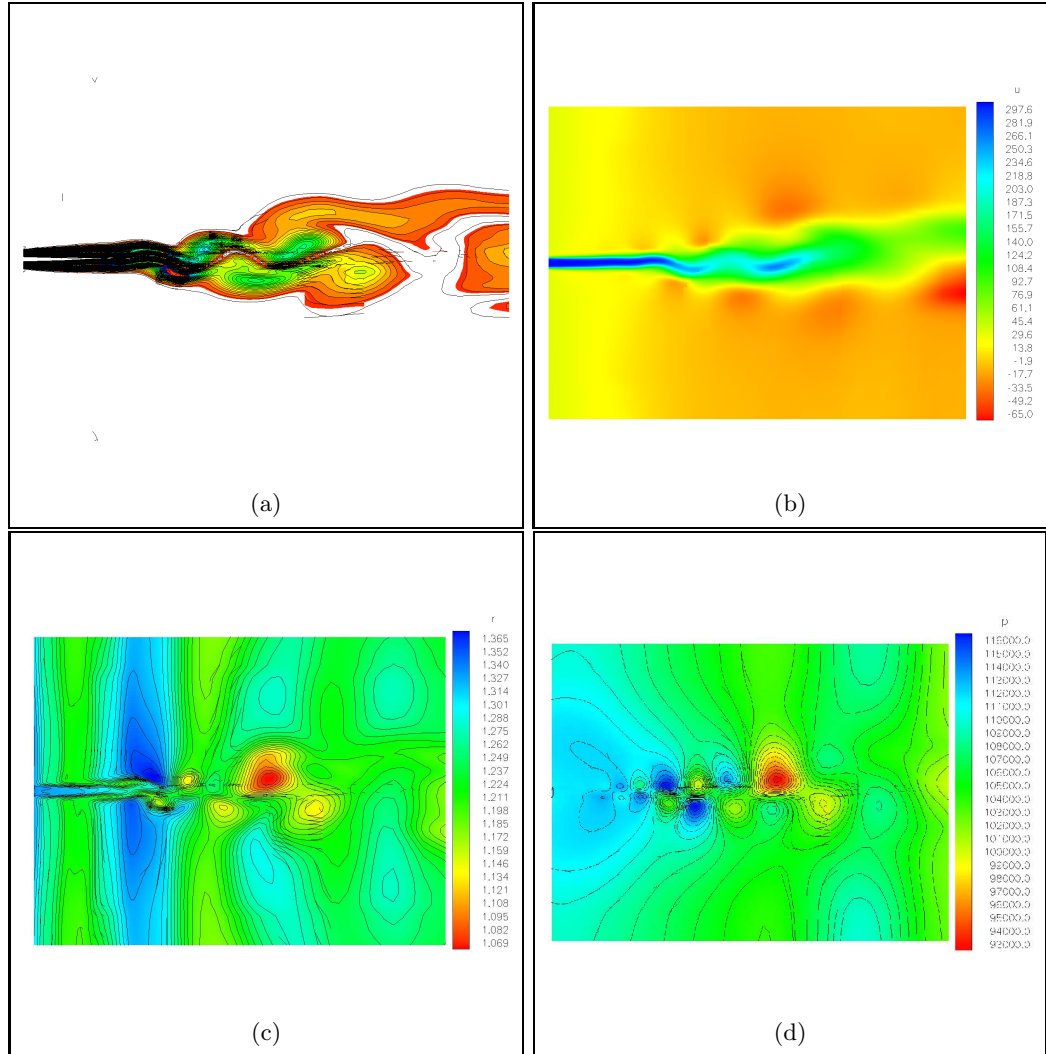


Figure 7.8: Snapshots of contours of the (a)magnitude of vorticity on an xy -plane, (b) velocity, (c) density and (d) pressure at time, $t=2.60E-04\text{sec}$.

The merging of the two unstable shear layers, which was observed in Figure 7.7 initiates the development of turbulent jet. This is illustrated in Figure 7.8. When the two unstable shear layers merge, the jet breakups and the flow separates. The contour plot of the magnitude of vorticity as shown in Figure 7.8 (a) illustrates the breakups of the jet and the separations of the flow. The momentum of the jet decreases downstream and the velocity of the jet spreads non-symmetrically. This can be observed in Figure

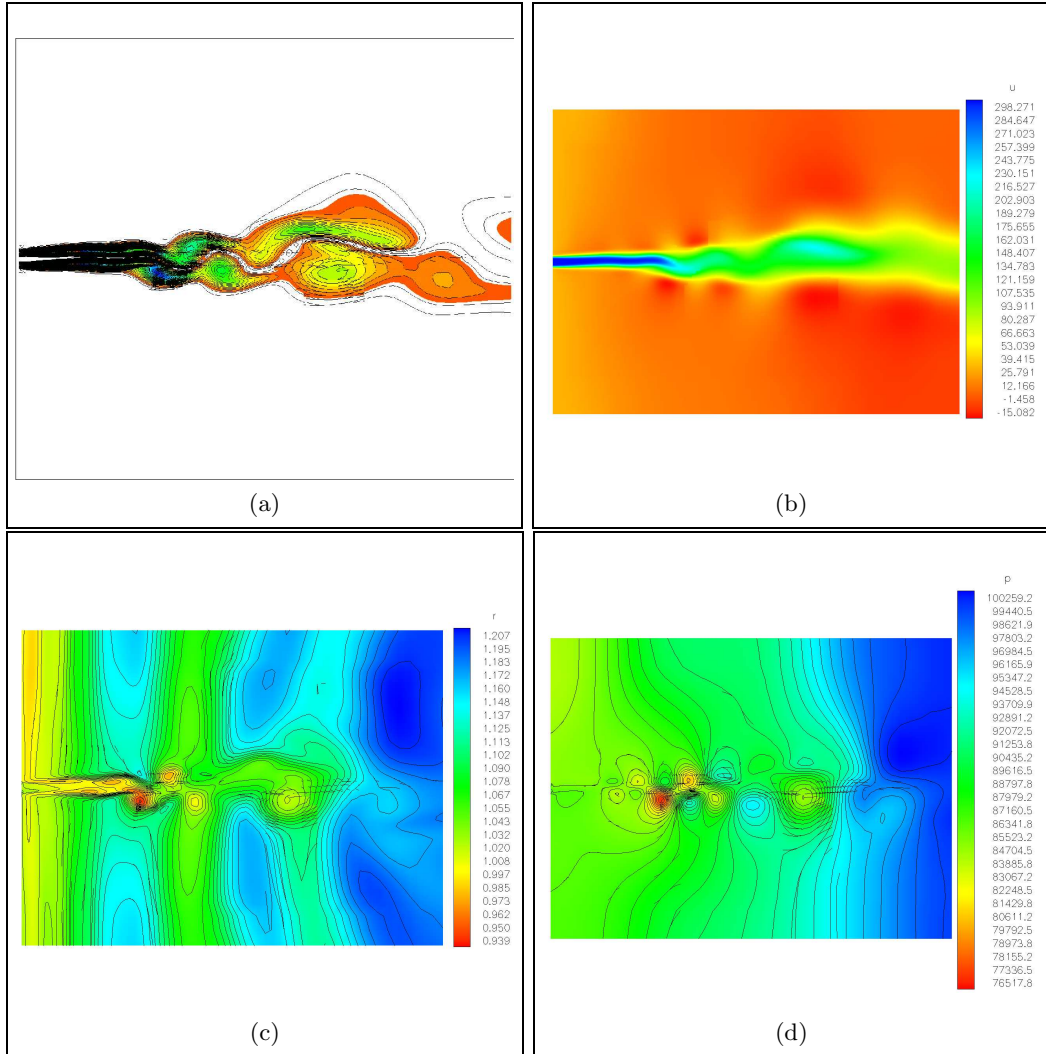


Figure 7.9: Snapshots of contours of the (a)magnitude of vorticity on an xy -plane, (b) velocity, (c) density and (d) pressure at time, $t=2.80E-04\text{sec}$.

7.8 (b), which plots the contour of the jet velocity. In addition, the jet diffuses and the magnitude of density continues to decrease due to the interaction of vortices as shown in Figure 7.8 (c). Similarly, the magnitude of pressure field decreases due to an increase of recirculations as observed in Figure 7.8 (d).

The turbulent structure of the jet including the formation of jet breakups and separation of flows varies at different time. Figure 7.9 shows the evolution of turbulent

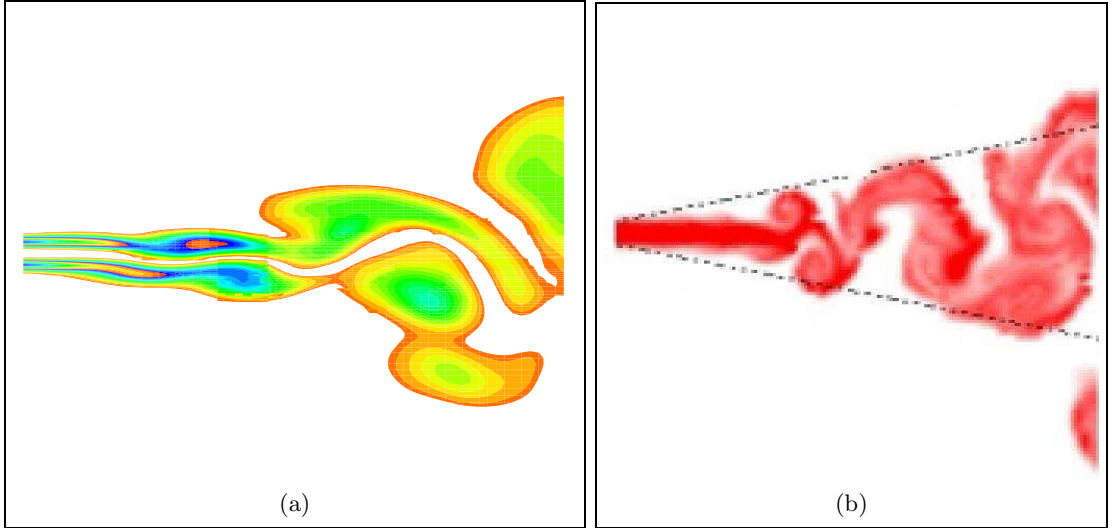


Figure 7.10: Comparison of a snapshot of turbulent jet. (a) extended LES approach for multiphase/multicomponent flows, (b) LES approach from [6].

jet at time, $t = 2.80E - 04$ sec. The formation of the jet breakups as shown in Figure 7.9 (a) differs from Figure 7.8 (a). The jet continues to loss momentum downstream as can be seen in Figure 7.8 (b). It can also be noticed in Figure 7.8 (c) the decrease of magnitude of density. Likewise, in Figure 7.8 (d), the decrease of magnitude of pressure field is observed.

A qualitative comparison of the result of numerical simulation for turbulent jet between the extended LES approach for multiphase/multicomponent flows and the LES approach from [6] is shown in Figures 7.10 (a) and (b), respectively. A good agreement of the results showing the structure of a turbulent jet is observed between the two approach.

7.3.2 Multiphase/Multicomponent LES of a Plane Jet

A multiphase/multicomponent plane jet with Mach number, $M_j = 0.9$ with respect to the gas is now considered. The jet is assumed to be a mixture of 80% liquid, 10% gas and 10% vapor by mass fraction. The jet exit through a gaseous medium. The

jet Reynolds number is $Re_d = \rho_m \Delta \bar{U}_j d / \mu_m \approx 2000$, where $\Delta \bar{U}_j$ is the velocity difference between the two streams at the inflow, d is the slot width, and ρ_m and μ_m are the mixture density and mixture viscosity of the jet, respectively. The fluid properties used in the simulations are:

1. liquid (water) with density, $\rho_l = 1000 \text{ kg/m}^3$ and viscosity, $\mu_l = 0.00089 \text{ Pa-s}$.
2. gas1 (air) with density, $\rho_g = 1.18 \text{ kg/m}^3$ and viscosity, $\mu_g = 0.0000173 \text{ Pa-s}$.
3. gas2 (vapor) with density, $\rho_v = 0.83 \text{ kg/m}^3$ and viscosity, $\mu_v = 0.000013 \text{ Pa-s}$.

The velocity ratio between the low-speed and high-speed streams at the inflow is 0.1.

The ratio of the jet slot width to the inflow momentum thickness is 20.

7.3.2.1 Computational Results

Results of numerical simulation for multiphase and multicomponent jet flows demonstrate the capabilities of the extended LES approach for multiphase and multicomponent flows. The computational results confirm physically observed phenomena, which shows that the extended LES approach works, at least qualitatively. Further test will need to be done to confirm the model behavior quantitatively. In addition, the fully dynamic models will need to be used.

Figure 7.11 shows the snapshots of the mass fraction of (a) liquid, (b) gas and (c) vapor, at time $t = 5.0E - 04 \text{ sec}$. The formation of the jet and the value of the mass fraction are consistent for each phase/component. A mushroom-shape structure is observed at the leading part of the jet. The jet spreads radially entraining the surrounding gas. The entrainment of the surrounding gas is controlled by the speed of the jet. The entrainment rate of the jet defines the rate of propagation of the interface between rotational and irrotational fluid [137]. The corresponding contour plot of the magnitude of vorticity, density, energy, pressure and velocity with vectors are shown in Figures 7.11 (b-f), respectively. The body of the jet at the leading part becomes thin

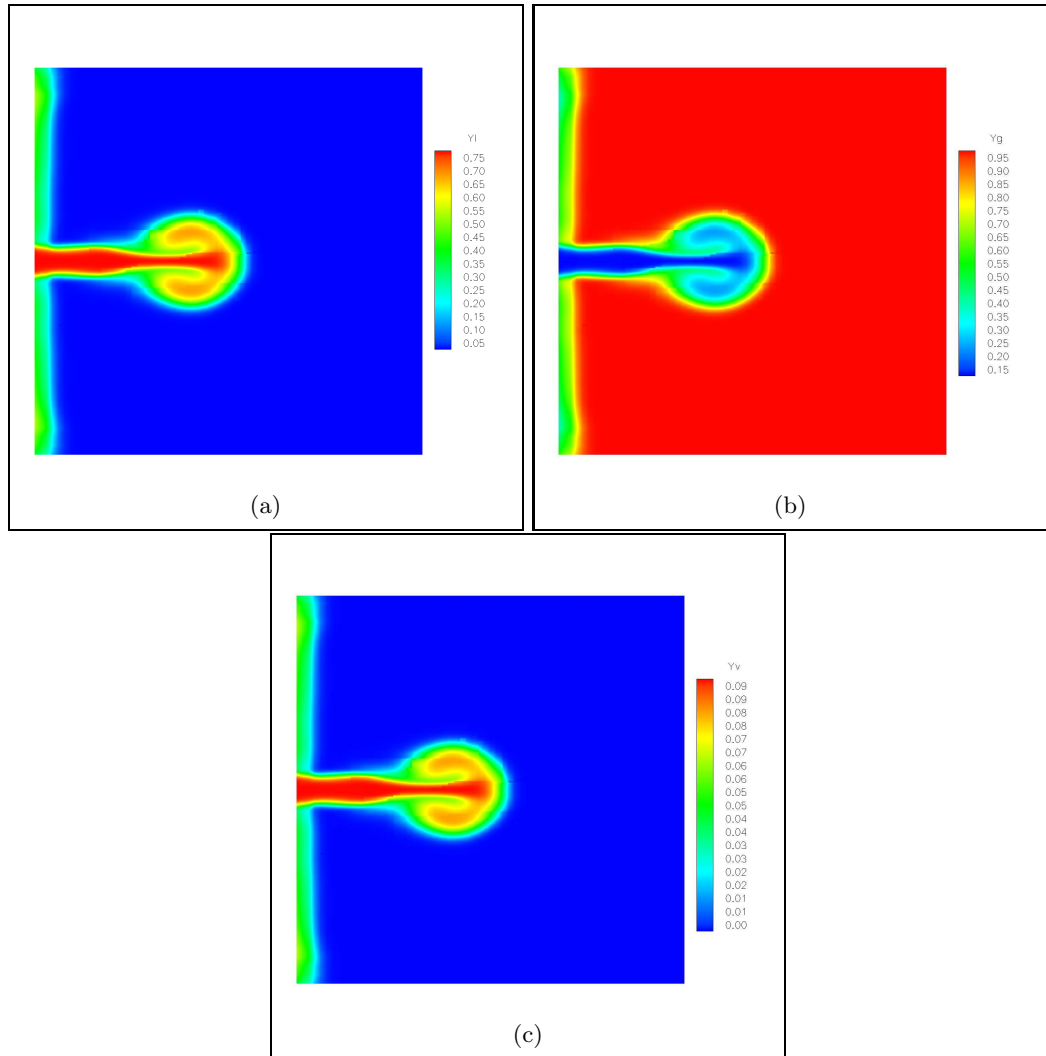


Figure 7.11: Snapshots of multiphase jet at time, $t=5.0\text{E-}04$ sec.(a) mass fraction of liquid, (b) mass fraction of gas, (c) mass fraction of vapor.

as can be observed in Figures 7.11 (c) and (d). The thinning maybe be caused by the kinematic requirements, or viscous extrusion [85]. The vorticity, see Figure 7.11 (b), at the leading part of the jet develops recirculation of flows on both sides of the leading part of the jet as can be seen in Figures 7.11 (e) and (f). In addition, the magnitude of pressure and velocity in this region decreases.

The jet expands as it continues to propagate and the structure of the mushroom-

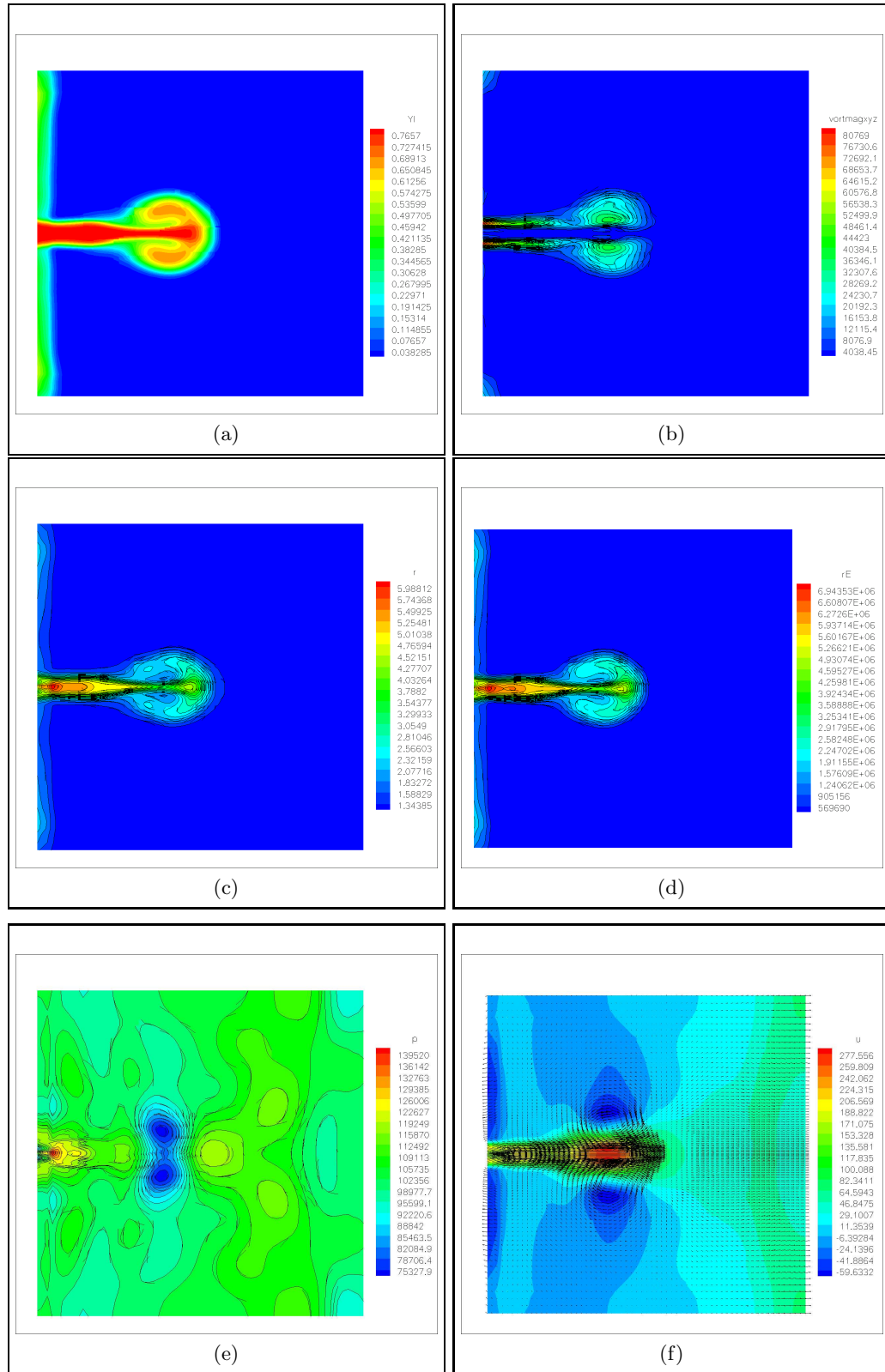


Figure 7.12: Snapshots of multiphase jet at time, $t=5.0\text{E-}04$ sec. (a) mass fraction of liquid, (b) vorticity, (c) density, (d) energy, (e), pressure and (f) velocity vectors.

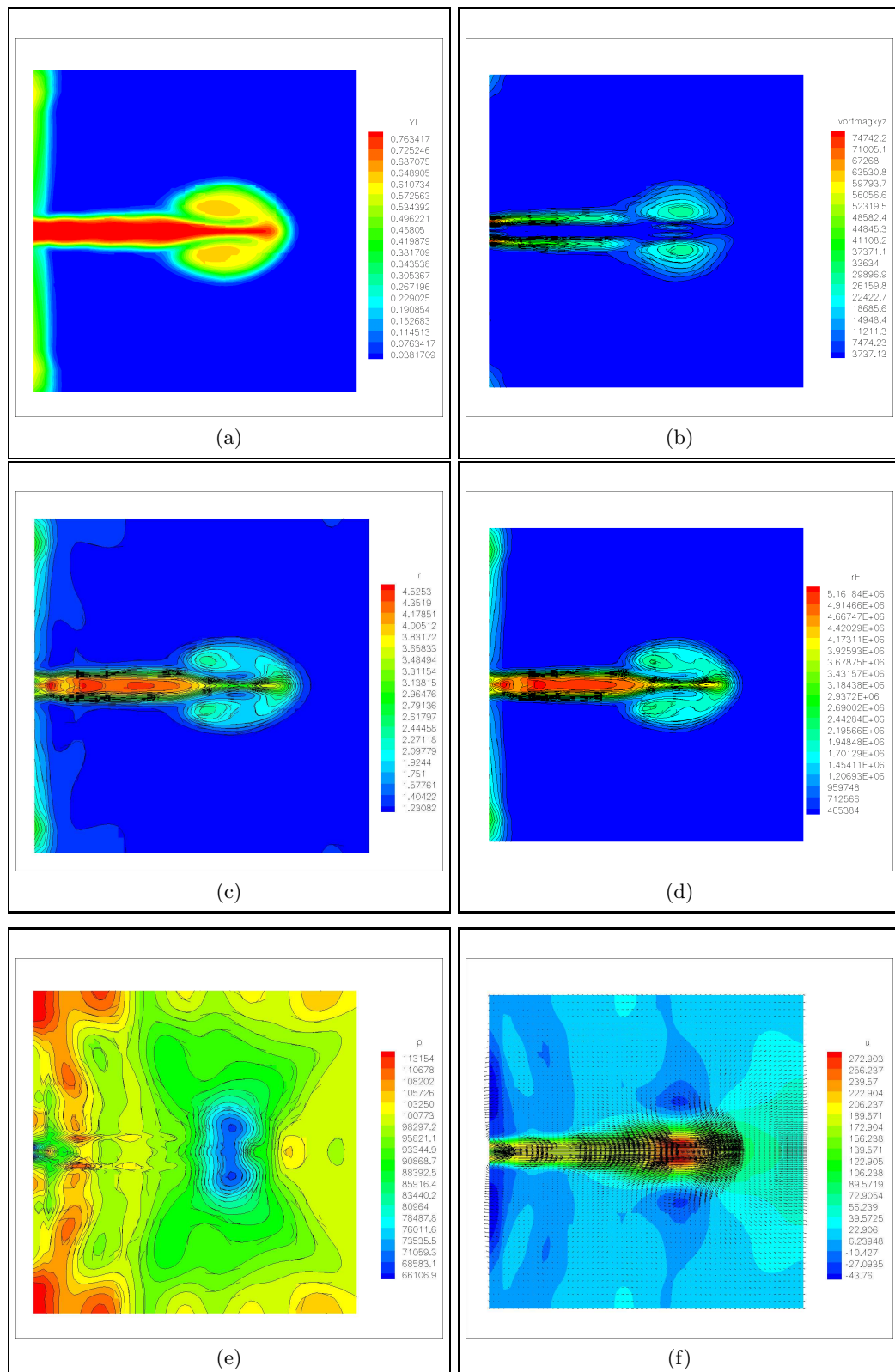


Figure 7.13: Snapshots of multiphase jet at time, $t=7.7\times 10^{-4}$ sec. (a) mass fraction of liquid, (b) vorticity, (c) density, (d) energy, (e), pressure and (f) velocity vectors.

shape at the leading part of the jet starts to deform. Figure 7.13 plots the contour of the mass fraction of liquid (a), magnitude of vorticity (b), density (c), energy (d), pressure (e) and velocity with vectors (d) at time $t = 7.7E - 04$ sec. The body of the jet at the leading part remains thin, see Figure 7.13 (a). The surface area of the jet reduces due to axisymmetric deformation. The decrease of magnitude of density and energy is observed in Figures 7.13 (c) and (d). The axial momentum of the jet decreases along the jet axis. The magnitude of pressure, see Figure 7.13 (d), at the leading part of the jet decreases also due to recirculation of flow as can be seen in Figure 7.13 (e).

In Figure 7.14, the contour of the mass fraction of liquid (a), magnitude of vorticity (b), density (c), energy (d), pressure (e) and velocity with vectors (d) at time $t = 1.0E - 03$ sec. is plotted. The leading part of the jet diffuses and expands in axial direction. The mushroom-shape at the leading part is completely deformed and disintegrated as can be observed in Figures 7.14 (a), (c) and (d). Flow recirculation on the side of the leading part of the jet is still noticeable as shown in Figure 7.14 (f), which corresponds to a decrease in pressure, see Figure 7.14 (e).

The imbalance between stabilizing and destabilizing forces in fluid motion results to the instability of the jet [24]. In constant density, homogeneous, single phase flows, such forces refers to viscous and inertial forces, when neglecting gravity and capillary effects. The instability mechanisms corresponds to the emergence of various types of vortex structures. For example, in thin shear layer flows, the basic instability processes that takes place is the so-called Kelvin-Helmholtz instability, associated with an inflexional velocity profile. On the other hand, in variable density fluid motions, the situation is different because of the new mechanisms of vorticity generation by density gradients in presence of pressure gradients.

Figures 7.15 and 7.16 show the instability of the jet at time $t = 1.2E - 03$ sec. and $t = 1.4E - 03$ sec., respectively, with the corresponding plot of (a) mass fraction of liquid, (b) magnitude of vorticity, (c) density, (d) energy, (e) pressure and

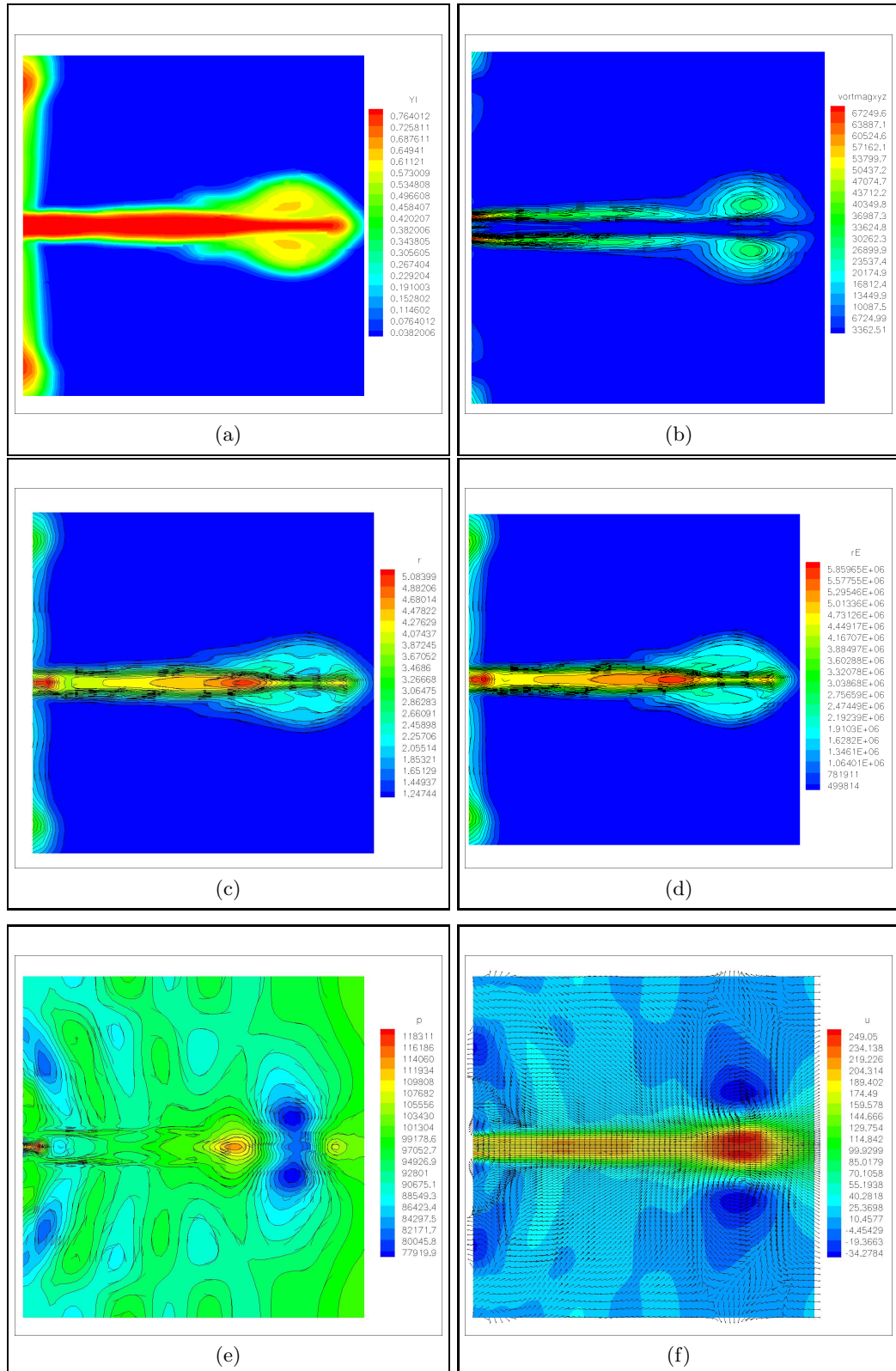


Figure 7.14: Snapshots of multiphase jet at time, $t=1.0\text{E-}03$ sec. (a) mass fraction of liquid, (b) vorticity, (c) density, (d) energy, (e), pressure and (f) velocity vectors.

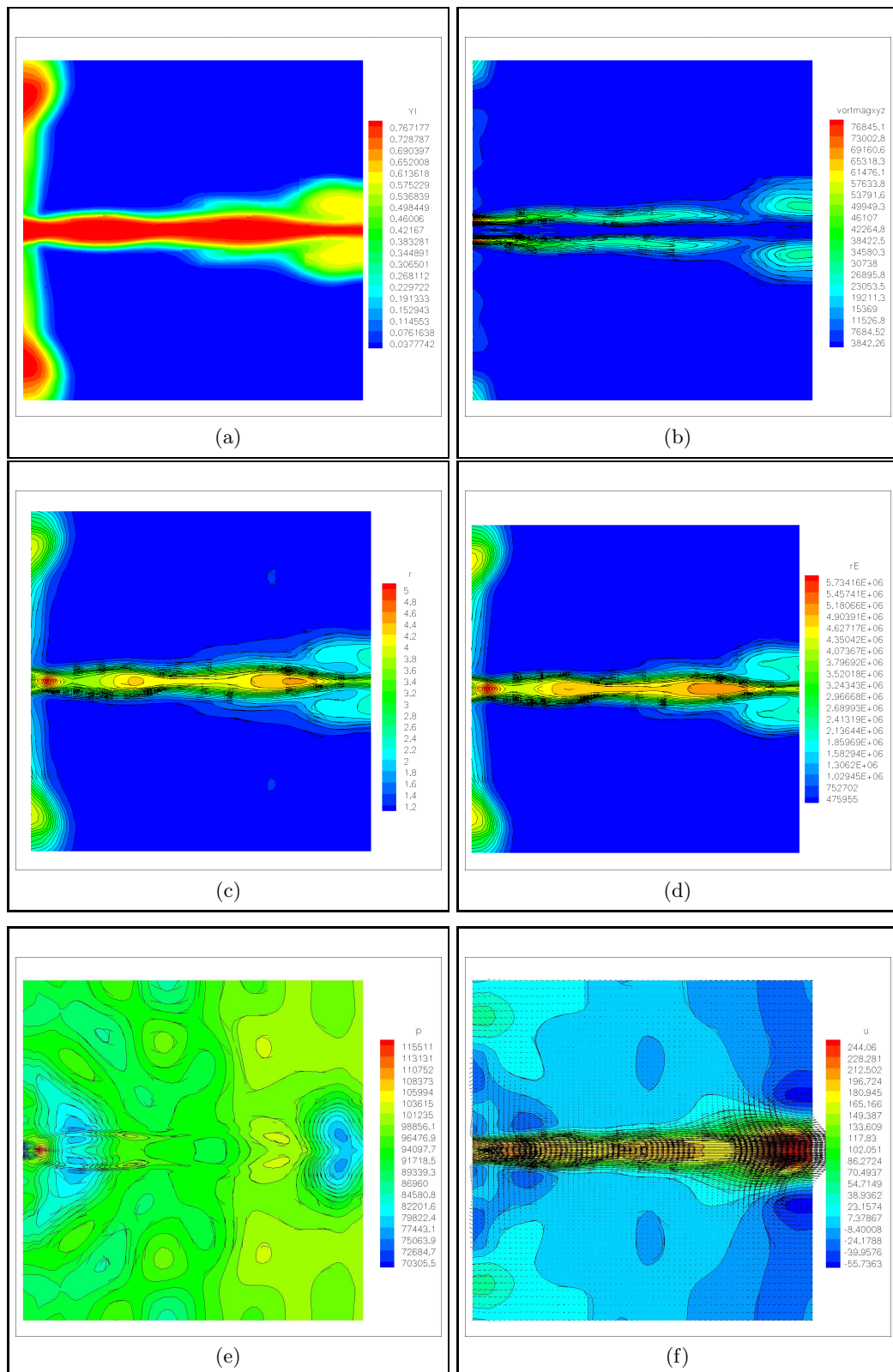


Figure 7.15: Snapshots of multiphase jet at time, $t=1.2\text{E-}03$ sec. (a) mass fraction of liquid, (b) vorticity, (c) density, (d) energy, (e), pressure and (f) velocity vectors.

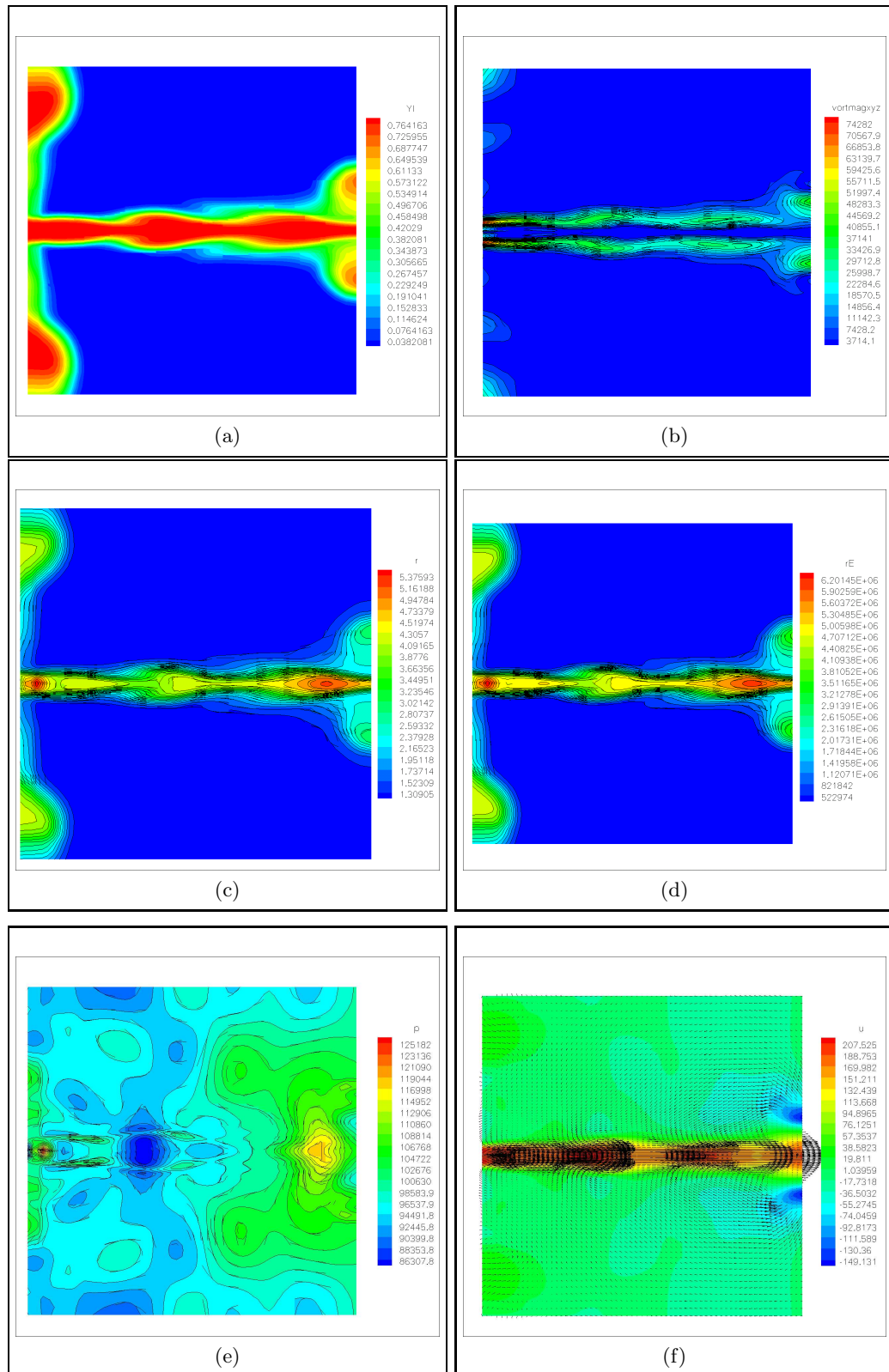


Figure 7.16: Snapshots of multiphase jet at time, $t=1.4\text{E-}03$ sec. (a) mass fraction of liquid, (b) vorticity, (c) density, (d) energy, (e), pressure and (f) velocity vectors.

(f) velocity with vectors. The instability of the jet is characterized by the unstable varicose mode [30, 34, 85] as can be seen in Figures 7.15 (a) and 7.16 (a). Rayleigh [106] have studied the hydrodynamic stability of a free liquid jet in air and have observed the symmetric instability of the jet, which he described as varicose. In addition, the pressure of the surrounding gas and the shear fluctuations provides energy to the disturbance in varicose mode instability. The unstable disturbances propagates in both the upstream and downstream direction accompanied by a pressure fluctuation. Furthermore, the deformation of the jet depends on several factors including: (1) the non-uniformity of the velocity of the jet, (2) the interaction of the jet with the surrounding gas, and (3) the viscosity of the jet. Also, turbulence controls the transfer of axial and radial momentum, which can modify the shape of the jet.

The transition from instability to turbulence depends on the boundary and initial conditions applied to the flow field. A reflection of wave from the outer boundary was observed (results not shown) after continuing the jet to propagate the outer boundary. The reflection is caused by the use of one-dimensional characteristic outflow boundary conditions, which are known to cause strong reflection waves in highly nonuniform region of the flow such as wake. Furthermore, the flow has high density variations and subsonic flow condition with very low speed of sound of the mixture. Note that the jet was a mixture of liquid, gas and vapor with a corresponding mixture speed of sound to about 25 m/s. The reflection was not experienced before in Chapter 6 because the simulations were performed at supersonic condition.

Chapter 8

Conclusions and Future Research

This chapter concludes the thesis with a summary of the computational capabilities of the new developed analytical and computational approach for modeling and numerical simulation of multiphase and multicomponent flows. Possible extensions of the work are also outlined in this chapter.

8.1 Concluding Remarks

A general approach for modeling and numerical simulation of multiphase and multicomponent, compressible and incompressible flows, which can be applied to a variety of flow configurations including shock waves, cavitation, single and multi-phase turbulent flows has been successfully developed. The approach is flexible and can have an arbitrary number of components in each phase using either Euler or Navier-Stokes formulation. The modeling and computational approach developed in this thesis is flexible enough to incorporate a variety of different cavitation and/or turbulence models. The new developed approach for multiphase and multicomponent flows does not require an *ad hoc* closure for the variation of mixture density with regards to the attendant pressure and yields a thermodynamically accurate value for the mixture speed of sound. A good agreement of the value of mixture speed of sound was observed between the derived speed of sound based on the proposed mixture model (2.50) and the experimental data of Karplus [72]. The predicted mixture speed of sound was also compared

to Refs. [3, 4, 35, 74, 143] and in good agreement. The accuracy of the value of the speed of sound of the mixture is very important in modeling and numerical simulation of multiphase and multicomponent flows.

The analytical solution of the governing equations of the mixture is very useful for validation and verification of the accuracy of the new developed approach, especially if no available experimental data. However, the governing equations of the multiphase and multicomponent mixture are not possible to solved analytically for arbitrary mixtures. The equation of state for each component must be carefully chosen, if an exact solution is to be found. To obtain an exact solution of the mixture equations, a novel “idealized” fluid mixture model was developed, which allows the derivation of an exact solution for the multiphase and multicomponent Riemann problem in one dimension. A number of existing benchmark problems for single phase and multicomponent flows become a subset of this new model.

The Roe and HLLC approximate Riemann solver, originally developed for single-phase single-component fluids, was successfully extended to multiphase and multicomponent fluids and used to capture shock waves and contact discontinuities. The accuracy of the proposed numerical method and physical model were verified and validated by solving a number of test problems. Three classical benchmark problems (single-phase two-component shock tube, shock-wave propagation in a single-phase two-component fluid, and single-phase shock-bubble interaction) and two novel benchmark problems for the idealized fluid-mixture model (two-phase shock-tube and two-phase rarefaction problems) were presented. For all problems allowing an exact solutions, good agreement between numerical and exact solutions was observed. For the case of single-phase shock-bubble interaction problem, the numerical results were compared with the experiments by [53] and the simulations by [105], and exhibited good agreement.

The new developed analytical and computational approach for modeling and simulation of multiphase and multicomponent flows was successfully applied to simulate

high pressure and supersonic multiphase and multicomponent free surface jet flows. Shock wave generation in a gaseous medium, which was observed by MacPhee *et al.* [89] using a synchrotron x-radiography and a fast x-ray detector in their experiments, was successfully captured in the simulation. The results of the simulation compliment the experiments and provide useful information for better understanding of the complex structure of the jet close to the nozzle region.

The flexibility of the new developed general approach to incorporate a variety of cavitation model was demonstrated by integrating the cavitation model proposed by Hosangadi *et al.* [64] into the general framework. The approach with the incorporated cavitation model was tested to perform simulation of multiphase and multicomponent cavitating nozzle jet flow through a gaseous medium. The results of the numerical simulation captures the cavitation process in the nozzle orifice and shows the influence of cavitation to the external jet formation. It was observed that the time scale of the internal cavitation dynamics is in the order of $10 \mu s$, which confirms the assertion of Yuan *et al.* [155]. It was found out also that the discharge of the nozzle is strongly dependent on the cavitation process and the magnitude of the bubble cavities. When the inflow condition is fluctuated, it was noticed that the cavitation separates the flow inside the nozzle injector and intensifies the unsteadiness of the external jet formation. Furthermore, It was believed that downstream the nozzle and the reattachment region, turbulence affect the breakup and coalescence of the collapsing bubble cavities.

The new developed general approach was successfully extended for modeling and numerical simulation of turbulent multiphase and multicomponent flows. The flexibility of the approach to incorporate a variety of turbulence model was demonstrated by incorporating the extended large eddy simulation (LES) methodology for multiphase and multicomponent flows into the general framework. The capability of the extended LES for multiphase and multicomponent flows was examined by conducting a numerical simulation of turbulent plane jet in both single phase and multiphase/multicomponent

flow regime. The results of the numerical simulation provide a very useful information in understanding the behavior of a turbulent plane jet. The computational results confirm physically observed phenomena including the generation of vortex rollers and development of jet instability. It was also found out that the deformation of the jet depends on several factors including: (1) the non-uniformity of the velocity of the jet, (2) the interaction of the jet with the surrounding gas, and (3) the viscosity of the jet.

Computational Capabilities

The following summarizes the capabilities of the new developed analytical and computational approach for modeling and numerical simulation of multiphase and multicomponent flows;

1. Numerical Capabilities:

- (a) Finite Volume Method,
- (b) Multiphase and Multicomponent Mixture Formulation,
- (c) Euler and Navier-Stokes Formulation,
- (d) Coupled Incompressible-Compressible Solver,
- (e) Unstructured Mesh Formulation,
- (f) Serial and Parallel Code,

2. Physical Capabilities:

- (a) Steady and Transient Flows,
- (b) Laminar and Turbulent Flows,
- (c) Steady and Unsteady Cavitation,
- (d) Shock Wave Generation,
- (e) Subsonic and Supersonic Flows,
- (f) Transport of Species (Passive and Active Scalar).

8.2 Future Research

The research presented in this thesis could be extended in three main directions: further development of numerical methodology, model improvements, and technological applications.

Algorithm development. Current explicit formulation of the method put a great constraint on time step. Implicit implementation would remove this limitation and make it more robust and computationally efficient. Another area of improvement is the use of adaptive mesh refinement strategies. This is especially important in the regions with large density contrast or contact discontinuity. Having an ability to have fine mesh along the interphase boundary will drastically decrease the error and improve the quality of the results. A good candidate for the extension of the algorithm is an adaptive wavelet collocation method [144, 145, 146]. In addition, the present one-dimensional characteristic outflow boundary conditions need to be improved by making use of non-linear multi-dimensional characteristic boundary conditions and/or applying the sponge layer technique.

Model Development. There are many types of cavitation and turbulence models available. Each model has its own strengths and weaknesses in simulation of a particular flow configuration. Thus, it could be possible to incorporate a variety of cavitation and/or turbulence model into the new developed general approach for modeling and simulation of multiphase and multicomponent flows. Consequently, perform numerical simulations of different flow configurations and conduct a qualitative and quantitative analysis for different types of cavitation and/or turbulence models. With regards to the turbulence model, the current subgrid-scale model (SGS) implemented in the LES methodology is of eddy-viscosity type. A dynamic subgrid-scale model of both eddy and non-eddy viscosity type for multiphase and multicomponent flow needs to be added in the approach in order to avoid ad hoc treatment of the model coefficients.

Applications. The approach needs to be applied to problems of engineering interest to demonstrate technological applications of the new developed analytical and computational approach for modeling and numerical simulation of multiphase and multicomponent flows. Examples of engineering applications for which the new developed general approach for numerical modeling and simulation of multiphase and multicomponent flows could be advantageously applied are in diesel and gasoline fuel injection systems, liquid jet-machining, thermal and plasma spray coating, and gas and oil transport. In addition, the approach could also be utilized for biomedical applications such as blood flow, drug/gene delivery, and shock wave lithotripsy.

Bibliography

- [1] R. Abgrall. Generalization of the Roe scheme for the computation of mixture of perfect gases. *Rech. Aerospat.*, 6:31–43, 1988.
- [2] R. Abgrall and S. Karni. Computations of compressible multifluids. *J. Comput. Phys.*, **169**:594–623, 2001.
- [3] V. Ahuja and A. Hosangadi. Unstructured simulation of multi-phase mixtures with compressibility effects. *AIAA-2001-2671*, pages 1–15, 2001.
- [4] V. Ahuja, A. Hosangadi, R. Ungewitter, and S.M. Dash. A hybrid unstructured mesh solver for multi-fluid mixtures. *AIAA-99-3330*, pages 1–9, 1999.
- [5] A. Alajbegovic, G. Meister, D. Greif, and B. Basara. Three phase cavitating flows in high pressure swirl injectors. In *Fourth International Conference on Multiphase Flow*. ICMF, 2001.
- [6] W. Altai and V.H. Chu. Les of the turbulent plane jet. *Fourteenth Engineering Mechanics Conference*, 2000.
- [7] M. Arai, M. Shimizu, and H. Hiroyasu. Breakup length and spray angle of high speed jet. *Proc. of the 3rd International Conference on Liquid Atomization and Spray Systems*, 1985.
- [8] C. Arcoumanis, M. Badami, H. Flora, and M. Gavaises. Cavitation in real size multi-hole diesel injector nozzles. *SAE Paper 2000-01-1249*, 2000.
- [9] C. Arcoumanis, H. Flora, M. Gavaises, N. Kampanis, and R. Horrocks. Investigation of cavitation in a vertical multi-hole diesel injector. *SAE Paper 1999-01-0524*, 1999.
- [10] C. Arcoumanis, J.M. Nouri, and R.J. Andrews. Application of refractive index matching to a diesel nozzle internal flow. *Proceedings of the ImechE Seminar on Diesel Fuel Injection System*, April 14-15, 1992.
- [11] Vreman B., B. Geurts, and H. Kuerten. Subgrid-modeling in les of compressible flow. *Applied Scientific Research*, 54:191–203, 1995.
- [12] C. Badock, R. Wirth, and C. Tropea. The influence of hydro-grinding on cavitation inside a diesel injection nozzle and primary break-up under unsteady pressure conditions. *Proceedings of the 15th ILASS-Europe 99*, pages 5–7, Toulouse, July 5-7, 1999.

- [13] M. Baer and J. Nunziato. A two-phase mixture theory for the deflagration to detonation transition in reactive granular materials. *Int. J. Multiphase Flow*, **12**:861–889, 1986.
- [14] F.J. Barclay, T.J. Ledwidge, and G.C. Cornfiled. Some experiments on sonic velocity in two-phase one-component mixtures and some thoughts on the nature of two-phase critical flow. *Proc. Inst. Mech. Eng.*, 184(3C):185, 1969.
- [15] P. Batten, N. Clarke, C. Lambert, and D. M. Causon. On the choice of wavespeeds for the HLLC Riemann solver. *SIAM Rev.*, **18**, 6:1553–1570, 1997.
- [16] W. Bergwerk. Flow pattern in diesel nozzle spray holes. *Proc. Inst. Mech. Eng.*, 173:655–660, 1959.
- [17] S. Biswas, A. Esmaeeli, and G. Tryggvason. Comparison of results from DNS of bubbly flows with a two-fluid model for two-dimensional laminar flows. *Int. J. Multiphase Flow*, **31**:1036–1048, 2005.
- [18] B.J. Boesrma and S.K Lele. Large eddy simulation of a mach 0.9 turbulent jet. *A99-27941*, 1999.
- [19] A.C. Buckingham. Large eddy simulation of shockwave passage through turbulence. *Engineering Applications of Large Eddy Simulations*, 162:73–80, 1993.
- [20] R.A. Bunnell and S.D. Heister. Three-dimensional unsteady simulation of cavitating flows in injector passages. *Journal of Fluids Engineering*, 122:791–797, 2000.
- [21] L.C. Burrill. Sir charles parsons and cavitation. *1950 Parsons Memorial Lecture*, 63,no.8:149–167, 1951.
- [22] C. E. Castro and E. F. Toro. A Riemann solver and upwind methods for a two-phase flow model in non-conservative form. *Int. J. Numer. Meth. Fluids*, **60**, 3:275–307, 2006.
- [23] B.W. Chandra and S.H. Collicott. Experimental investigation of cavitation frequency in a slot orifice. *ILASS-99*, pages 379–384, Indianapolis, IN, 1999.
- [24] P. Chassaing, R.A. Antonia, F. Anselmet, L. Joly, and S. Sarkar. *Variable Density Fluid Turbulence*. Kluwer Academic Publisher, 2002.
- [25] H. Chavez, M. Knapp, and A. Kubitzek. Experimental study of cavitation in the nozzle hole of diesel injectors using transparent nozzles. *SAE Paper No. 950290*, 1995.
- [26] N. Chihier. *Prog. Energy Combust. Sci*, 17:211, 1991.
- [27] S. Chumakov and C.J. Rutland. Dynamic structure models for scalar flux and dissipation in large eddy simulation. *AIAA Journal*, 42,6:1132–1139, 2004.
- [28] S.G. Chumakov and C.J. Rutland. Dynamic structure subgrid-scale model for large eddy simulation. *Int. J. Numer. Meth. Fluids*, 47:911–923, 2005.

- [29] R. Courant and K. O. Friedrichs. Supersonic flow and shock waves. *Interscience, New York*, 1948.
- [30] W.O. Crimale, T.L. Jackson, and R.D. Joslin. Theory and Computation in Hydrodynamic Stability. Cambridge University Press, 2003.
- [31] J.R. Debonis. A large-eddy simulation of a high reynolds number mach 0.9 jet. AIAA 2004-3025, 2004.
- [32] C.F. Delale, K. Okita, and Y. Matsumoto. Steady-state cavitating nozzle flows with nucleation. Fifth International Symposium on Cavitation, November 1-4, Osaka, Japan, 2003.
- [33] von M. Dirke, A. Krautter, J. Ostertag, M. Mennicken, and C. Badock. Simulation of cavitating flows in diesel injectors. Oil and Gas Science and Technology, Vol. 54, No. 2:223–226, 1999.
- [34] P.G. Drazin and W.H Reid. Hydrodynamic Stability. Cambridge University Press, 1981.
- [35] D.A. Drew and S.L. Passman. Theory of multicomponent fluids. 1998.
- [36] J. Du, B. Fix, J. Glimm, X. Jia, X. Li, Y. Li, and L. Wu. A simple package for front tracking. J. Comput. Phys., **213**:613–628, 2006.
- [37] N. Dumont, O. Simonin, and C. Habchi. Numerical simulation of cavitating flows in diesel injectors by a homogeneous equilibrium modeling approach. CAV2001:sessionB6.005, 2001.
- [38] N.M. El-Hady, T.A. Zang, and U. Piomelli. Dynamic subgrid-scale modeling for high-speed transitional boundary layers. Engineering Applications of Large Eddy Simulations, 162:103–111, 1993.
- [39] A.T. Ellis. Some effects on macromolecules on cavitation inception and noise. Calif. Inst. of Tech. Div. of Engrg. and Appl. Sci. Rep., June, 1967.
- [40] G. Erlebacher, M.Y. Hussaini, C.G. Speziale, and T.A. Zang. Toward the large-eddy simulation of compressible turbulent flows. J. Fluid. Mech., **238**:155–185, 1992.
- [41] X. Escaler, E. Egusquiza, M. Farhat, Avellan F., and M. Coussirat. Detection of cavitation in hydraulic turbines. Mechanical Systems and Signal Processing, 2004.
- [42] A. Esmaeeli and G. Tryggvason. A front tracking method for computations of boiling in complex geometries. Int. J. Multiphase Flow, **30**:1037–1050, 2004.
- [43] A. Favre. Equations des gaz turbulents compressible. i. formes generales. J. Mec., 4:361–390, 1965.
- [44] A. Favre. Equations des gaz turbulents compressible. ii. methode des vitesses moyennes; methode des vitesses macroscopiques ponderees par la masse volumique. J. Mec., 4:391–421, 1965.

- [45] L. Fraccarollo and E. F. Toro. Experimental and numerical assessment of the shallow water model for two dimensional dam-break type problems. *Journal of Hydraulic Research*, 33, 1995.
- [46] L. Fulachier, R. Borghi, F. Anselmet, and P. Parenthoen. Influence of density variations on the structure of low-speed turbulent flows: A report on euromech. *J. Fluid Mech.*, 237, 577–593, 1989.
- [47] L. Fulachier, J.L. Lumley, and F. Anselmet. Iutam symposium on variable density low-speed turbulent flows. *Number 41 in fluid mechanics and its applications*, 1997.
- [48] L.C. Ganippa, G. Bark, S. Anderson, and J. Chomiak. Comparison of cavitation phenomenon in transparent scaled-up single-hole diesel nozzles. *Proceedings of the 4th International Symposium on Cavitation*, June 20-23, 2001.
- [49] M. Germano, U. Piomelli, P. Moin, and W.H. Cabot. A dynamic subgrid-scale eddy viscosity model. *Phys. Fluid A*, 3, 7:1760–1765, 1991.
- [50] J. Glimm, M. J. Graham, J. Grove, X. L. Li, T. M. Smith, D. Tan, F. Tangerman, and Q. Zhang. Front tracking in two and three dimensions. *Comput. Math. App.*, 35:1–11, 1998.
- [51] D. E. Goldstein and Vasilyev O. V. Stochastic coherent adaptive large eddy simulation method. *Phys. Fluid*, 16, 7:2497–2513, 2004.
- [52] F.F Grinstein, M. Glauser, and W.K. George. Vorticity in jets, chapter iii of fluid vortices, ed. s. green. pages 65–94, 1995.
- [53] J. F. Haas and B. Sturtevant. Interaction of weak shock waves with cylindrical and spherical gas inhomogeneities. *J. Fluid Mech.*, 181:41–76, 1987.
- [54] T. J. Hanratty, T. Theofanous, J.-M. Delhaye, J. Eaton, J. McLaughlin, A. Prosperetti, S. Sundaresan, and G. Tryggvason. Workshop findings. *International Journal of Multiphase Flow*, 29:1047–1059, 2003.
- [55] A. Harten, P. Lax, and B. Van Leer. On upstream differencing and Godunov-type schemes for hyperbolic conservation law. *SIAM Review*, 25:35–61, 1983.
- [56] A. Harten, P.D. Lax, and B. Van Leer. On upstream differencing and godunov-type schemes for hyperbolic conservation laws. *SIAM Rev.*, 25:35–61, 1983.
- [57] A. Haselbacher. *The RocfluMP Book*. Center for Simulation of Advanced Rockets, University of Illinois at Urbana-Champaign, 2003-2006.
- [58] A. Haselbacher. A WENO reconstruction method for unstructured grids based on explicit stencil construction. *AIAA-2005-0879*, 2005.
- [59] A. Haselbacher. On constrained reconstruction operators. *AIAA-2006-1274*, 2006.
- [60] L. He and F. Ruiz. Effect of cavitation on flow and turbulence in plain orifices for high-speed atomization. *Atom Sprays*, 5:569–84, 1995.

- [61] L. F. Henderson, P. Colella, and E. G. Puckett. On the refraction of shock waves at a slow-fast gas interface. *J. Fluid Mech.*, **224**:1–27, 1991.
- [62] W. Hentschel and K.P. Schindler. *Opt. Laser Eng.*, **25**:401, 1996.
- [63] H. Hiroyasu, M. Arai, and M. Shimizu. Break-up length of a liquid spray and internal flow in a nozzle. ICLASS-91, Gaithersburg, Maryland , July, 1991.
- [64] A. Hosangadi, V. Ahuja, and S. Arunajatesan. A generalized compressible cavitation model. CAV2001:sessionB4.0043, 2001.
- [65] A. Hosangadi, N. Sinha, and S.M. Dash. A unified hyperbolic interface capturing scheme for gas-liquid flows. AIAA-97-2081, pages 1227–1237, 1997.
- [66] Z.W. Hu, C.L. Morfey, and N.D. Sandham. Sound radiation from a subsonic turbulent plane jet. AIAA 2002-2421, 2002.
- [67] Z.W. Hu, C.L. Morfey, and N.D. Sandham. Large eddy simulation of plane jet sound radiation. AIAA 2003-3166, 2003.
- [68] S.A. Jordan and S.A Ragab. On the unsteady and turbulent characteristics of the three-dimensional shear-driven cavity flow. Engineering Applications of Large Eddy Simulations, **162**:127–146, 1993.
- [69] T. Karasawa, M. Tanaka, K. Abe, and T. Kurabayashi. Effect of nozzle configuration on the atomization of a steady spray. Atom. Sprays, **2**:411–426, 1992.
- [70] S. Karni. Multicomponent flow calculations by a consistent primitive algorithm. *J. Comput. Phys.*, **112**:31–43, 1994.
- [71] S. Karni. Hybrid multifluid algorithms. *SIAM J. Sci. Comput.*, **17**, 5:1019–1039, 1996.
- [72] H. B. Karplus. The velocity of sound in a liquid containing gas bubbles. Res. Develop. Rep. C00-248, 1958.
- [73] K. Kato, Y. Matudaira, and H Obara. Flow visualization of cavitation with particle and bubble image processing. Proceedings of ASME FEDSM, July 6-10, 2003.
- [74] S. W. Kieffer. Sound speed in liquid-gas mixtures: water-air and water-steam. *J. Geophys. Research*, **82**, 20:2895–2904, 1977.
- [75] R.T. Knapp, J.W. Daily, and F.G Hammitt. Cavitation. McGraw-Hill Book Company, 1970, 1970.
- [76] D. Knight, G. Zhou, N. Okong'o, and V. Shukla. Compressible large eddy simulation using unstructured grids. AIAA Paper 98-0535, 1998.
- [77] A.L. Knox-Kelecy and P.C. Farrell. Spectral characteristics of turbulent flow in a scale model of a diesel fuel injector nozzle. SAE Paper 972942, 1997.
- [78] C.B. Laney. Computational gasdynamics. Cambridge University Press, 1998.

- [79] B. Larrouture. How to preserve the mass fraction positive when computing compressible multi-component flows. *J. Comput. Phys.*, **95**:59–84, 1991.
- [80] B. Larrouture and L. Fezoui. On the equations of multicomponent perfect or real gas inviscid flow. *Lect. Notes in Math.*, **1402**:69–97, 1989.
- [81] C. Le Ribault, S. Sarkar, and S.A. Stanley. Large eddy simulation of a plane jet. *Physics of Fluids*, **11**,10:3069–3083, 1999.
- [82] C. Le Ribault, S. Sarkar, and S.A. Stanley. Large eddy simulation of a plane jet. *AIAA Journal*, **39**,8:1509–1515, 2001.
- [83] Li, Haiyun, and S.H. Collicott. Initial images of cavitation inside high-pressure atomizers. *ILASS-99*, pages 409–413, Indianapolis, IN, 1999.
- [84] A. Lichtarowicz, R.K. Duggins, and E. Markland. Discharge coefficients for incompressible non-cavitating flow through long orifices. *J. Mech. Eng. Sci.*, Vol. 7, No. 2:210–219, 1965.
- [85] S.P. Lin. *Breakup of Liquid Sheets and Jets*. Cambridge University Press, 2003.
- [86] Y. Liu and P.G. Tucker. *Linear and nonlinear model large-eddy simulations of a plane jet*. 44th AIAA Aerospace Sciences Meeting and Exhibit, 2006.
- [87] J. Lu, S. Biswas, and G. Tryggvason. A DNS study of laminar bubbly flows in a vertical channel. *Int. J. Multiphase Flow*, **32**:643–660, 2006.
- [88] J. Lyness. Notes on the adaptive Simpson quadrature routine. *J. of the ACM*, **16**, 3:483–495, 1969.
- [89] A.G. MacPhee, M.W. Tate, C.F. Powell, Y. Yue, M.J. Renzi, A. Ercan, S. Narayanan, E. Fontes, J. Walther, J. Schaller, S.M. Gruner, and J. Wang. X-ray imaging of shock waves generated by high pressure fuel sprays. *SCIENCE*, **295**:1261–1263, 2002.
- [90] A. Mallock. The damping of sound by frothy fluids. *Proc. Roy. Soc. London Ser. A*, **84**:391, 1910.
- [91] L. di. Mare, M. Klein, W.P. Jones, and J. Janicka. Synthetic turbulence inflow conditions for large-eddy simulation. *Physics of Fluids*, **10**, 025107, 2006.
- [92] M.P. Martin, U. Piomelli, and G.V. Candler. Subgrid-scale models for compressible large-eddy simulations. *Theoretical and Computational Fluid Dynamics*, **13**:361–376, 2000.
- [93] D. McWilliam and R.K. Duggins. Speed of sound in bubbly liquids. *Proc. Inst. Mech. Eng.*, **184**(3C):102, 1969.
- [94] C.L. Merkle, J.Z. Feng, and P.E.O. Buelow. Computational modeling of the dynamics of sheet cavitation. Grenoble, 1998.

- [95] P. Moin, K. Squires, W. Cabot, and S. Lee. A dynamic subgrid-scale model for compressible turbulence and scalar transport. *Phys. Fluid A*, 3,11:2746–2757, 1991.
- [96] J. Murphy, D. Schmidt, S.P. Wang, and M.L. Corradini. Multi-dimensional modelling of multi-phase flow physics: high-speed nozzle and jet flows - a case study. *Nuclear and Engineering*, pages 177–190, 2001.
- [97] T. Nakahira, M. Komori, K. Nishida, and K. Tsujimura. *Shock Waves*, K. Takayama, Ed., 2:1271–1276, 1992.
- [98] V.E. Nakoryakov, B.G. Pokusaev, and I.R Shreiber. Wave propagation in gas liquid media. *CRC Press*, 1993.
- [99] W. H. Nurick. Orifice cavitation and its effect on spray mixing. *ASME J. Fluids Eng.*, pages 681–687, 1976.
- [100] F. Payri, R. Bermudez, R. Payri, and F.J. Salvador. The influence of cavitation on the internal flow and the spray characteristics in diesel injection nozzles. *Fuel*, 83:419–431, 2004.
- [101] C. Pierce and P. Moin. A dynamic model for subgrid-scale variance and dissipation rate of a conserved scalar. *Phys. of Fluids*, 12:3041–3044, 1998.
- [102] U. Piomelli and T.A. Zang. Large eddy simulation of transitional channel flow. *Comput. Phys. Commun.*, 65:224–230, 1991.
- [103] H. Power and C.A. Brebbia. *Computational Methods in Multiphase Flow*. WIT-PRESS Southampton, Boston, 2001.
- [104] J.R. Qin, S.T. Yu, and M.C. Lai. Direct calculations of cavitating flows by the method of space-time conservation element and solution element. *SAE 1999-01-3554*, October 25-28, Toronto, Ontario, Canada, 1999.
- [105] J. Quirk and S. Karni. On the dynamics of a shock-bubble interaction. *J. Fluid Mech.*, 318:129–163, 1996.
- [106] L. Rayleigh. On the instability of jets. *Proc. London Math. Soc.*, 10:4–13, 1879.
- [107] R.S. Reichert and S. Biringen. Numerical simulation of compressible plane jets. *AIAA*, 1997.
- [108] R.C. Reid, J.M. Prausnitz, and B.E. Poling. *The Properties of Gases and Liquids*. McGraw-Hill, Inc, New York, 1987.
- [109] R.D. Reitz. Modeling atomization processes in high-pressure vaporizing sprays. *Atomization and Spray Technology*, 3:309–337, 1987.
- [110] C.L. Ribault, S. Sarkar, and S.A. Stanley. Large eddy simulation of evolution of a passive scalar in plane jet. *AIAA Journal*, 39,8:1509–1516, 2001.
- [111] B.E. Richards, D.H. Trevena, and D.H. Edwards. Cavitation experiments using a water shock tube. *J. Phys. D: Appl. Phys.*, 13:1315–1323, 1980.

- [112] P. L. Roe. Approximate Riemann solvers, parameter vectors and difference schemes. *J. Comput. Phys.*, **43**:357–372, 1981.
- [113] R.S. Rogallo and P. Moin. Numerical simulation of turbulent flows. *Annu. Rev. Fluid Mech.*, **16**:99–137, 1984.
- [114] P. Roosen, O. Unruh, and M. Behmann. Untersuchung und modeleirung des transienten verhaltens von kavitationserscheinungen bei ein- und mehrkomponentigen kraftstoffen in schnell durchstromten dusen. *Report of the Institute for Technical Termodynamics, aachen, Germany*, 1996.
- [115] F. Ruiz and L. He. Turbulence under quasi cavitating conditions: a new species. *Atom Sprays*, **9**:419–29, 1999.
- [116] L. Sainaulieu. Finite volume approximation of two-phase fluid flows based on an approximate roe-type riemann solver. *J. Comput. Phys.*, **121**:1–28, 1995.
- [117] Sanchez and Collicott. Statistics of cavitation length in a 2-d slot orifice. *ILASS-99*, pages 403–408, Indianapolis, IN, 1999.
- [118] K. Sankaranarayanan, I. G. Kevrekidis, S. Sundaresan, J. Lu, and G. Tryggvason. A comparative study of Lattice Boltzmann and front-tracking finite-difference methods for bubble simulations. *Int. J. Multiphase Flow*, **29**:109–116, 2003.
- [119] K. Sato, S. Shimojo, and J. Watanabe. Observation of chain-reaction behavior at bubble collapse using ultra high speed video camera. *Proceedings of ASME FEDSM*, July 6-10, 2003.
- [120] R. Saurel and R. Abgrall. A multiphase Godunov method for compressible multifluid and multiphase flows. *J. Comput. Phys.*, **150**:425–467, 1999.
- [121] R. Saurel and R. Abgrall. A simple method for compressible multifluid flows. *SIAM J. Sci. Comput.*, **21**, 3:1115–1145, 1999.
- [122] D.P. Schmidt, C.J. Rutland, and M.L. Coarradini. A numerical study of cavitating flow through various nozzle shapes. *Transactions of the SAE*, **106**(3):1644–1673, 1997.
- [123] I. Senocak and W. Shyy. Computations of unsteady cavitation with a pressure-based method. *FEDSM2003-45009*, 2003.
- [124] H.H. Shi, K. Takayama, and O Onodera. *JSME Intl. J. Ser. B*, **37**:509, 1994.
- [125] B.R Shin. Numerical analysis of unsteady cavitating flow by a homogeneous equilibrium model. *Fluid Dynamics Conference*, A01-31290, 2001.
- [126] A. Singhal, M. Athavale, H. Li, and Y. Jiang. Mathematical basis and validation of the full cavitation model. *Journal of Fluids Engineering*, **124**:617–624, 2002.
- [127] Smagorinsky:1963. General circulation experiments with the primitive equations. i. the basic experiment. *Mon. Weather Rev.*, **91**:99–164, 1963.

- [128] C. Soteriou, R. Andrews, and M. Smith. Direct injection diesel sprays and the effect of cavitation and hydraulic flip on atomization. SAE Paper 950080, 1995.
- [129] C. Soteriou, M. Smith, and R. Andrews. Diesel injector laser light sheet illumination of the development of cavitation in orifices. Proc ImechE C529/018/98, 1998.
- [130] C.G. Speziale, G. Erlebacher, T.A. Zang, and M.Y. Hussaini. The subgrid-scale modeling of compressible turbulence. Phys. Fluid, 31,4:940–942, 1988.
- [131] K.D. Squires. Large eddy simulation of rotating isotropic turbulence. Engineering Applications of Large Eddy Simulations, 162:65–71, 1993.
- [132] G. D. Stefano, O. V. Vasilyev, and D. E. Goldstein. A-priori dynamic test for deterministic/stochastic modeling in large-eddy simulation of turbulent flow. Computer Physics Communications, 169:210–213, 2005.
- [133] B. H. Stewart and B. Wendroff. Two-phase flow: models and methods. J. Comput. Phys., 56:363–409, 1984.
- [134] N. Tamaki, M. Shimizu, K. Nishida, and H. Hiroyasu. Effects of cavitation and internal flow on atomization of a liquid jet. Atom. Sprays, 8:179–197, 1998.
- [135] S. Tanguy and A. Berlemont. Application of a level set method for simulation of droplet collisions. Int. J. Multiphase Flow, 31:1015–1035, 2005.
- [136] R. Tatschl, B. Wiesler, A. Alajbegovic, and C v. Knsberg Sarre. Advanced 3d fluid dynamic simulation for diesel engines. THIESEL, September 2000.
- [137] H. Tennekes and J.L. Lumley. A first course in turbulence. 1972.
- [138] V. T. Ton, A. R. Karagozian, B. E. Engquist, and S. J. Osher. Numerical simulation of inviscid detonation waves with finite rate chemistry. In Proceedings of Combustion Institue, Fall Meeting, Paper 91-101, 1991.
- [139] E. F. Toro and A. Chakraborty. Development of an approximate Riemann solver for the steady supersonic euler equations. The Aeronautical Jurnal, 98, 1994.
- [140] E.F. Toro. Riemann-problem based techniques for computing reactive two-phase flows. Proc. Third. Intern. Confer. on Numerical Combustion, No. 351 in Lecture Notes in Physics, Antibes, France:472–481, 1989.
- [141] E.F. Toro. Riemann Solvers and Numerical Methods for Fluid Dynamics. Springer-Verlag, (1999).
- [142] E.F. Toro, M. Spruce, and W. Speares. Restoration of the contact surface in the hll-riemann solver. Shock Waves, 4:25–34, 1994.
- [143] I. Toumi, A. Kumbaro, and H. Paillere. Approximate Riemann solvers and flux vector splitting schemes for two-phase flow. 30th Computational Fluid Dynamics, von Karman Institute for Fluid Dynamics, Lecture Series, 1999.

- [144] O.V. Vasilyev and Bowman. Second generation wavelet collocation method for the solution of partial differential equations. *J. Comp. Phys.*, 165:660–693, 2000.
- [145] O.V. Vasilyev and N.K.-R. Kevlahan. Hybrid wavelet collocation - brinkman penalization method for complex geometry flows. *Int. J. Numer. Meth. in Fluids*, 40:531–538, 2002.
- [146] O.V. Vasilyev and S. Paolucci. A dynamically adaptive multilevel wavelet collocation method for solving partial differential equations in a finite domain. *J. Comp. Phys.*, 125:498–512, 1996.
- [147] M.S. Vazquez, W. Vicente, A. Espinosa, and E. Barrios. Large eddy simulation of an ammonia jet. *American Journal of Applied Science*, 2,8:1270–1273, 2005.
- [148] P.R. Voke and S. Gao. Large eddy simulation of heat transfer from an impinging plane jet. *Engineering Applications of Large Eddy Simulations*, 162:29–35, 1993.
- [149] C. Vortman, G.H. Schnerr, and S. Seelecke. Thermodynamic modeling and simulation of cavitating nozzle flow. *International Journal of Heat and Fluid Flow*, 24:774–783, 2003.
- [150] S. Wang, M. Anderson, J. Oakley, M. Corradini, and R. Bonazza. A thermodynamically consistent and fully conservative treatment of contact discontinuities for compressible multicomponent flows. *J. Comput. Phys.*, 195:528–559, 2004.
- [151] F.M. White. *Fluid Mechanics*, 5th. edition. McGraw-Hill, Inc, New York, 2003.
- [152] K.J. Wu, C.C. Su, R.L. Steinberg, D.A. Santavicca, and F.V. Bracco. Measurements of the spray angle of atomizing jets. *ASME J. Fluids Eng.*, 105:406–413, 1983.
- [153] A. Yoshizawa. Statistical theory for compressible turbulent shear flows, with the application to subgrid modeling. *Phys. Fluid A*, 29:2152–2164, 1986.
- [154] W. Yuan and G. Schnerr. Cavitation in injection nozzles: effect of injection pressure fluctuations. *CAV2001:session A7.001*, 2001.
- [155] W. Yuan and G. Schnerr. Numerical simulation of two-phase flow in injection nozzles: Interaction of cavitation and external jet formation. *Journal of Fluids Engineering*, 125:963–969, 2003.
- [156] A.J. Yule and A.P. Watkins. *Atomization Sprays*, page 1441, 1991.